

EXHIBIT 4

Effect of Heated-Air Blanket on the Dispersion of Squames in an Operating Room

Said Elghobashi

Mechanical and Aerospace Engineering
The Henri Samueli School of Engineering
4220 Engineering Gateway
University of California, Irvine
Irvine, CA 92697-3975
Phone: (949) 824-6131
Email: selghoba@uci.edu

March 23, 2017

Contents

1	Introduction	2
2	Operating Room Geometry and CAD Model	7
3	Numerical Simulation	11
3.1	Large-eddy Simulation (LES): Introduction and Need	12
3.2	Governing Equations	18
3.2.1	Gas-phase equations	19
3.2.2	Equations for calculating the trajectories of individual squames	20
3.3	Computational grid	23
3.4	Boundary Conditions	28
3.4.1	Inlet boundary conditions	28
3.4.2	Hot air blower and other heat sources	31
3.5	Numerical solution method	32
3.5.1	Advancing the Lagrangian squames equations	33
3.5.2	Advancing the Eulerian fluid flow equations	34
4	Results	36
4.1	Flow characteristics	37
4.2	Dispersion of squames	42
4.2.1	Initial locations of squames	42
4.2.2	Trajectories and snapshots of squames	47
4.2.3	Number density of squames in the regions of interest	55
5	Summary and Concluding Remarks	60
	Appendices	63
	Appendix A	63
	Bibliography	65

Effect of Heated-Air Blanket on the Dispersion of Squames in an Operating Room

Abstract

A large-eddy simulation (LES) of the interaction between the ventilation air flow and forced hot air from a blower is performed to investigate the effect of hot air on dispersion of squames in a realistic operating room (OR) consisting of an operating table (OT), side tables, surgical lamps, medical staff, and a patient. Two cases with blower-off and blower-on are calculated together with Lagrangian trajectories of 3 million squames initially placed on the floor surrounding the OT. The squames particles are assumed as spheres of size 10 microns and the drag, lift and buoyancy forces are considered in calculating their instantaneous motion. It is shown that with the blower-off, squames are quickly transported by the ventilation air away from the table and towards the exit grilles. However, with the hot air blower turned on, the ventilation air flow above and below the OT is disrupted significantly. The rising thermal plumes from the hot blower air drag the squames above the OT and the side tables and then they are blown downwards toward the surgical site by the ventilation air from the ceiling. Temporal history of number of squames particles reaching four imaginary boxes surrounding the side tables, the OT, and the patient's knee shows that several particles reach these boxes with the blower turned on. The study shows that LES is necessary to accurately capture the mixing and transport in a turbulent flow and predict the dispersion of squames in an OR.

1 Introduction

Microbial skin colonizers, such as *Staphylococcus aureus*, have been known as a major cause of surgical site infections in operating rooms (Noble, 1975; Clark & de Calcina-Goff, 2009; Wood *et al.*, 2014). These bacteria typically colonize on human skin cells or squames which are routinely shed by humans, roughly about 10^7 particles per day (Noble, 1975). The squame particle size ranges over 4–20 μm of equivalent diameter (Noble *et al.*, 1963; Lees & Brighton, 1972).

Reduction of post-operative surgical site infections has been linked to two main factors: (i) ultra-clean ventilation (UCV) systems, and (ii) perioperative patient warming (Ng *et al.*, 2006; Legg *et al.*, 2012; Wood *et al.*, 2014). Ultra-clean ventilation aims to reduce the quantity of airborne bacteria in the operating room (OR) and most importantly near the surgical site. This is typically achieved by the constant delivery of highly filtered ultra-clean air with a downward uniform velocity of 0.3-0.5 m/s (McGovern *et al.*, 2011). The UCV performance depends critically on volumetric airflow, proper temperature gradients, use of uniform downward flowing ventilation air, potentially in the laminar regime (Memarzadeh & Manning, 2002; Pereira & Tribess, 2005). Surgeons and other medical equipment within the operating room (surgical lights, tables, patient, computers, etc.), motion of surgeon's arms and their bending motion (Chow & Wang, 2012) can disrupt this air flow

and create wakes, flow unsteadiness, and turbulence, thereby increasing the amount of cfu in the OR.

Perioperative patient warming is the other important clinical practice to prevent inadvertent surgical hypothermia, wherein the core temperature of the patient drops below 36°C. Preventing inadvertent perioperative hypothermia has several benefits that include reduced operative blood loss, reduced duration of surgery, improved wound healing, reduced wound infections, reduction in post-operative ulcers, reduced duration of hospital stay, and increased survival rates (Wood *et al.*, 2014; Ng *et al.*, 2006; Legg *et al.*, 2012). Monitoring and maintaining body temperature during surgery is therefore an accepted and required practice. Warttig *et al.* (2014) review different methods used to combat inadvertent perioperative hypothermia. These include use of warm cotton blankets, reflective blankets, warmed intravenous and irrigation solutions, circulating warm water mattresses, a reusable electric blanket, an electric heating pad, and forced-air warmers (Kellam *et al.*, 2013; Austin, 2015). Of these, active warming using forced air warming (FAW) devices, and passive warming based on the use of reflective blankets, are the two main techniques used to keep the patient's body warm and prevent hypothermia. Although passive heating techniques may show similar effectiveness as the FAW devices, the latter have been used for over two decades due to their efficacy in maintaining patient's core body temperature. These techniques use forced convection to increase the skin temperature and the total body heat content. These devices contain a blower (such as 3M™ Bair Hugger™) that extracts the room temperature air through an air-intake filter heats the air using a heating coil, and vents the air into the sterile field adjacent to the operative site (Albrecht *et al.*, 2011; Leaper *et al.*, 2009; Wood *et al.*, 2014). The filtered and warm air flows through a connecting hose into blankets made of plastic and exits the blankets through tiny holes over the patient's skin. However, this forced warm air has the potential to generate and mobilize airborne contamination in the operating room.

A number of studies have examined at the safety of forced-air warming, and whether FAWs can affect surgical site infections through mobilized airborne contamination. FAWs can potentially lead to surgical site contamination in two ways: (i) direct contamination of the air from the blowers that reaches the patient's body, and (ii) disruption of the ultra-clean ventilation air by the thermal plumes and turbulence. The former risk can potentially be reduced by using intake filters that are HEPA-rated and show high filtration efficiency. The latter has been studied extensively as reviewed

by Wood *et al.* (2014). It is hypothesized that the temperature gradients and resultant thermal plumes created by the FAW devices could disrupt the benefits of UCV flow, that is designed to be uniform and downwards. The interaction between the FAW and UCV flows may lead to increased surgical site infections (SSI).

McGovern *et al.* (2011); Legg *et al.* (2012) have shown that temperature gradients and excess heat created by FAW devices can transport air from the unsterilized floor level to the surgical site, thus increasing the potential risk of SSIs. Moretti *et al.* (2009) measured an increase in the bacterial load when FAWs were used. Lack of flow visualization is the main drawback of these studies as it does not provide information about whether the particles came from the floor or from the FAW blower. Legg *et al.* (2012); Sessler *et al.* (2011) used smoke particle visualization to understand the source of these particles near the surgical site comparing cases with no warming, FAW, and radiant warming. Although they found that FAW increased the particle count with blower turned on (almost 10-fold increase), they also showed that the uniform, laminar flow from the ultra-clean ventilation reduced the effect of particles by limiting their numbers near the surgical site.

It is clear from the available literature that the interaction between the UCV flow and the rising plumes from the forced-air warming devices plays a critical role in deciding whether FAWs indeed can lead to increased number of particles near the surgical site. However, there have not been detailed experimental measurements of flow patterns in the OR setting with the FAW blower turned on. Recently, McNeill *et al.* (2012, 2013) conducted particle-image velocimetry (PIV) measurements to understand the flow pattern in an OR with the ultra-clean ventilation system. This study, however, did not investigate the effect of FAW blower. McNeill *et al.* (2013) also made detailed measurements of temperature fields on surgeon's and patient's body to be used for computational modeling. Although the above PIV was able to visualize and measure the flow field, it was limited to planar data (2D PIV) and thus a full three-dimensional data are not available for the OR. Nevertheless, some useful information on the flow unsteadiness, turbulence within the room was obtained from the McNeill *et al.* (2013) study.

The only other way to characterize the flow field in an OR with and without FAW blowers, is to use computational fluid dynamics (CFD) modeling in three-dimensions. This, however, is a difficult task due to the size and complexity of the domain involving medical equipment, staff, computers, etc. There are only few CFD studies in the literature that used Reynolds-averaged Navier

Stokes (RANS) models (Memarzadeh & Manning, 2002; Memarzadeh, 2003; Chow & Wang, 2012), wherein only the time-averaged velocity field is computed. All information about the turbulence and velocity fluctuations is completely *modeled*. As is shown later (section 3), RANS approach is not predictive, since the instantaneous velocity field needed for calculating the trajectories of squames is not directly computed. Thus, RANS is incapable of accurately predicting the locations of squames at any time in the OR. Memarzadeh & Manning (2002); Memarzadeh (2003) investigated the effect of various UCV inlet flow conditions on the transport of squames particles in an OR. They considered a realistic OR with medical staff, equipment, surgical lamps, etc. and accounted for the thermal plumes created by heat radiated from various sources. However, they used a RANS model coupled with a Lagrangian particle-tracking of around 4000 representative particles. Their study did not include the FAW blower discharge. They showed that use of a uniform inlet flow with laminar conditions¹ is better for reducing the number of particles near the surgical site. In addition, they found that the thermal plume created by the hot surface of the surgical site prevented particles from reaching the site. They showed that roughly 2-5% of particles reach the surgical site, *provided they are originated very close, about 1.3cm above the site*. Particles originating from locations away from the surgery did not have a statistically significant probability of reaching the surgical site. As is discussed later in section 3, RANS model cannot compute the instantaneous velocity field needed to accurately calculate the forces on particles, and particle trajectories.

Chow & Wang (2012) investigated the ultra-clean ventilation flow and its effect on bacteria-carrying particles in an OR using a RANS model as well. They simulated the bacteria particles as a non-inertial pollutant, wherein an Eulerian transport equation for the concentration of the bacteria is calculated. In addition, they considered periodic bending movement of one of the surgeons performing the operation. They found that if the surgical staff stands upright (no bending), the UCV flow keeps the bacteria concentration very low ($< 1 \text{ cfu/m}^3$) near the surgical site. However, with the surgeon's bending motion included, they showed that this concentration increased to larger than the recommended value (10 cfu/m^3).

All of the above computational studies are based on RANS modeling and did not include the

¹It should be noted that the literature uses the terminology 'laminar flow' for the ultra-clean ventilation flow. Based on the standard values of air changes per hour (ACH) for an OR (25 per hour), the inlet grille sizes, and properties of air, the flow Reynolds numbers are much larger than 2000, a critical value beyond which turbulence occurs in a duct. The inlet grille flow, thus is not typically laminar. Although the level of turbulence in the inlet flow is not large ($< 10\%$), the flow contains velocity fluctuations and is unsteady.

FAW blower system together with a blanket cover above the patient. In order to assess the interaction between UCV and FAW blower, a systematic, predictive simulation is needed. Large-eddy simulation (LES) is a numerical technique that involves computing the properties of the large, energy-containing eddies of turbulence accurately, without any user adjustable tuning parameters, and models only the more homogeneous, small scales of turbulence (Pope, 2000; Piomelli, 2014). This technique provides the instantaneous three-dimensional velocity, temperature, and pressure fields and has been shown to be far more accurate than the RANS model. Section 3 outlines the differences between LES and RANS in detail. In addition, since the time dependent, three-dimensional velocity field is available in LES, then the forces on particles and their trajectories can be calculated accurately (Apte *et al.*, 2003b; Ham *et al.*, 2003; Apte *et al.*, 2009; Moin & Apte, 2006; Mahesh *et al.*, 2006). The only challenge with this technique is that it is computationally intensive and requires fine grid resolutions and small time-steps to capture the large-scales of turbulence. Recent advances made in algorithmic developments for LES on arbitrary shaped, unstructured grids (Mahesh *et al.*, 2004; Ham *et al.*, 2003; Moin & Apte, 2006; Mahesh *et al.*, 2006; Ham & Iaccarino, 2004) have facilitated application of LES to more realistic problems involving complex geometries and flow conditions. These advances have been successfully applied to turbulent, reacting flows in a gas-turbine combustion chamber and has led the gas-turbine industry to switch from RANS to the predictive LES technique in their design cycle (Moin & Apte, 2006; Mahesh *et al.*, 2006; Apte *et al.*, 2009).

LES applied to operating rooms with medical staff and other instruments is still challenging, owing to the size of the room and the complexity of the geometries involved. At the time of writing this report, only one LES study has been performed for an operating room by Saarinen *et al.* (2015). They studied the escape of air into an isolation room during opening and closing of a door and passage of a human figure. They used passive smoke visualizations to compute the volume flux of air when a door is opened. Although this study had some complex geometry (a human figure), it did not have the intricacies of the OR table, surgeons, patient and other medical equipment, nor it computer the dispersion of squames in the OR. Nevertheless, it showed that LES can accurately predict such flows through validation with experimental observations.

The main goal of the work reported here is to use large-eddy simulation to compute the interaction of the OR ultra-clean ventilation air flow and the flow created by forced air warming

system (such as 3MTM Bair HuggerTM) and investigate their impact on the dispersion of squames. Specifically, computations are conducted for the cases with blower-off and blower-on, including the Lagrangian tracking of inertial squame particles, starting from the operating room floor, to prove whether the FAW system and the resultant thermal plumes play a role in transporting squame particles to the surgical site.

The rest of the report is arranged as follows. In section 2, details of the operating room geometry and CAD model are described. This includes the OR dimensions, the surgical lamps, four medical staff, an operating room table, two side tables, the blower, and the patient undergoing knee surgery. The numerical approach is described in section 3. This includes a detailed discussion of LES and RANS, the governing equations used for LES, the computational grid, and the boundary conditions. The numerical algorithm used is briefly summarized in section 3.5. This is followed by detailed description of the results in section 4 on flow field, particle trajectories and particle counts that reach the surgical site and other key regions of interest. Finally, the findings are summarized in section 5.

2 Operating Room Geometry and CAD Model

The operating room CAD (computer aided design) model was created using Ansys[®] SpaceClaim Direct ModelerTM (ANSYS, Inc., Canonsburg, PA, USA). The CAD model replicated a realistic operating room (OR) depicting a knee surgery being performed on a patient. An original baseline CAD model was obtained from M/E Engineering P.C. (Straub, 2016) and was further modified to incorporate the measured dimensions of the inlet air grilles and the surgical drape as shown below. Figure 1a shows the OR dimensions used to create the CAD model. The length, width and height of the room are 7.32m, 7.01m and 3.18m, respectively. These dimensions are from 3M video at: <https://www.youtube.com/watch?v=QhzeInWIJ54>. Figure 1b shows a close-up view of the surgeon's hands extended over the patient's knee mimicking a real world operating procedure.

The CAD model also includes several objects that are usually present in a real OR. Typically, there can be several combinations of such objects, but for this study the following objects were included in the model. These are shown in a top view in figure 2 and include: (i) OR Table; (ii) OR drape; (iii) patient's body under the drape with knee exposed; (iv) four surgeons (two of the surgeons have extended hands and two have hands down), (v) two side tables, (vi) two surgical lamps, (vi)

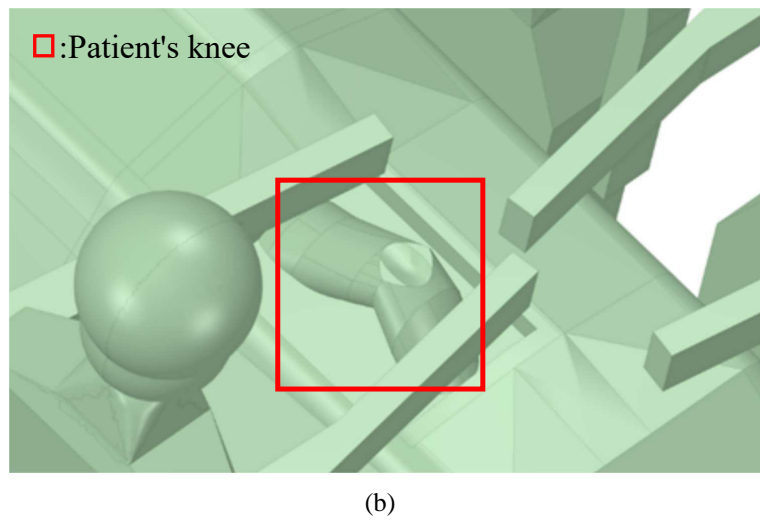
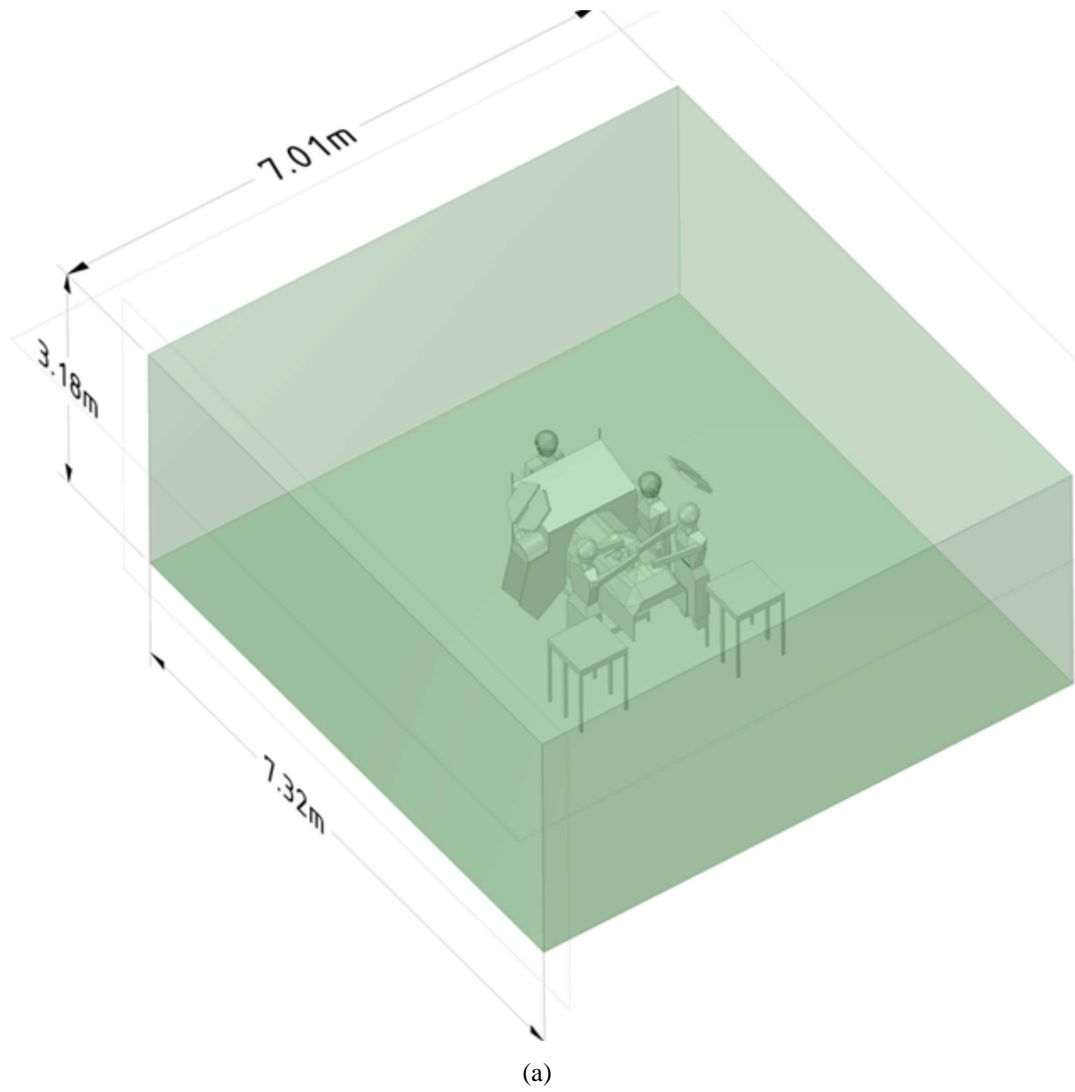


Figure 1: CAD model showing (a) operating room dimensions, and (b) closeup of the patient's knee.

3M™ Bair Hugger™ blower unit (partly visible near the top left corner under the drape).

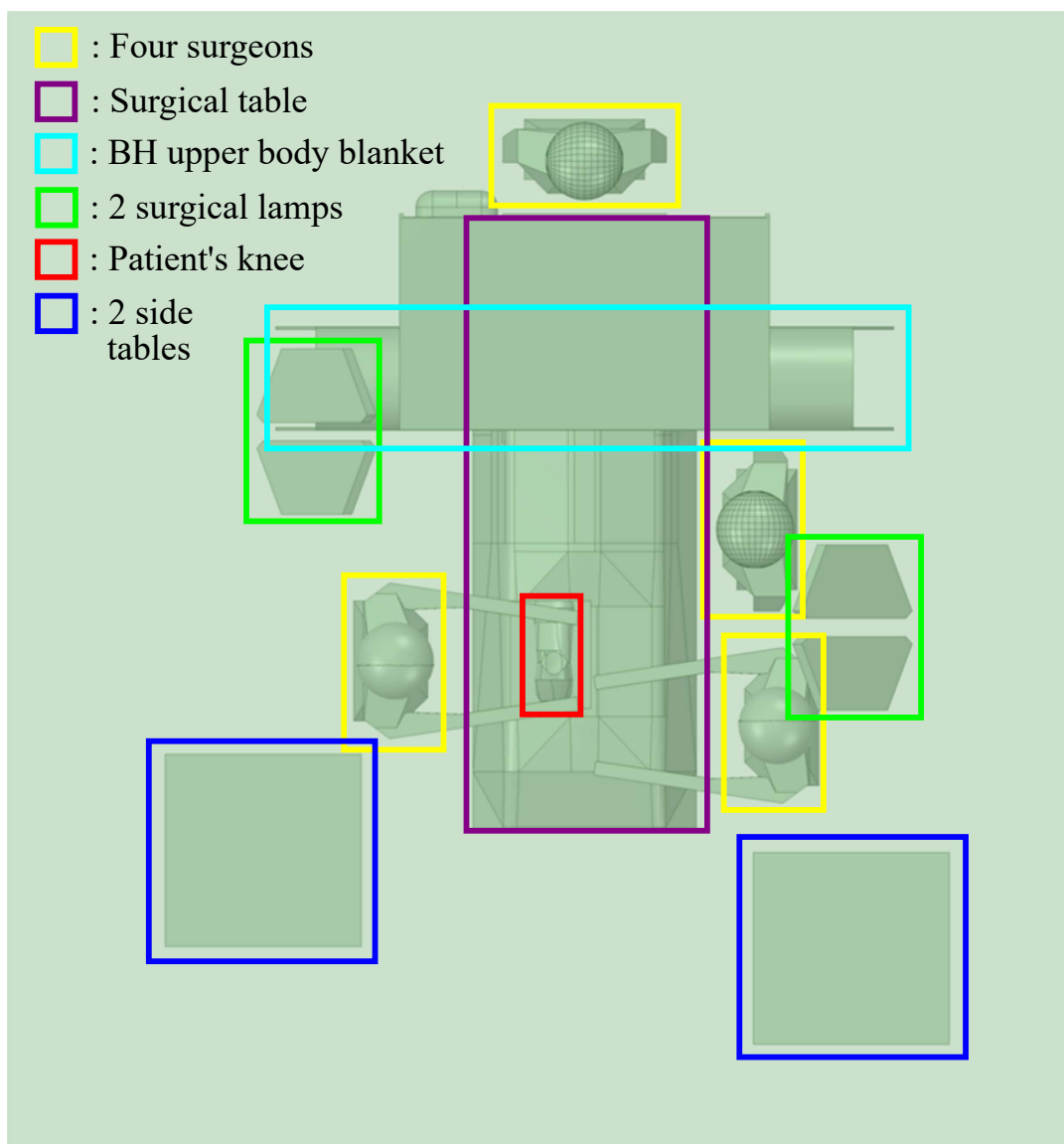


Figure 2: Close-up view of various objects included in the CAD model.

Figure 3 shows a side view of the OR table together with a few key dimensions. The bottom of the OR table is 0.94m above the floor of the room. The drape on the OR table covering the patient's torso is suspended 0.52m above the floor. The 3M™ Bair Hugger™ blower unit is also seen in the bottom right side of the figure.

The drape design from the base CAD model was modified to better represent the drape layout in a real OR room. The modifications mainly focused on using accurate dimensions and shape of the drape near the front end based on an actual picture taken in an OR room as shown in figure 4b. A corresponding CAD model used in the present study is shown in figure 4a. For the CAD model, the

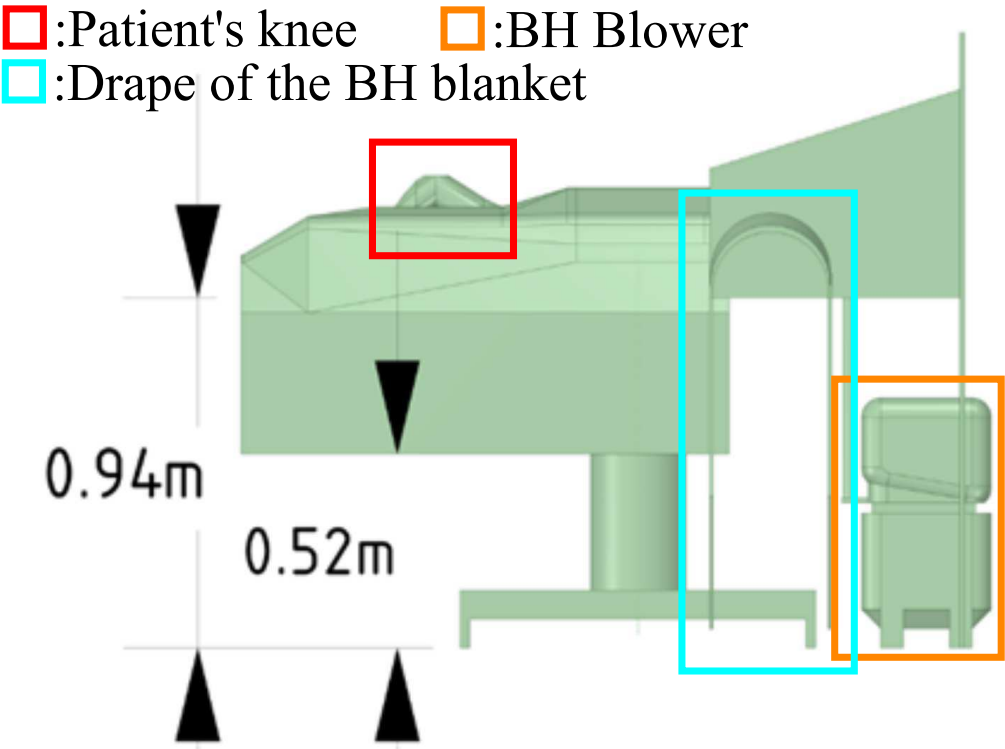


Figure 3: Side view of the OR table with some key dimensions. The 3M™ Bair Hugger™ blower unit is clearly visible on the bottom ride side.

171 front end of the drape was designed to mimic the shape obtained by dimensions A, D, C, E in figure
172 4a. The dimensions in the CAD model are given in both metric and imperial units (in brackets) in
173 this figure to facilitate direct comparison with the real picture on the right. The distance between the
174 vertical bars holding the drape, denoted by dimension F in Figure 4b, was also implemented in the
175 CAD model.

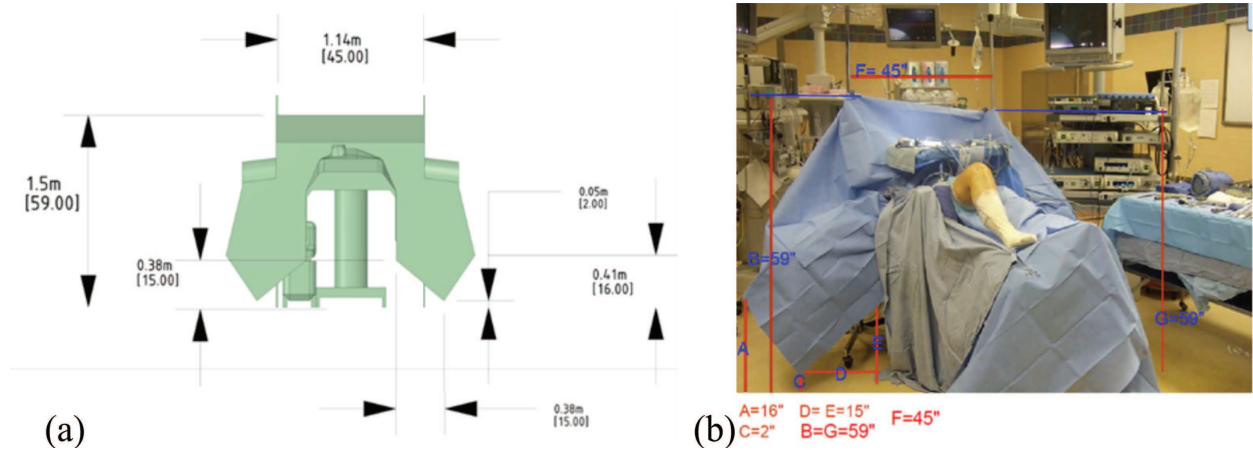


Figure 4: Drape dimensions and configuration: (a) model developed to match the drape dimensions, (b) actual drape picture in an OR room. The dimensions are shown in both metric and imperial units (in brackets).

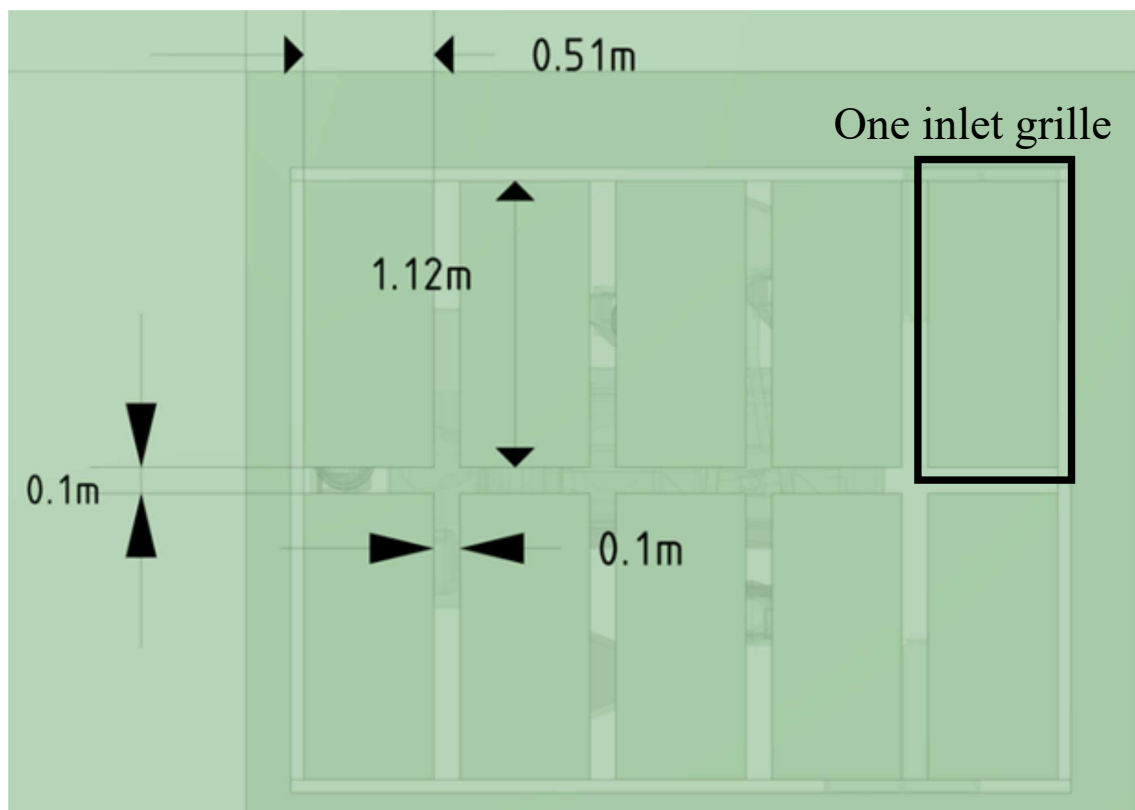


Figure 5: Ten inlet grilles to supply clean filtered air into the OR.

The CAD model included ten inlet grilles (figure 5) for supplying clean filtered air to the OR.

Each inlet grille is 0.51m in width and 1.12m in length. All ten grilles are of the same size. There is a gap of 0.1m between the neighboring grilles at all sides.

There are four exhaust (or outlet) vents, two on each side wall. Figure 6 shows two outlet grilles (with the other two outlets located on the opposite wall). Each outlet grille is 0.71m in width and 0.71m in length.

3 Numerical Simulation

A state-of-the art, fully parallel, unstructured, co-located grid flow solver based on principles of kinetic energy conservation for large-eddy simulation (Moin & Apte, 2006) of turbulent flow in the limit of zero-Mach numbers is used in this study. This solver is MPI-based, uses algebraic multigrid for the pressure Poisson equation, and third-order WENO-based scheme for transport of scalar fields such as temperature. It has been thoroughly validated for a number of different particle-laden turbulent flows (Apte *et al.*, 2003b,a, 2008a, 2009, 2008b) including swirling turbulent flow

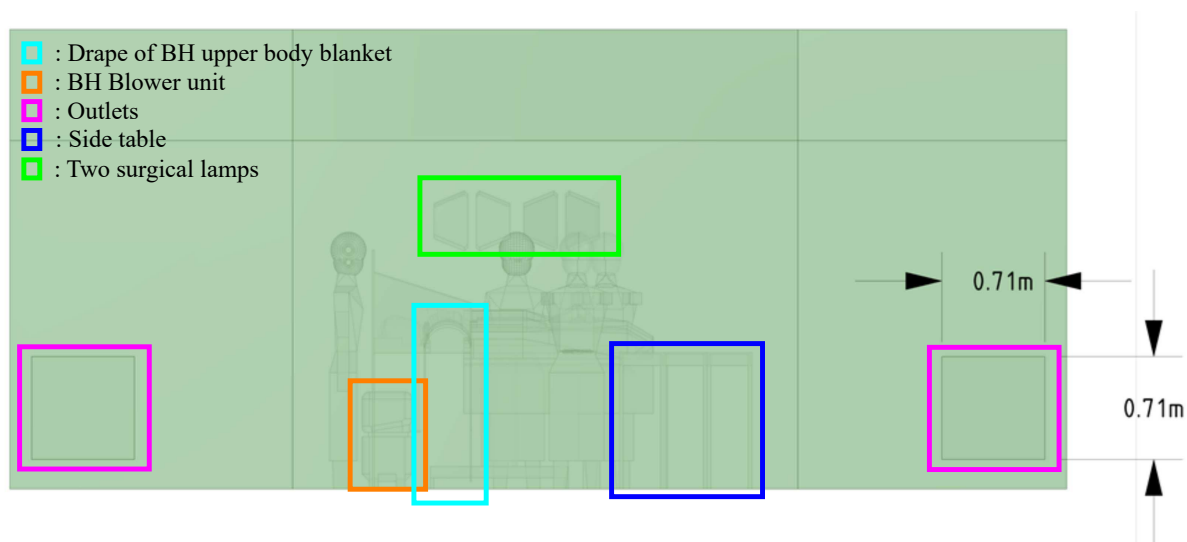


Figure 6: Outlet (exhaust) grilles for air exit from the room. Out of the four outlets in the CAD model, only two are visible in the picture. The other two outlets are on the opposite wall.

in a co-axial combustor, turbulent reacting flow, as well as spray combustion in a realistic Pratt and Whitney gas-turbine combustion chamber (Moin & Apte, 2006; Mahesh *et al.*, 2006).

3.1 Large-eddy Simulation (LES): Introduction and Need

The physics of turbulent air flow containing heated buoyant plumes and laden with inertial particles in a real-life operating room is highly complex. Simulating such flows with predictive capability is difficult as turbulence, by nature, consists of a broad range of length- and time-scales and is inherently three-dimensional. In addition, the geometry of a realistic operating room consists of complex surfaces involving surgeons, operating table, surgical lights, patient, among other. If a probe measures the velocity at a certain location in such a flow, the velocity signal will show a broad range of frequencies and fluctuations around a mean. A typical kinetic energy spectrum obtained via Fourier transform of turbulent velocity field is shown in figure 7, especially for moderate to large Reynolds numbers. The spectrum is broad-band with large amount of kinetic energy per wavenumber present at large scales (small wavenumbers) and small amount of energy present at smaller scales (larger wavenumbers). There also exists an inertial range, scales in this regime simply transfer the energy from larger scales to smaller scales through a process commonly known as the energy cascade (Pope, 2000). As the Reynolds number increases, this spectrum is known to broaden. The largest scales (\mathcal{L}) of motion are typically confined by the size of the domain (for example, size of the inlet jet

or size of the room). However, as the Reynolds number increases, the smallest scales of motion (known as the Kolmogorov scales, η) are reduced until the kinetic energy is dissipated into internal energy by the viscous effects. Owing to this broad range of scales, prediction of turbulent flows at large Reynolds numbers becomes difficult and is only possible if the behavior of all scales of motion is captured properly.

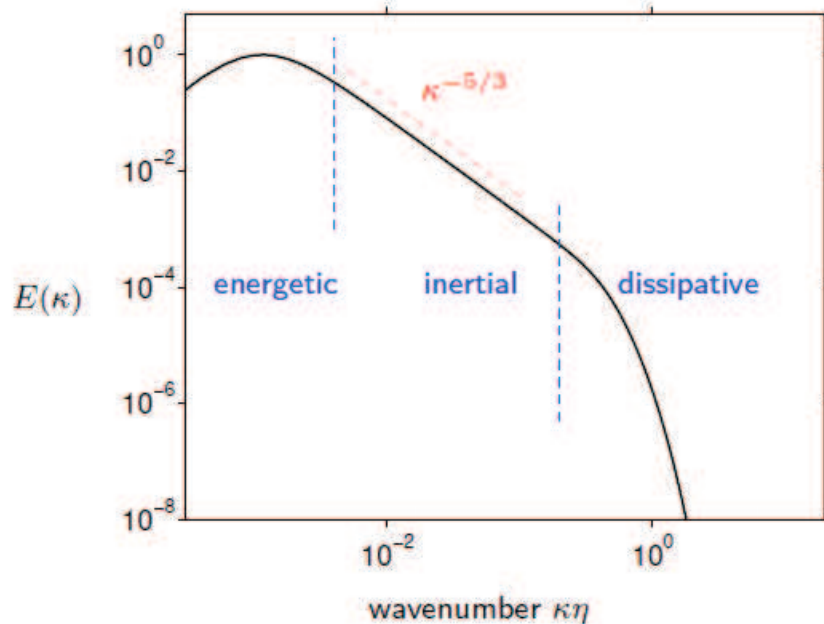


Figure 7: Schematic of a turbulence kinetic energy spectrum showing energy per wavenumber as a function of the wavenumber (Pope, 2000). The inertial range of scales is indicated by the $-5/3$ slope line that separates the energetic large scales and dissipative small scales of turbulence. In DNS, the grid resolution is fine enough to capture all scales, whereas in LES, the grid resolution is coarser (typically 10 times the Kolmogorov length scale), placing the grid cut-off somewhere in the inertial range.

Three basic approaches can be identified for prediction of turbulent flows: (i) direct numerical simulation (DNS), (ii) Reynolds averaged Navier-Stokes (RANS) modeling, and (iii) large-eddy simulation (LES), and are briefly described below.

DNS: In direct numerical simulation (DNS), the Navier-Stokes equations are solved on a computational grid that is fine enough, in space and time, to directly capture *all* the scales associated with the fluid flow motion without requiring any additional models. This means that the computational grid in three-dimensions is small enough to capture the smallest scales of turbulence and the time-step is small enough to capture the smallest time-scale associated with the flow. Using scaling arguments based on the Kolmogorov hypotheses (Tennekes & Lumley, 1972; Pope, 2000) used in the theory of turbulence, it can be shown that for a simple homogeneous, isotropic turbulence in a box, the grid resolution requirement ($\Delta \sim \mathcal{L}/\eta$; where \mathcal{L} is the size of the large, energy-containing

eddies) for DNS varies as $Re_{\mathcal{L}}^{3/4}$, where $Re_{\mathcal{L}}$ is the Reynolds number based on \mathcal{L} and the velocity fluctuations u , in one coordinate. Hence, the total number of mesh points needed in three-dimensions varies as $Re_{\mathcal{L}}^{9/4}$. A simple isotropic turbulence in a box at $Re_{\mathcal{L}} = 2000$, would require computational grid containing about 27M control volumes ($= 300^3$). In addition, based on numerical constraints of a computational solver, for a fluid flow of unit velocity, the grid spacings (Δ) and the time-steps (Δt) are roughly of the same order of magnitude ($CFL = u\Delta t/\Delta \sim 1$) and thus the spatio-temporal resolution will require a computational power that increases as $Re_{\mathcal{L}}^3$. Owing to the grid requirements and associated computational costs, DNS is not practical for realistic engineering applications and is restricted to canonical geometries and flow problems to study the fundamentals of turbulence (Moin & Mahesh, 1998).

RANS: According to the above discussion, the computation of practical turbulent flows relies predominantly on the Reynolds-averaged Navier-Stokes (RANS) equations approach. In RANS, the governing equations are averaged in time to obtain equations for the *time-averaged* velocity field, $\bar{u}(\mathbf{x})$. Thus, in this approach, only the mean velocity field that varies in space is obtained, and all information about the time-dependent fluctuations of the velocity field around the mean flow is lost. Because the momentum equations are non-linear (owing to the inertial, advective terms), a time-average of the non-linear term creates additional quantities that are unknown, giving rise to the classical closure problem of turbulence (Tennekes & Lumley, 1972; Pope, 2000). In order to evaluate these terms, models are introduced wherein the effect of the entire spectrum of turbulence (involving the large, inertial, and small scales shown in Figure 7) is completely modeled. This is usually done by introducing two additional transport equations for the turbulence kinetic energy (k) and the kinetic energy dissipation rate (ε), giving rise to the $k - \varepsilon$ model. It should be noted that the transport equations for k and ε also contain a large number of unknown, unclosed terms which also need to be modeled. The model constants are obtained by fitting the RANS predictions to the experimental data on simple, canonical flows such as wall bounded channel flow, isotropic turbulence, or free-shear flows. Because these models and model constants *are not universal*, using them for a complex flow such as air circulation in an operating room, invariably provides inaccurate results. Experimental data is necessary to adjust the model constants and thus the RANS models are not *predictive*. However, since only the time-averaged velocity field is calculated, the RANS approach is computationally the least expensive because it does not require the spatio-temporal resolution

necessary for the DNS studies. There are modified approaches, wherein the large-time scale variations are captured by solving the RANS equations in an unsteady manner. These unsteady-RANS simulations also suffer from the same hypotheses and models used for the basic RANS and their predictive capability is also poor.

LES: The energy spectrum (figure 7) shows that a substantial portion of the turbulence kinetic energy (TKE) is contained in the large-scales, known as the energy containing scales. In LES, only the contribution of the large, energetic structures to momentum and energy transfer is computed exactly, and the effect of the small scales, also termed as unresolved or subgrid scales, of turbulence is modeled. Since the small scales tend to be more homogeneous, and less affected by the domain boundary conditions as compared to the large eddies, then the subgrid closure models used in LES are universal and can be applied to a range of flows as compared to the RANS closures. Owing to these differences between the LES and RANS approaches, LES has been shown to be far superior to RANS in accurately predicting turbulent mixing of momentum and scalar (Mahesh *et al.*, 2004), pollutant and heat transport, combustion (Pierce, 2001), and particle dispersion (Apte *et al.*, 2003b; Ham *et al.*, 2003).

In LES, the Navier-Stokes (NS) equations are filtered in space (as opposed to time as done in RANS) using a local filter (Gaussian, box, spectral etc.) to obtain a filtered velocity field, $\bar{u}_i(\mathbf{x}, t)$ (Pope, 2000). Using the local grid resolution as a spatial filter, the small, under-resolved scales of turbulence are filtered out. However, applying the filtering operation to the inertial, non-linear terms in the NS equations, gives rise to the closure problem. The resulting additional terms need to be modeled. Most often, the models used to close the unknown terms, known as Reynolds stresses, are based on the same types of assumptions, such as the gradient diffusion hypothesis, as employed in RANS. However, the fact that, in LES, modeling is only applied to capture the effect of unresolved, subgrid scales, which are homogeneous and universal, the closure models work very well in a wide range of problems. A dynamic procedure, typically employed in LES subgrid scale modeling, renders the modeling process completely free of any tuning parameters in contrast to RANS. All constants in the model are obtained directly in the calculations and are not set by the user. As long as the grid resolution is sufficient such that the motion of the energy-containing large eddies is captured correctly, unlike RANS, the LES approach can then be used in a truly predictive manner.

In addition, away from the boundaries, a typical LES grid can be 10 times coarser than a DNS grid in each direction (that is 10 times the Kolmogorov scale), resulting in significant savings in the computational cost. This makes LES an attractive tool compared to the DNS. However, there are still several challenges. Just like DNS, the LES computations are inherently three-dimensional and time-dependent, making the cost of the calculation large as the important large-scale spatio-temporal variations in the flow must still be resolved. In addition, the computational algorithm must not add large amounts of numerical dissipation as it has been shown that dissipative numerical approaches mask the physical dissipation present in turbulent flows and provide inaccurate predictions (Mittal & Moin, 1997; Kravchenko & Moin, 1997). These restrictions typically limits the use of LES to simple, canonical geometries and flows (as free-shear flows (jets, wakes, shear layers), wall bounded channel flows, or flow over backward facing step (Pierce, 2001; Piomelli, 2014)) for which the underlying algorithms are based on a non-dissipative schemes developed for structured Cartesian grids.

Applying LES to the complex and realistic geometries of engineering applications such as the the operating room; including the operating table, surgeons, patient and other equipment, or other applications such as gas-turbine combustors, propellers, among others, requires use of arbitrary shaped unstructured meshes. In recent years; however, considerable progress has been made in handling complex configurations and unstructured grids accurately (Piomelli, 2014). Mahesh *et al.* (2004); Ham *et al.* (2003); Mahesh *et al.* (2006) have developed a numerical algorithm for high-fidelity simulations of incompressible, variable density flows on unstructured grids. A novelty of their algorithm is that it is discretely energy-conserving which makes it robust at high Reynolds numbers *without numerical dissipation*. This makes LES applicable to complex configurations and it has been successfully used to simulate multiphase, spray combustion processes in a realistic Pratt and Whitney gas-turbine combustion chamber (Moin & Apte, 2006; Mahesh *et al.*, 2006; Apte *et al.*, 2009). These simulations are still computationally intensive, often requiring 3–4 weeks of simulation on parallel supercomputers, however, the detailed data obtained from the simulations are of significant importance to researchers and engineers since such information could not be obtained from laboratory experiments. This has led several gas-turbine industries, who generally use RANS in their design cycle, to switch from RANS-based approaches to LES.

Furthermore, turbulent flows laden with dispersed particles (either solid particles, or droplets or

bubbles) involve the complexity of capturing the dynamics of turbulence as well as that of the dispersed phase. The physics of particle-turbulence interactions is complex (Elghobashi, 1994, 2006), and depending upon the magnitudes of the particle relaxation times relative to the Kolmogorov time scales, heavier-than-fluid particles (solid particles, droplets, squames) can exhibit behavior such as preferential clustering on the edges of vortices (Eaton & Fessler, 1994; Rouson & Eaton, 2001; Kulick *et al.*, 2006; Reade & Collins, 2000; Eaton & Segura, 2006), whereas, lighter-than-fluid particles (bubbles) can break the vortical structures (Ferrante & Elghobashi, 2004; Druzhinin & Elghobashi, 1998; Ferrante & Elghobashi, 2007; Sridhar & Katz, 1999).

RANS is not capable of capturing this complex physics of particles interacting with turbulence because only the mean velocity field is computed by RANS, yet it is commonly used owing to its low cost. However, if the objective is to accurately simulate the dispersion of inertial particles in a turbulent flow, then a three-dimensional, instantaneous velocity field is necessary to calculate the forces on the particles. Inertial particle trajectories and dispersion are strongly influenced by the spatio-temporal variations in the velocity fields. Hence, using only the mean velocity field provides inaccurate dispersion characteristics. An improved RANS to capture the transient effects uses a model for particle motion that utilizes the local turbulence kinetic energy and introduces some randomness (typically a Gaussian distribution) in the particle equations (Sommerfeld *et al.*, 1992) is necessary. Recent work on the dispersion of squames in an operating room and the effect of different inlet air flow conditions used RANS together with such a stochastic, Lagrangian particle-tracking algorithm (Memarzadeh & Manning, 2002). Such a model must be tuned by the user to calculate different particle-laden flows and can behave differently in free-shear versus wall-bounded flows. As can be seen from the results presented by Sommerfeld *et al.* (1992); Chen & Pereira (1998), particle dispersion predicted using a RANS approach for turbulent flows in a wide range of applications involving swirling, separated flows do not agree with the experimental data. However, the same flowfields computed using LES (Apte *et al.*, 2003b; Moin & Apte, 2006; Apte *et al.*, 2008b, 2009) show considerably better predictive capability and agree with the experimental data very well. In LES, the resolved instantaneous velocity field, which varies in time and space, at the particle location is used to compute the forces on the particles as opposed to the time-averaged velocity in RANS. Accordingly, the effect of the energetic, turbulence scales (of the order of the grid resolution and larger) are completely captured in LES, thus predicting its impact on particle dispersion directly.

To summarize, it is essential to use LES instead of RANS to accurately predict the air circulation and dispersion of squames in an operating room for the following reasons:

- LES provides a three-dimensional, instantaneous flow field (velocity, pressure, temperature) of the resolved, energetic, large-scales, and only models the effect of the unresolved, subgrid (small) scales of turbulence. The subgrid scales tend to be more homogeneous, and less affected by the domain boundary conditions and thus allow the appropriate use of the eddy-viscosity models to calculate their stresses. RANS, on the other hand, only calculates the time-averaged velocity field and models the effect of all the scales of turbulence on the mean flow, resulting in unrealistic flow predictions.
- The subgrid model constants used in LES can be obtained dynamically, thus making LES truly predictive without any user-defined tuning parameters, whereas RANS model constants are not universal and often require manual tuning.
- LES is considerably more accurate in predicting passive as well as inertial particle dispersion since the instantaneous, three-dimensional resolved velocity field is available for computing the forces on the particles. In RANS, a random perturbation must be added to the mean velocity field to construct an artificial, time-dependent, three-dimensional velocity field needed to calculate the particle motion. This renders the calculation of particle dispersion highly inaccurate.

3.2 Governing Equations

The air flow in an operating room involves temperature variations within the room owing to various sources of heat; such as the operating room lamps, heat radiated from the medical personnel bodies, hot air discharged from a blower system, among others. The local temperature variations change the local air density. However, since the air flow in the room is low-speed (maximum velocity on the order of, $u \sim 0.5$ m/s compared to speed of sound of around, $c \sim 343$ m/s), the Mach number (u/c), that represents the ratio of acoustic to convective time-scales, is small ($\ll 0.01$). Small Mach numbers mean that the convective time-scales are much larger than acoustic time-scales, and thus the compressibility effects are negligibly small. Under these conditions, the variable-density equations in the limit of zero-Mach number are valid and the pressure field at any point within the

domain and time can be split into a bulk thermodynamic pressure, P_0 , and the dynamic pressure p that appears in the momentum equation,

$$P(x, t) = P_0(t) + p(x, t). \quad (1)$$

The background thermodynamic pressure (P_0) for the operating room is assumed constant and equal to the atmospheric pressure, $P_0 = 1$ atm.. Accordingly, the density of the air (assumed as ideal gas) varies only with the local temperature field according to the equation of state as,

$$\rho = \frac{P_0 R_{\text{universal}} T}{M_{\text{air}}}, \quad (2)$$

where $R_{\text{universal}}$ is the universal gas constant, M_{air} is the molecular mass of the air, and T is the absolute temperature. The governing equations for large-eddy simulation of turbulent flows with variable density in the limit of zero Mach number are given below.

3.2.1 Gas-phase equations

The spatially filtered, Favre averaged, governing equations used for large-eddy simulation of particle-laden, turbulent air flow with heat transfer and buoyancy effects are given as,

$$\frac{\partial \bar{\rho}_g}{\partial t} + \frac{\partial \bar{\rho}_g \tilde{u}_j}{\partial x_j} = 0. \quad (3)$$

$$\frac{\partial \bar{\rho}_g \tilde{u}_i}{\partial t} + \frac{\partial \bar{\rho}_g \tilde{u}_i \tilde{u}_j}{\partial x_j} = -\frac{\partial \bar{p}}{\partial x_i} + \frac{\partial}{\partial x_j} (2\bar{\mu} \tilde{S}_{ij}) - \frac{\partial q_{ij}^r}{\partial x_j} + (\bar{\rho}_g - \rho_0) g_i, \quad (4)$$

$$\frac{\partial \bar{\rho}_g \tilde{h}}{\partial t} + \frac{\partial \bar{\rho}_g \tilde{h} \tilde{u}_j}{\partial x_j} = \frac{\partial}{\partial x_j} \left(\bar{\rho}_g \tilde{\alpha}_h \frac{\partial \tilde{h}}{\partial x_j} \right) - \frac{\partial q_{hj}^r}{\partial x_j}, \quad (5)$$

where

$$\tilde{S}_{ij} = \frac{1}{2} \left(\frac{\partial \tilde{u}_i}{\partial x_j} + \frac{\partial \tilde{u}_j}{\partial x_i} \right) - \frac{1}{3} \delta_{ij} \frac{\partial \tilde{u}_k}{\partial x_k}. \quad (6)$$

Here, $\bar{\rho}_g$ is the filtered density, \tilde{u}_i is the Favre averaged velocity field, \bar{p} is the filtered pressure, μ is the dynamic viscosity, $\alpha_h = k/\bar{\rho}_g C_p$, is the thermal diffusivity (k is the conductivity and C_p the specific heat at constant pressure), g_i is the gravitational acceleration, and \tilde{S}_{ij} is the filtered rate of

strain. In addition, the specific enthalpy, h , is given as,

$$h = \frac{T - T_0}{T_0}, \quad (7)$$

where T is the local temperature. Also, T_0 and ρ_0 are the temperature and density fields corresponding to the air inlet conditions and pressure of P_0 .

The additional terms q_{ij}^r and q_{hj}^r in the momentum and the enthalpy equations, respectively, represent the subgrid-scale stress and energy flux and are modeled using the dynamic Smagorinsky model by Moin *et al.* (1991) as demonstrated by Pierce & Moin (1998a). The unclosed terms in Eqs. (4-5) are modeled using the gradient-diffusion hypothesis with eddy-viscosity/diffusivity,

$$q_{ij}^r = \overline{\rho_g}(\tilde{u}_i\tilde{u}_j - \widetilde{u_iu_j}) = 2\mu_t\tilde{S}_{ij} - \frac{1}{3}\overline{\rho_g}q^2\delta_{ij}, \quad (8)$$

$$q_{hj}^r = \overline{\rho_g}(\tilde{h}\tilde{u}_j - \widetilde{hu_j}) = \overline{\rho_g}\alpha_t\frac{\partial\tilde{h}}{\partial x_j}, \quad (9)$$

where the eddy viscosity (μ_t) and eddy thermal diffusivity α_t are modeled as,

$$\mu_t = C_\mu\overline{\rho_g}\bar{\Delta}^2\sqrt{\widetilde{S_{ij}S_{ij}}}, \quad (10)$$

$$\overline{\rho_g}\alpha_t = C_\alpha\overline{\rho_g}\bar{\Delta}^2\sqrt{\widetilde{S_{ij}S_{ij}}}. \quad (11)$$

The coefficients C_μ , C_α are calculated dynamically at each time-step and for each grid point using the dynamic procedure as outlined by Germano *et al.* (1991). For the unstructured grids, the filter width $\bar{\Delta}$ is taken as $V_{cv}^{1/3}$ where V_{cv} is the volume of the grid element.

3.2.2 Equations for calculating the trajectories of individual squames

The human skin cells or squames typically are disc-shaped with a diameter ranging from 4–20 μm and a thickness of 3–5 μm with density close to that of liquid water (1000kg/m³) (Noble *et al.*, 1963; Noble, 1975; Snyder, 2009). Although the squames shape is more disc-like, in the present work they are considered as non-deformable, spherical in shape. A spherical shape is assumed as the dynamics of the spherical particle is easier to calculate and also the lift and drag forces on small particles of disc or spherical shape are not significantly different. The diameter of the spherical

379 particle is assumed to be 10 microns and matches an average settling velocity of a disc-shaped
 380 particle considering the mean flow normal and parallel to the disc (see Appendix A). Recent work
 381 using RANS model by [Memarzadeh & Manning \(2002\)](#); [Memarzadeh \(2003\)](#) also approximates the
 382 squames particles as spherical with a size of 10 microns.

An Eulerian-Lagrangian approach is used wherein individual squames trajectories will be tracked in a Lagrangian frame. The different forces on the particles will be calculated using standard closure laws. The effect of the particles on the fluid flow will be negligible owing to their small concentration and thus a one-way coupling approach is adopted, wherein the squame motion uses the fluid flow parameters (velocity) to compute the forces, however, the effect of squames on the fluid momentum is neglected ([Elghobashi, 1994, 2006](#)). In addition, since the volume fraction of the squames in an operating room is not very large ($\ll 10^{-3}$), collisions amongst the squames are neglected. The squame particle motion equation is that of [Maxey & Riley \(1983\)](#),

$$\frac{d}{dt}(\mathbf{x}_p) = \mathbf{u}_p \quad (12)$$

$$m_p \frac{d}{dt}(\mathbf{u}_p) = \mathbf{F}_g + \mathbf{F}_d + \mathbf{F}_\ell + \mathbf{F}_{am} + \mathbf{F}_p + \mathbf{F}_H, \quad (13)$$

383 where \mathbf{x}_p is the particle (squames) centroid location, m_p is the mass of an individual particle, \mathbf{u}_p is
 384 the particle velocity, \mathbf{F}_g is the gravitational force, \mathbf{F}_d is the drag force, \mathbf{F}_ℓ is the lift force, \mathbf{F}_{am} is the
 385 added mass force, \mathbf{F}_p is the pressure force, and \mathbf{F}_H is the Basset history force.

386 The large ratio of particle density to air density, ρ_p/ρ_g , renders both the Basset history force
 387 and the added mass force negligible compared to the drag force. The ratio of the Saffman lift to
 388 the drag force is given by, $F_\ell/F_{drag} \sim \rho_g d_p^2 (du/dy)^{1/2}/\mu$, and is dependent on the shear rate and
 389 particle diameter. For particles with small diameter and low inertia this force can also be neglected
 390 in comparison to the drag force ([Crowe *et al.*, 1996](#); [Saffman, 1965](#)). However, the lift force is in-
 391 corporated in our calculations to account for the saltation of the squame particles from the operating
 392 room floor. The gravity, drag and lift forces are given as,

$$\mathbf{F}_g = (\rho_p - \bar{\rho}_g) \mathcal{V}_p \mathbf{g}; \quad \mathbf{g} = -9.81 \mathbf{m}/s^2 \quad (14)$$

$$\mathbf{F}_d = -\frac{1}{8}C_d\bar{\rho}_g\pi d_p^2|\mathbf{u}_p - \tilde{\mathbf{u}}_{g,p}|(\mathbf{u}_p - \mathbf{u}_{g,b}); \quad C_d = \frac{24}{Re_p}(1 + 0.15Re_p^{0.687}), \quad (15)$$

$$\mathbf{F}_\ell = -C_\ell m_p \frac{\bar{\rho}_g}{\rho_p}(\mathbf{u}_p - \tilde{\mathbf{u}}_{g,p}) \times (\nabla \times \tilde{\mathbf{u}}_g)_p; \quad C_\ell = \frac{1.61 \times 6}{\pi d_p} \sqrt{\frac{\mu}{\bar{\rho}_g} |(\nabla \times \tilde{\mathbf{u}}_g)_p|} \quad (16)$$

where the subscript p represents the squame particle, $\tilde{\mathbf{u}}_{g,p}$ represents the fluid velocity interpolated at the particle center location, \mathcal{V}_p is the particle volume, d_p is the particle diameter, $Re_p = \bar{\rho}_g|\mathbf{u}_p - \tilde{\mathbf{u}}_{g,p}|d_p/\mu$ is the particle Reynolds number, C_d is the drag coefficient, C_ℓ is the lift coefficient.

The gas-phase velocity, $\tilde{\mathbf{u}}_g$, in the particle equations above, is computed at individual particle locations within a control volume using a generalized, tri-linear interpolation scheme for arbitrary shaped elements. Introducing higher order accurate interpolation is straight forward; however, it was found that tri-linear interpolation is sufficient to represent the gas-phase velocity field at particle locations. As mentioned earlier, in LES of particle-laden flows, the particles are presumed to be *subgrid*, and the particle-size is smaller than the filter-width used. The gas-phase velocity field required in equations (12) and (13) is the total (unfiltered) velocity, however, only the filtered velocity field is computed in equations (4). The direct effect of the unresolved (subgrid) velocity fluctuations on particle trajectories depends on the particle relaxation time-scale, and the subgrid kinetic energy. Pozorski & Apte (2009) performed a systematic study of the direct effect of subgrid scale velocity on particle motion for forced isotropic turbulence. It was shown that, in poorly resolved regions, where the subgrid kinetic energy is more than 30%, the effect on particle motion is more pronounced. A stochastic model reconstructing the subgrid-scale velocity in a statistical sense was developed (Pozorski & Apte, 2009). However, in well resolved regions, where the amount of energy in the subgrid scales is small, this direct effect was negligible. In the present work, the direct effect of subgrid scale velocity on the droplet motion is neglected. However, it should be noted that the particles *do feel* the subgrid scale stresses through the subgrid model that affects the resolved velocity field. For well-resolved LES of swirling, separated flows with the subgrid scale energy content much smaller than the resolved scales, the direct effect is shown to be small (Apte *et al.*, 2003b, 2009). This is the main advantage of LES as compared to RANS. In RANS, only the time-average mean velocity is available, and all scales of turbulence affecting the instantaneous fluctuations around the mean

must be modeled. Approximating the effect of turbulent fluctuations on the particle dispersion is thus necessary for RANS, whereas, it is implicitly accounted for in the LES.

Equations (12,13) are integrated using a fourth-order Runge-Kutta time-stepping algorithm. After obtaining the new particle positions, the particles are relocated, particles that cross interprocessor boundaries are duly transferred, boundary conditions on particles crossing boundaries are applied, source terms in the gas-phase equation are computed, and the computation is further advanced. Solving these Lagrangian equations thus requires addressing the following key issues: (i) efficient search and location of particles on an unstructured grid (ii) interpolation of gas-phase properties to the particle location for arbitrarily shaped control volumes (iii) inter-processor particle transfer. The details on efficiently locating the particles on unstructured grids, search algorithms for particles, and interpolation schemes can be found in the work by Apte *et al.* (2003b, 2009).

In addition, if the squames impact internal boundaries, a simple, perfectly elastic specular reflection is assumed wherein the squames reverse the wall-normal velocity and preserve the wall-tangential velocity. If the squames impact the patient's knee or the inlet (suction port) of the 3MTM Bair HuggerTM blower system, they are assumed to stick to the surface and are no longer advanced in the computations.

3.3 Computational grid

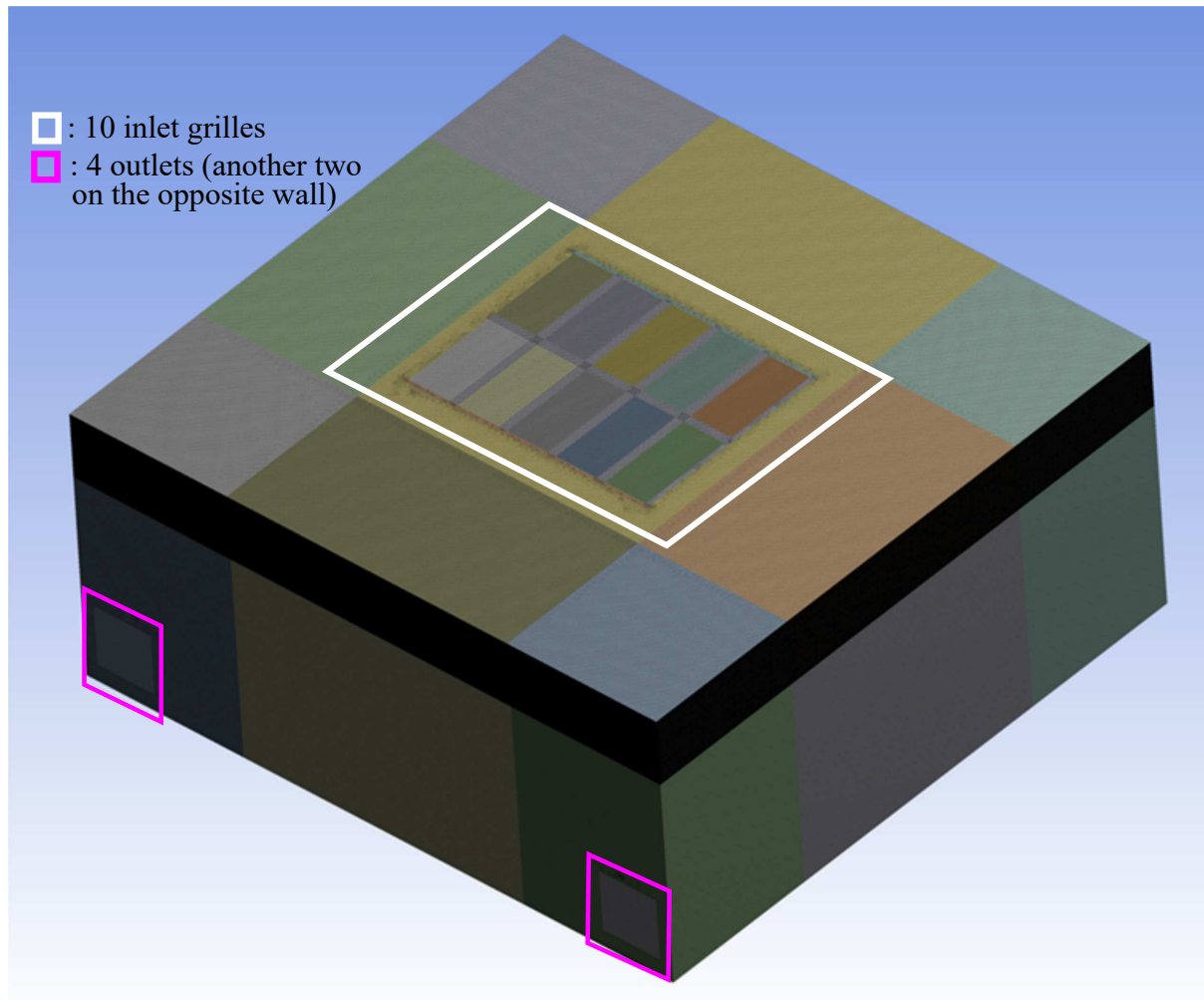
Use of high quality computational mesh is critical in LES for accurate prediction of the turbulent flow, but also having a stable numerical solution. However, to handle complex configurations, use of hybrid elements involving tetrahedrons, pyramids, hexagons and wedges, etc. is common in a typical computational grid. This helps with the grid generation surrounding complex features such as the operating table, the surgeons, the patient and the drape, for example. The transitions from one type of grid element to another; however, can lead to skewed elements. It is thus critical that the numerical algorithm be robust, stable and accurate at high Reynolds numbers on skewed or bad grid elements. A numerical algorithm developed for arbitrary shaped unstructured grids (Mahesh *et al.*, 2004; Ham *et al.*, 2003; Ham & Iaccarino, 2004; Mahesh *et al.*, 2006) that is based on kinetic energy conservation principles offers the much needed robustness and accuracy on such grids without resorting to explicit artificial dissipation. As discussed below, we use a research solver based on

such an algorithm.

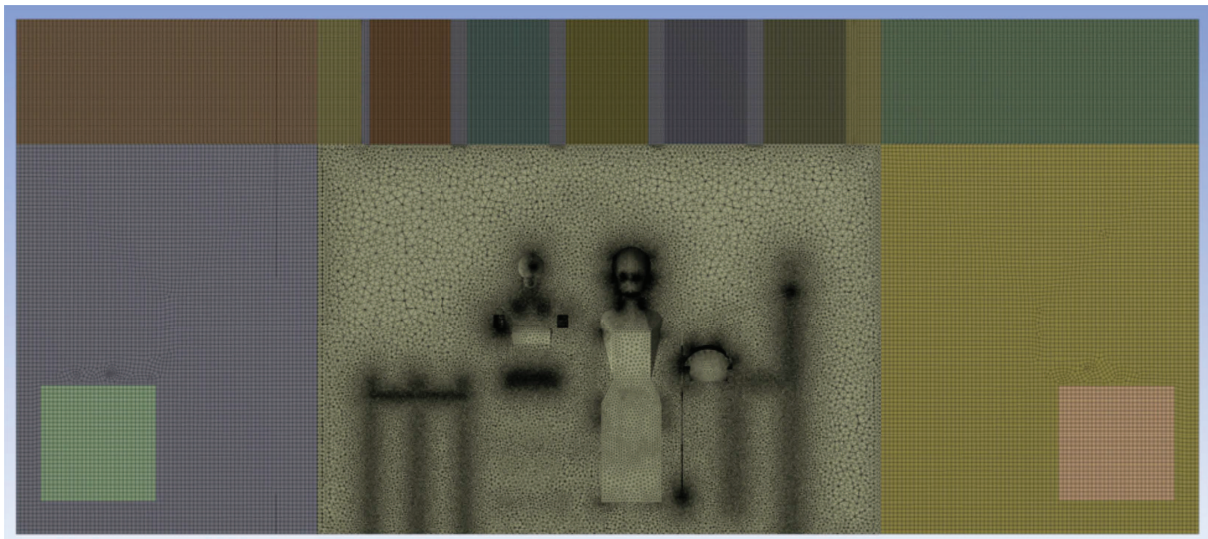
For the present study, a computational mesh (figure 8) was generated using the CAD model described earlier to facilitate predictive large eddy simulations. The mesh was generated using both tetrahedral and hexahedral cells. The transition of mesh from tetrahedral cells to hexahedral cells was done using a combination of pyramid and wedge type cells. Care was taken to generate a computational grid that minimizes the grid skewness as much as possible. As shown below, in the regions away from the complex OR configuration involving the surgeons, the tables, the patient and the drape, a mostly hex-dominant mesh is used. As one approaches closer to the operating table, the computational grid is transitioned to a predominantly tetrahedra-based mesh (see figure 8b). The total mesh count for the computational domain is about 66 million.

Figure 9 shows the grid resolution near the air inlet cross-sections. The grid is appropriately refined to capture the shear layer generated by the inlet flow between the grilles. The mesh surrounding the OR table, patient, surgeons, side tables, the blower, and surgical lamps is predominantly tetrahedral. The tetrahedral mesh was carefully refined to capture surface curvature. Extra refinement was performed near surfaces which were in close proximity to other surfaces. This enhanced mesh refinement is to ensure that the effect of surface shapes on the flow and particles going around them will be captured by the simulation (figure 10a,b.)

As is shown in the above figures, a high quality mesh was generated for the present LES investigation. The minimum tetrahedral cell size (defined as cube root of the cell volume) used near all key regions such as drape, patient, operating bed, surgeons, etc. was around 1mm. Smallest grid spacing in proximity regions resolving the gaps between closely placed surfaces is 0.7mm. The coarsest tetrahedral cell size used away from the key regions is 2.5cm. As mentioned earlier in the report a fine mesh was used near the inlet regions to resolve the flow entering the operating room. A uniform hexahedral cell size of 2.5cm was used to resolve the air inlet grille faces with 20 cells along its width and 44 cells along its length. The gaps between the inlet grilles were resolved using a finer mesh with each cell size of 0.63cm. To capture the inlet air flow structures properly, a refined uniform mesh of 0.38cm was used along the flow direction. Finally, a uniform cell size of 2.5cm was used to resolve each outlet grille with 28 cells along its width and 28 cells along its length. Various mesh metrics were checked to ensure that the quality of the generated mesh was good. Figure 11a shows histogram plot of cell skewness in the mesh. The average skewness was

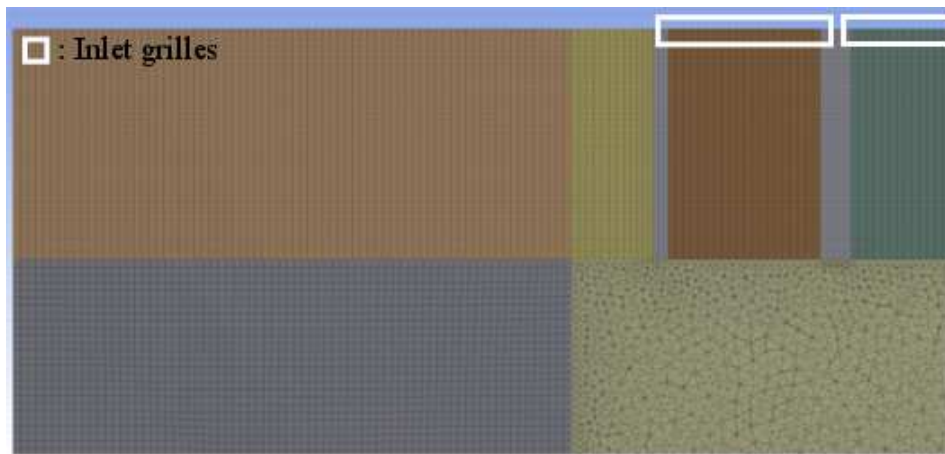


(a)

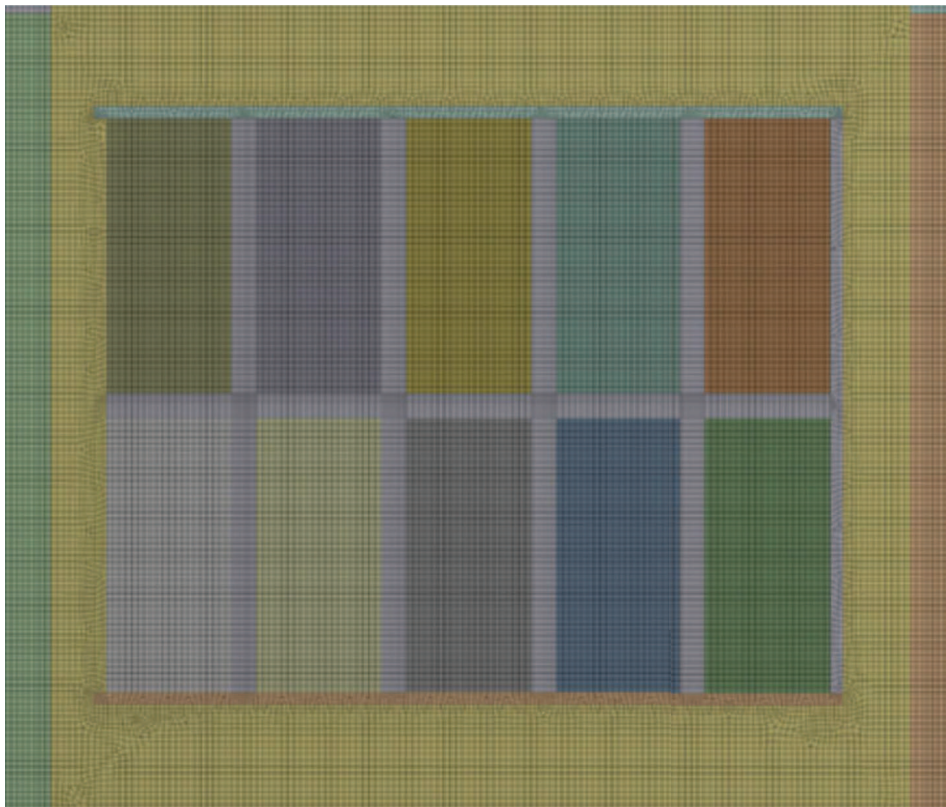


(b)

Figure 8: Computational mesh for the operating room model consisting of about 66M hybrid grid elements consisting of hexagons, tetrahedrons, pyramids and wedges: (a) the full 3D mesh, (b) cross-sectional slice showing hex-dominant mesh in the inlet and outlet regions and a tetrahedral mesh near the operating table.

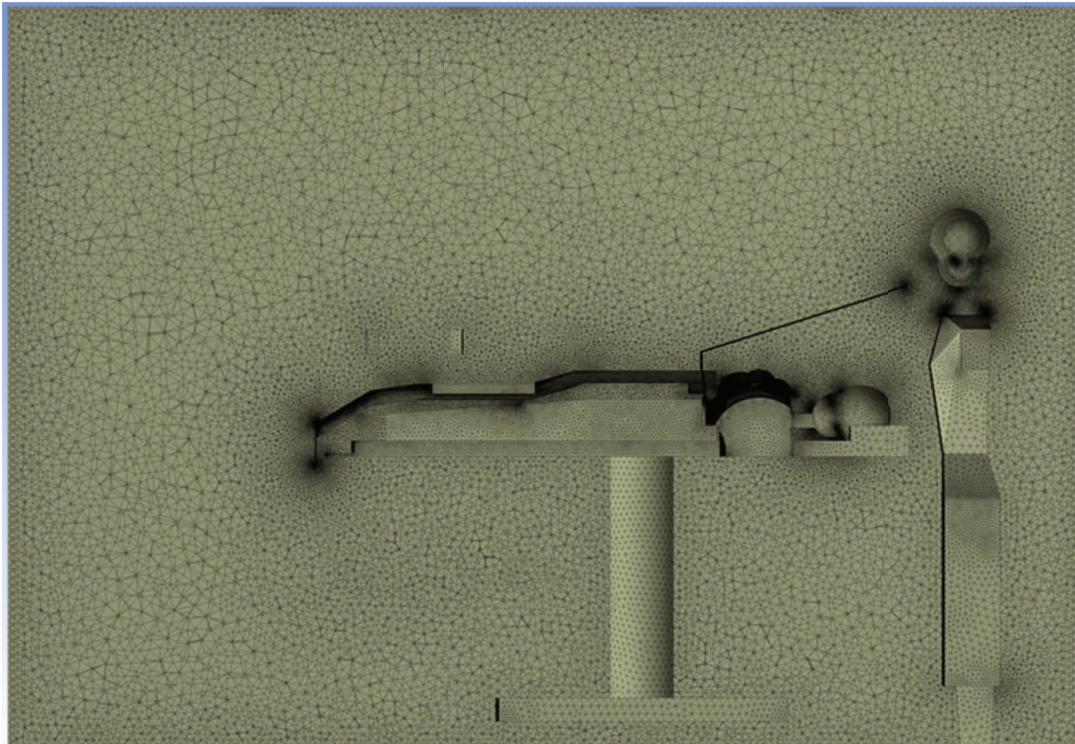


(a)

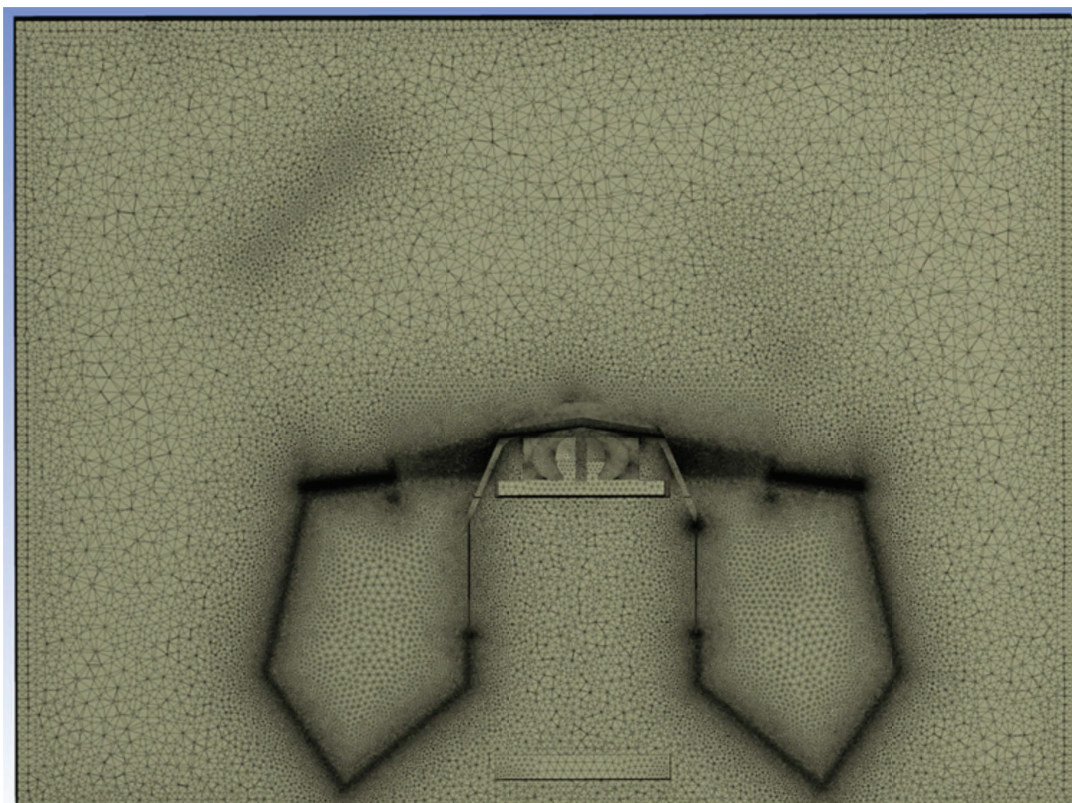


(b)

Figure 9: A cross section cut showing fine mesh near the ceiling of the room: (a) top view zoom-in, (b) top view showing all air inlet grilles.



(a)



(b)

Figure 10: Mesh refinement near curved surfaces and surfaces that are in close proximity to others: (a) side view showing the entire operating table, (b) side view showing drapes.

0.14 and with maximum skewness was 0.91. Only 0.018% of cells had total skewness greater than 0.8 indicating the high quality of cells in the mesh. Another mesh metric that was checked was the aspect ratio of cells. The maximum aspect ratio was 16.2 and the average cell aspect ratio was 2.9, which indicate that a majority of cells in the mesh were mostly uniform (see figure 11b).

3.4 Boundary Conditions

This subsection provides details of all boundary conditions used in the calculation, starting with operating room (OR) air inlet conditions, heat sources, BH hot air blower inflow (suction) and outflow, and OR air outlet conditions.

3.4.1 Inlet boundary conditions

The dimensions of the operating room are shown in Table 1. As shown, there are 10 inlet grilles supplying air. The net supply air volumetric flow rate, \dot{V} , is $1.10436 \text{ m}^3/\text{s}$ ($0.39 \text{ ft}^3/\text{s}$). Using the inlet flow rates, the air changes per hour (ACH) of the room is calculated as follows,

$$\text{ACH} = \dot{V} \times 3600 / (LWH) = 24.45 \text{ per hour}, \quad (17)$$

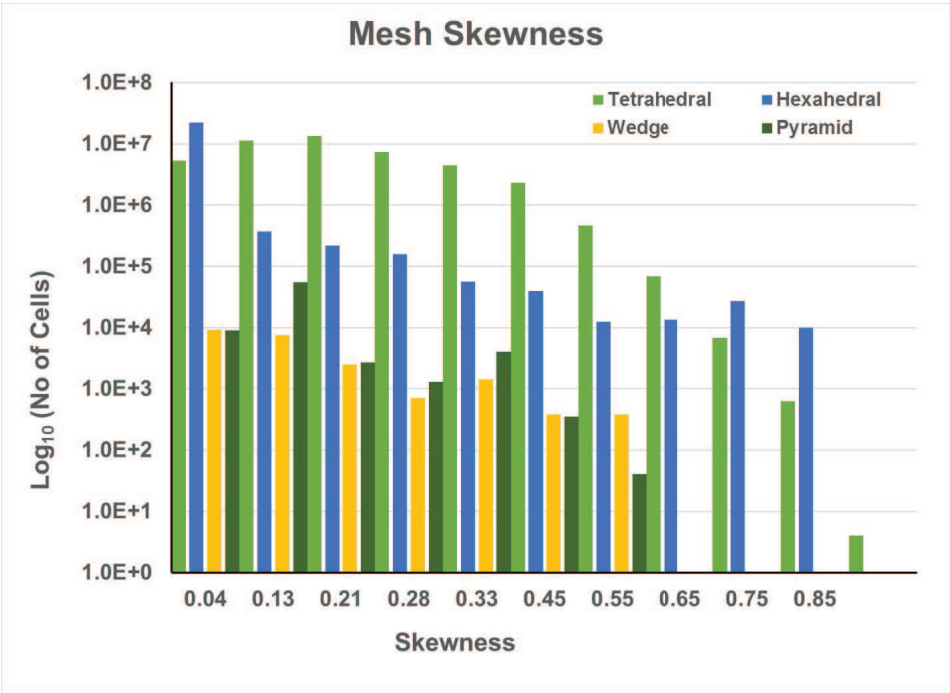
where L , W and H are the room length (in x), width (in y) and height (in z) directions. The ACH is according to the ASHRAE handbook [Memarzadeh & Manning \(2002\)](#), which suggests the ACH to be about 25 per hour for an operating room with recirculating air system.

The inlet boundary conditions are imposed at the 10 grilles on the ceiling of the operating room to model the inlet part of the forced ventilation system. The average inlet velocity, \bar{U}_{in} , is found to be 0.1933 m/s based on,

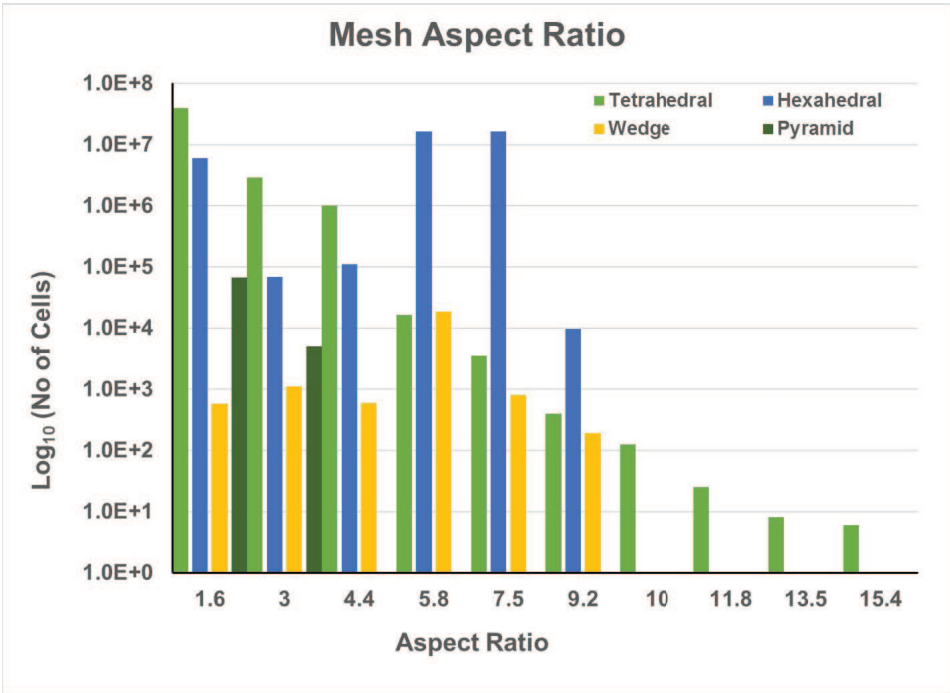
$$\bar{U}_{in} = \dot{V} / (10 \times A_{grill}), \quad (18)$$

where A_{grill} is the area of the cross-section ($1.12 \times 0.51 = 0.5712 \text{ m}^2$) and $\dot{V} = 1.1044 \text{ m}^3/\text{s}$ ($39 \text{ ft}^3/\text{s}$) is the net inlet volumetric flow rate. The air temperature of the inlet flow, T_{in} , is set to 59°F (15°C).

Based on Reynolds number for the inlet grilles, $Re_{in} = 9226.54$ (Table 1), the inlet flow is turbulent. In order to have completely predictive numerical simulation and to minimize the effect of boundary conditions, it is necessary to impose a proper, fully developed turbulent flow field at the in-



(a)



(b)

Figure 11: Statistics histograms of the quality of mesh used in the computation: (a) skewness, (b) aspect ratio.

Table 1: Operating room characteristics

Parameter	Value
Room dimensions [m], L, W, H	$7.315 \times 7.00 \times 3.175$
Supply air flow rate [m^3/s], \dot{V}	1.10436
ACH [1/hr]	24.45
Room air temperature [$^{\circ}\text{C}$]	15
Inlet air density [kg/m^3], ρ_{in}	1.225
Supply air temperature [$^{\circ}\text{C}$]	15
Room air pressure [Pa]	1.0131×10^5
Grille dimensions [m]	1.12×0.51
Grille Area [m^2]	0.5712
Grille hydraulic diameter [m], D_h	0.7
Mean inlet velocity [m/s], \bar{U}_{in}	0.1933
Inlet Reynolds number, $Re_{in} = \frac{\rho_{in} \bar{U}_{in} D_h}{\mu}$	9226.54

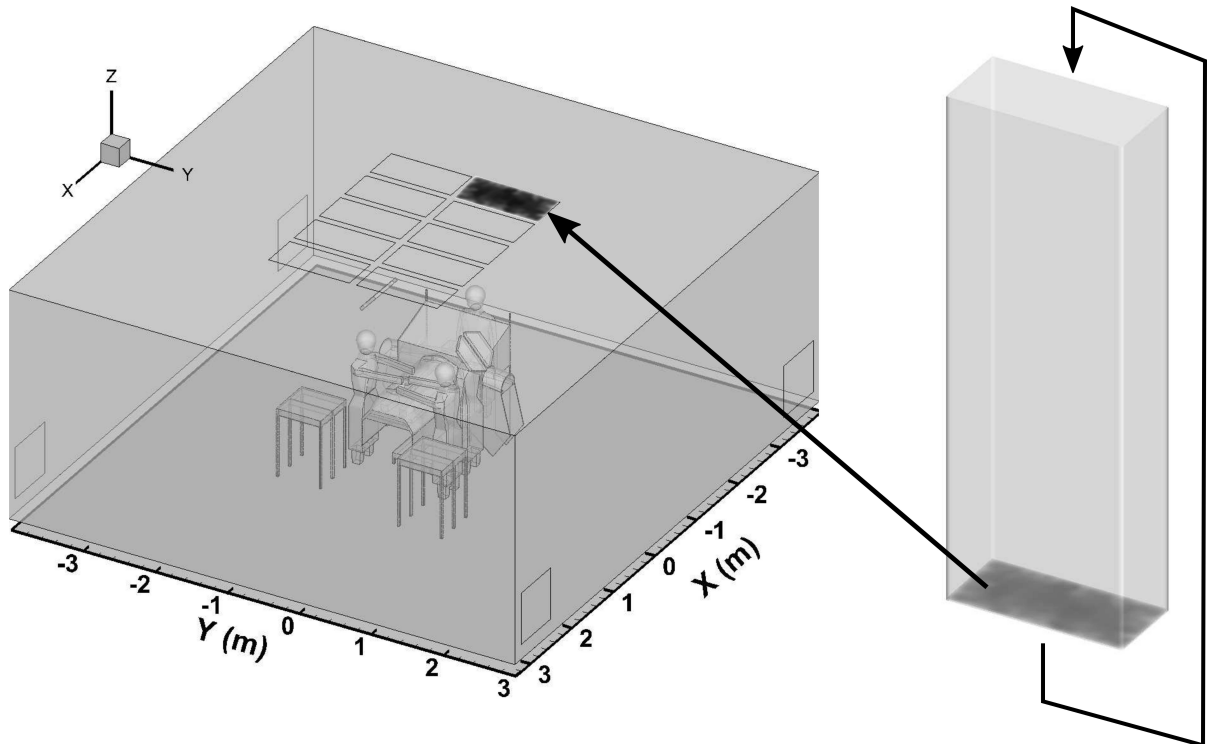


Figure 12: Schematic of the periodic duct used to generate inlet flow data.

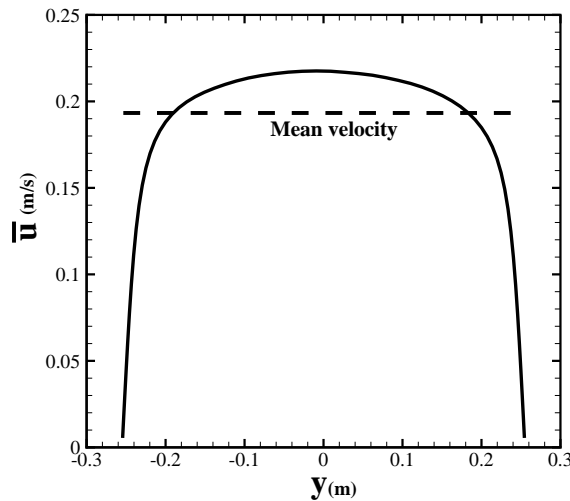


Figure 13: Mean velocity profile generated by a periodic duct flow for the inlet grilles.

let. Thus, a periodic turbulent duct flow was computed (figure 12) to produce a target mean flow rate equal to that prescribed ($\dot{V} = 1.10436\text{m}^3/\text{s}$) using a body force technique of [Pierce & Moin \(1998b\)](#). This also generates turbulence fluctuations at the inlet plane that satisfy the continuity equation. The cross-sectional area of the periodic duct used is the same as that of each grille ($1.12\text{m} \times 0.51\text{m}$), and the length is about 4.5 times the hydraulic diameter of the cross-section. The velocity field data at the inlet cross-section was recorded in time series for almost 400 seconds of physical time. Figure 13 shows the time-averaged velocity field in the center plane of the duct obtained from the periodic duct simulation. The turbulence intensity ($I = \sqrt{\frac{1}{3}(u_{rms}^2 + v_{rms}^2 + w_{rms}^2)}/\bar{U}_{in}$) at the inlet cross-section is 5-6% of the mean inlet velocity (\bar{U}_{in}), and is in agreement with the experimental measurements conducted by [McNeill et al. \(2012, 2013\)](#). Here, u_{rms} , v_{rms} and w_{rms} are the root-mean square velocity components in the x , y and z directions, respectively.

3.4.2 Hot air blower and other heat sources

A 3MTM Bair HuggerTM 750 blower draws air from the floor of the operating room, heats it and blows it into the blanket (3MTM Bair HuggerTM Model 522) that covers the torso region of the patient. The blanket is covered with a plastic drape. The maximum flow rate of the blower is $\dot{V}_{blower} = 0.021\text{m}^3/\text{s}$. The hot air moves along the surface of the drape that faces the patient and then it is discharged into the room along the drape edges. In the present calculation, the bottom surface (facing the floor) of the 3MTM Bair HuggerTM blower is considered as a suction surface with

surface area ($A_{extraction} = 0.03796\text{m}^2$). A Dirichlet boundary condition is applied at this surface that prescribes the extraction velocity $\bar{U}_{extraction}$ as

$$\bar{U}_{extraction} = \frac{\dot{V}_{blower}}{A_{extraction}}, \quad (19)$$

giving an extraction velocity of 0.5532m/s. To model the hot air discharged along the edges of the drape. The total area of this edge of the drape is measured to be $A_{drape} = 0.07794\text{m}^2$. A Dirichlet boundary condition is applied such that the air is injected into the room perpendicular to the edges of the drape with velocity, \bar{U}_{drape} , calculated as,

$$\bar{U}_{drape} = \frac{\dot{V}_{blower}}{A_{drape}}, \quad (20)$$

giving an average injection velocity along the drape edge as 0.2694 m/s. The temperature of the hot air at the BH blower outlet is prescribed equal to 109°F (42.77°C) and the temperature of the air leaving the drape edge is set equal to 106°F (41.11°C) according to 3M video at:

<https://www.youtube.com/watch?v=QhzeInWIJ54>. The flow rates at the inlet grilles and for the blower are summarized in Table 3.4.2.

Other heat sources in the surgical room are mainly the surgeons, patient, surgical lamps, and exposed surface of the patient's knee. These heat sources can cause warming of the air in contact with the surfaces and result in a rising thermal plume. For these surfaces, a Dirichlet condition was used for temperature based on the experimentally measured values. In their work, McNeill *et al.* (2012) conducted detailed measurements of detailed surface temperatures that may lead to buoyant plumes specifically to be used in CFD calculations. The values are summarized in Table 3.4.2, among which, the temperatures of surgeons and patient's heads as well as the surgical lamps are based on the work of McNeill *et al.* (2012) and the rest are from the 3M video. For all other other solid surfaces, a no heat flux Neumann condition was specified, $\frac{\partial T}{\partial n} = 0$.

3.5 Numerical solution method

The computational approach is based on a co-located, finite-volume, energy-conserving numerical scheme on unstructured grids (Moin & Apte, 2006; Mahesh *et al.*, 2006) and solves the variable

Table 2: Flow and temperature conditions

Parameter	Value
Inlet volume flow rate \dot{V} , [m ³ /s]	1.1044
Temperature of inlet grille air, [°C]	15
Mean inlet velocity [m/s], \bar{U}_{in}	0.1933
BH blower volume flow rate \dot{V}_{blower} , [m ³ /s]	0.021
Temperature of hot air leaving the drape edge, [°C]	41.11
Heads of the surgeons and patient, [°C]	31.44
The patient's knee, [°C]	37.78
Two surgical lamps, [°C]	93.92

density gas-phase flow equations in the limit of zero-Mach number. In this co-located scheme, the velocity and pressure fields are stored and solved at the centroids of the control volumes. Numerical solution of the governing equations of the continuum fluid phase and particle phase (squames) are staggered in time to maintain time-centered, second-order advection of the fluid equations. Denoting the time level by a superscript index, the velocities are located at time level t^n and t^{n+1} , and pressure, density, viscosity, and the scalar fields at time levels $t^{n+3/2}$ and $t^{n+1/2}$. Squames position and velocity are advanced explicitly from $t^{n+1/2}$ to $t^{n+3/2}$ using fluid quantities at time-centered position of t^{n+1} .

3.5.1 Advancing the Lagrangian squames equations

The squames (particles) equations are advanced using a fourth-order Runge-Kutta scheme. Owing to the disparities in the flow field time-scale (τ_f) and the squames relaxation time (τ_p) sub-cycling of the squames equations may become necessary. Accordingly, the time-step for squames equation advancement (Δt_p) is chosen as the minimum of τ_p and the time-step for the flow solver (Δt). For the present simulations, the squames relaxation time, τ_p , based on the drag force, was found to be always larger than the time-step, Δt , used for solving the fluid flow equations in LES. Thus, the temporal evolution of the squames was well resolved by the flow time step, and subcycling of the particle equations was not necessary.

After obtaining their new positions, the squames are relocated, and the squames that cross inter-processor boundaries are duly transferred. Boundary conditions for squames crossing boundaries are applied and the computation is further advanced. Solving these Lagrangian equations thus requires

addressing the following key issues: (i) efficient search for locations of squames on an unstructured grid, (ii) interpolation of gas-phase properties to the squames location for arbitrarily shaped control volumes, (iii) inter-processor transfer of the squames.

Locating the squames particles in a generalized-coordinate structured code is straightforward since the physical coordinates can be transformed into a uniform computational space. This is not the case for unstructured grids used in the present simulations (Apte *et al.*, 2003b,a, 2009). The approach used here, projects the squames location onto the faces of the control volume and compares these vectors with outward face-normals for all faces. If the particle lies within the cell, the projected vectors point the same way as the outward face-normals. This technique is found to be very accurate even for highly skewed elements. A search algorithm is then required to efficiently select the control volume to which the criterion should be applied. An efficient technique termed as ‘the known vicinity algorithm’ was used to identify the control volume number in which the particle lies. Given the previous particle location, the known-vicinity algorithm identifies neighboring grid cells by traversing the direction the particle has moved. In LES, the time steps used are typically small in order to resolve the temporal scales of the fluid motion. Knowing the initial and final location of the particle, this algorithm searches in the direction of the particle motion until it is relocated. The neighbor-to-neighbor search is extremely efficient if the particle is located within 5-10 attempts, which is usually the case for 98% of the squames in the present simulation. Once this cell is identified, the fluid parameters are interpolated to the particle location using a generalized, tri-linear interpolation scheme for arbitrary shaped elements. Introducing higher order accurate interpolation is straight forward; however, it was found that tri-linear interpolation is sufficient to represent the gas-phase velocity field at particle locations. In the present case, particles are distributed over several processors used in the computation, and the load-imbalance was not significant. Details of the algorithm can be found in Apte *et al.* (2003b, 2009). The overall increase in computational cost due to addition of about 3 million particles was about 25% per time-step.

3.5.2 Advancing the Eulerian fluid flow equations

The scalar field (enthalpy or non-dimensional temperature; equation 5) is advanced using the old time-level velocity field. A second-order WENO scheme is used for scalar advective terms and centered differencing for the diffusive terms. All terms, except the source terms due to buoyancy

effect, are treated implicitly using Crank-Nicholson for temporal discretization. Once the scalar field is computed, the density and temperature fields are obtained from constitutive relations (equation 7) and the ideal gas law (equation 2). The cell-centered velocities are advanced in a predictor step such that the kinetic energy is conserved. The predicted velocities are interpolated to the faces and then projected. Projection yields the pressure at the cell-centers, and its gradient is used to correct the cell and face-normal velocities. The steps involved in solving the projection-correction approach for velocity field are briefly described below, Details of this algorithm may be found in Moin & Apte (2006); Mahesh *et al.* (2006); Apte *et al.* (2008b).

- Advance the fluid momentum equations using the fractional step algorithm. The density field is available at intermediate time level is obtained from arithmetic average at the two time steps $t^{n+3/2}$ and $t^{n+1/2}$.

$$\frac{\rho u_i^* - \rho u_i^n}{\Delta t} + \frac{1}{2V_{cv}} \sum_{\text{faces of cv}} \left[u_{i,f}^n + u_{i,f}^* \right] g_N^{n+1/2} A_f = \quad (21)$$

$$\frac{1}{2V_{cv}} \sum_{\text{faces of cv}} \mu_f \left(\frac{\partial u_{i,f}^*}{\partial x_j} + \frac{\partial u_{i,f}^n}{\partial x_j} \right) A_f + (\rho - \rho_0) g_i$$

where f represents the face values, N the face-normal component, $g_N = \rho u_N$, and A_f is the face area. The superscript ‘*’ represents the predicted velocity field, and $g_N^{n+1/2} = 0.5(g_N^n + g_N^{n+1})$.

- Interpolate the velocity fields to the faces of the control volumes and solve the Poisson equation for pressure:

$$\nabla^2 (p \Delta t) = \frac{1}{V_{cv}} \sum_{\text{faces of cv}} \rho_f u_{i,f}^* A_f + \frac{\rho^{n+3/2} - \rho^{n+1/2}}{\Delta t} \quad (22)$$

- Reconstruct the pressure gradient, compute new face-based velocities, and update the cv-velocities using the least-squares interpolation used by Mahesh *et al.* (2004); Ham *et al.* (2003); Mahesh *et al.* (2006),

$$\frac{\rho (u_i^{n+1} - u_i^*)}{\Delta t} = -\frac{\delta p}{\delta x_i}. \quad (23)$$

4 Results

The numerical simulation was initiated with stagnant air (zero velocity) in the operating room and proper boundary conditions. A simulation was carried out with the blower off and all surfaces at room temperature for about 67s of physical time, which corresponds to about 4 flow through times based on the average inlet air velocity and the height of the room. After the initial transients, the thermal boundary conditions were applied at the surgeons heads, the patient's knee, the surgical lights. A calculation was performed for another 54s to establish a stationary flow with the thermal plumes created by the surfaces with higher-than-ambient temperatures. At this time, calculation of statistics for time-averaged mean velocity field and turbulence intensity were initiated and also 3 million squame particles were placed at the floor in three different regions surrounding the operating table as described below. With the blower-off the time-step used in the calculation was $\Delta t = 6 \times 10^{-5}$ s giving a CFL number of about 0.75. This time step was able to resolve the important time-scales of turbulence and particle motion accurately. The flow statistics were collected for a total of 80s after a stationary flow field was established and the squames trajectories were calculated for about 21s.

After the above calculation was completed, the remaining squames particles in the computational domain were removed, and the blower was turned on. With the blower discharging a hot air at higher speeds, the time-step was reduced by a factor of 2.5 to $\Delta t = 2.4 \times 10^{-5}$ s maintaining the CFL number about 0.6. The reduction in time step is related to both the explicit treatment of the gravitational source term in the momentum equation as well as increased velocity at the blower discharge location. A calculation was performed for about 30s to obtain a developed plume from the hot air discharged by the blower. Flow statistics and the initial location of 3 million squames particles were initiated. With the blower-on, the flow statistics were collected for about 37s and particle trajectories were calculated for about 30s.

All calculations were performed on a parallel computer and used 1600 processors. The computational domain was decomposed such that each processor contains roughly the same number of control volumes. The overall calculation (including initial transient, the case with blower-off and the case with blower-on including particle trajectories for both cases) took about 2M CPU-hrs. For the case of blower-off, about 20s of physical time would cost roughly 100,000 CPU-hours, whereas

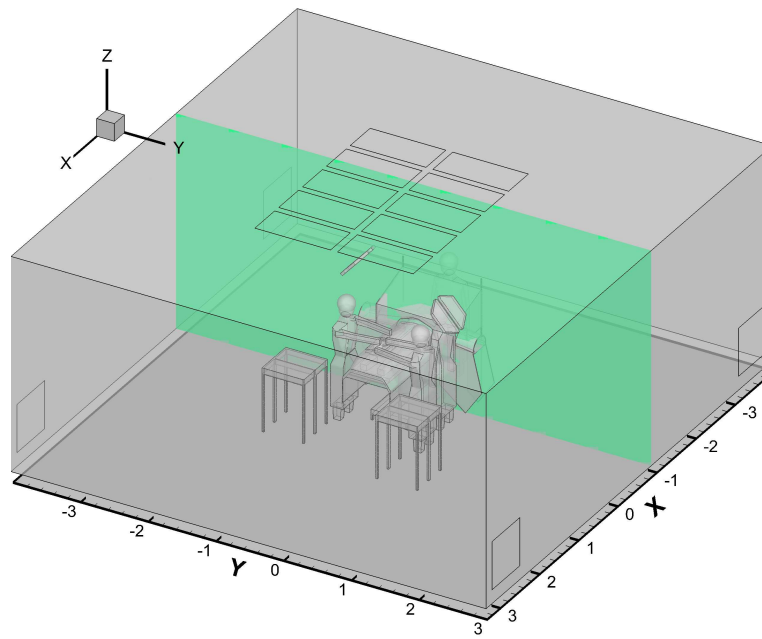
the same calculation with blower-on would cost roughly 220,000 CPU-hours. For each case, tracking 3 million trajectories of squames would add about 20-30% additional computing cost. This is because, initially the 3 million squames are clustered in a small region near the floor causing load imbalance as the particles were present on only a few processor domains. The flow statistics and particle trajectories are discussed below.

4.1 Flow characteristics

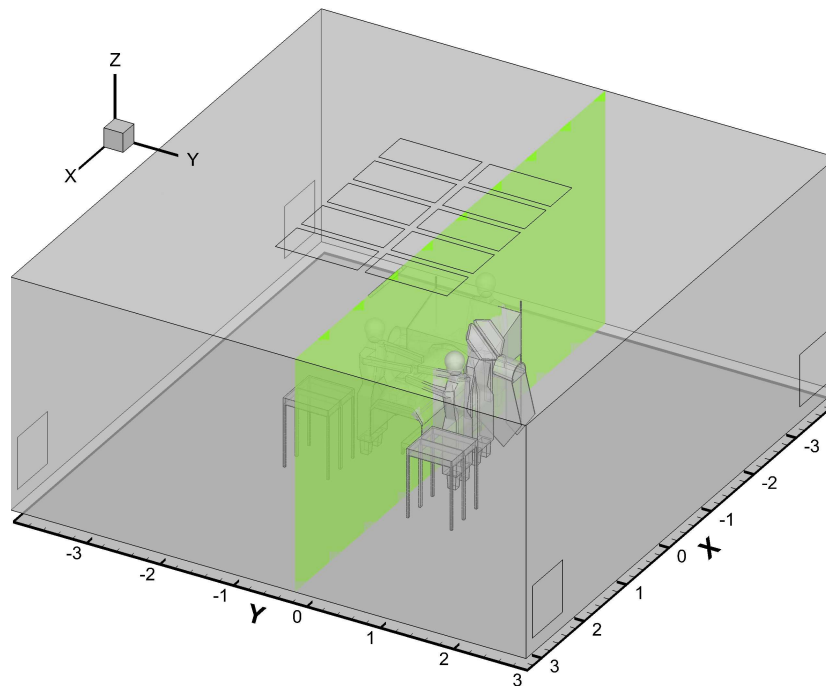
Figures 14a and 14b show the locations of two slices through the three-dimensional computational domain at $x = -0.88\text{m}$ and $y = -0.162\text{m}$ for which the mean velocity magnitude, turbulence intensity, and instantaneous temperature contours are plotted. The $x = -0.88\text{m}$ slice shows a planar cut that includes the surgical lamp and the operating table (OT). The $y = -0.162\text{m}$ slice shows a side view and contains 2 medical staff, a side table, the surgical lamp, and part of the inverted U-shaped drape. For these two slices, the flow characteristics with blower-off and blower-on are compared.

Figures 15, 16, and 17 show the contours of mean velocity magnitude, turbulence intensity, and instantaneous temperature, respectively, for the two cases of blower-off and blower-on. For the case of blower-off, figure 15a shows that the ventilation air from the ceiling inlet grilles moves downwards, gets deflected by the surgical lights and the table, impinges on the floor farther away from the table, and finally exits through the outlet grilles. Large recirculation regions are created on both sides of the table. The flow is not symmetric owing to asymmetries in the configuration itself. In comparison, with the blower turned on, the flow underneath and around the table is considerably modified as can be seen from the large velocity magnitudes under the table (figure 15b). The recirculation region is also disrupted by the rising air from the hot blower discharge. This difference is clearly visible from the turbulence intensity contours shown in figure 16a,b. With the blower-off, the maximum turbulence intensity level is about 30% in the high shear regions between the inlet air streams, as well as near the warm surgical lights due to the buoyant plume. With the blower-on, the turbulence intensity level is as high as 60% in regions affected by the rising thermal plumes from the blower hot air. The instantaneous temperature contours shown in figure 17a,b confirm that the increased turbulence level is mainly because of the thermal plumes from the hot blower air as can be seen by the high temperature regions under the OT.

Figures 18, 19, and 20 show the contours of mean velocity magnitude, turbulence intensity, and



(a)



(b)

Figure 14: Locations of the planes for which contour plots of mean velocity magnitude, turbulence intensity and instantaneous temperature are presented to compare the effect of the blower discharge on the flowfield: (a) $x = -0.88\text{m}$ (b) $y = -0.162\text{m}$.

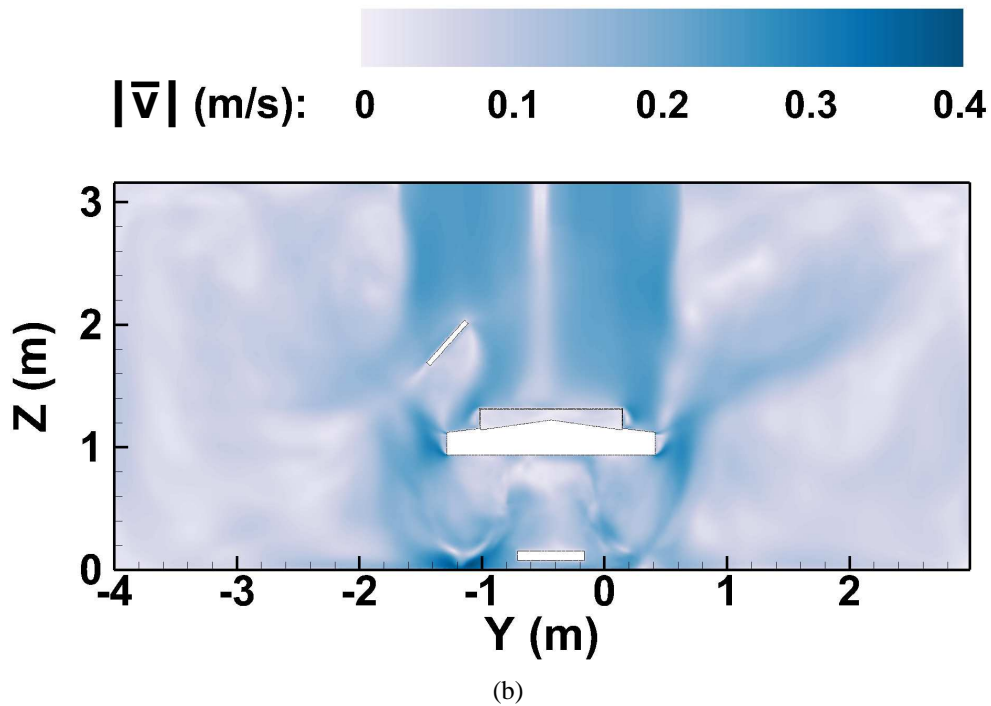
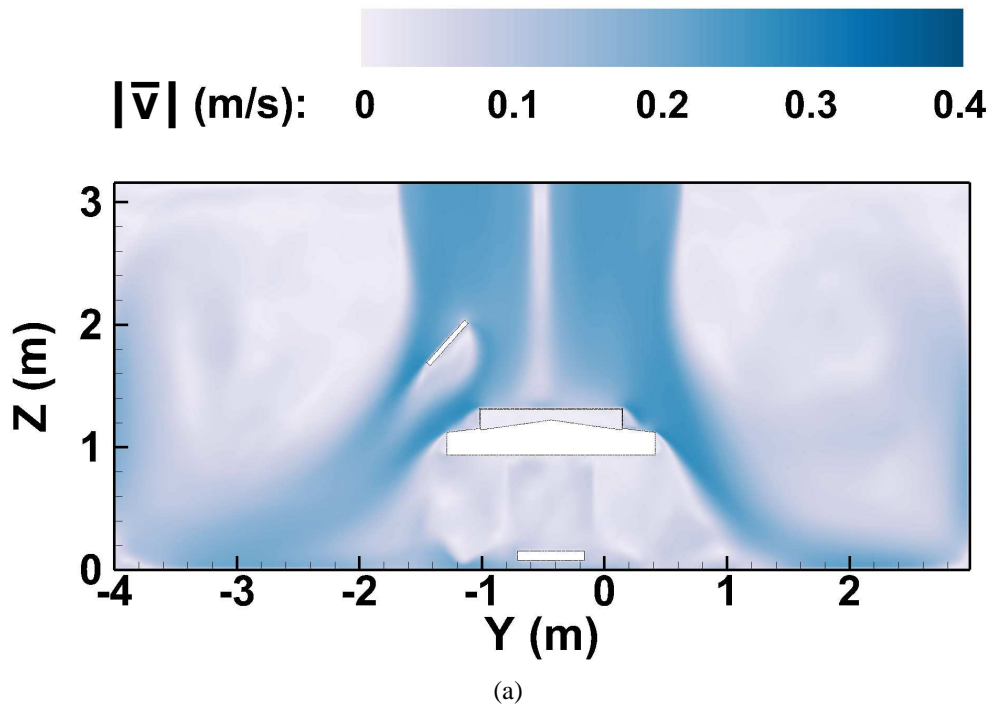


Figure 15: Contours of the mean velocity magnitude at $x = -0.88\text{m}$ (a) with blower-off and (b) with blower-on. The time average is taken over a physical time of 80s (no blower) and 37s (with blower) after establishing a stationary state.

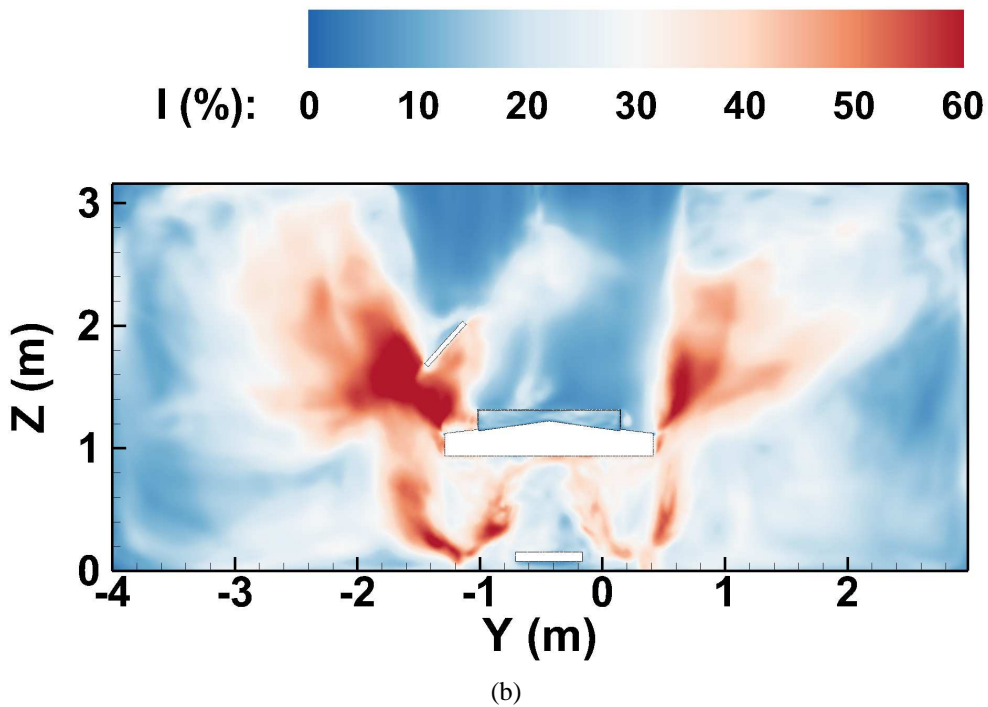
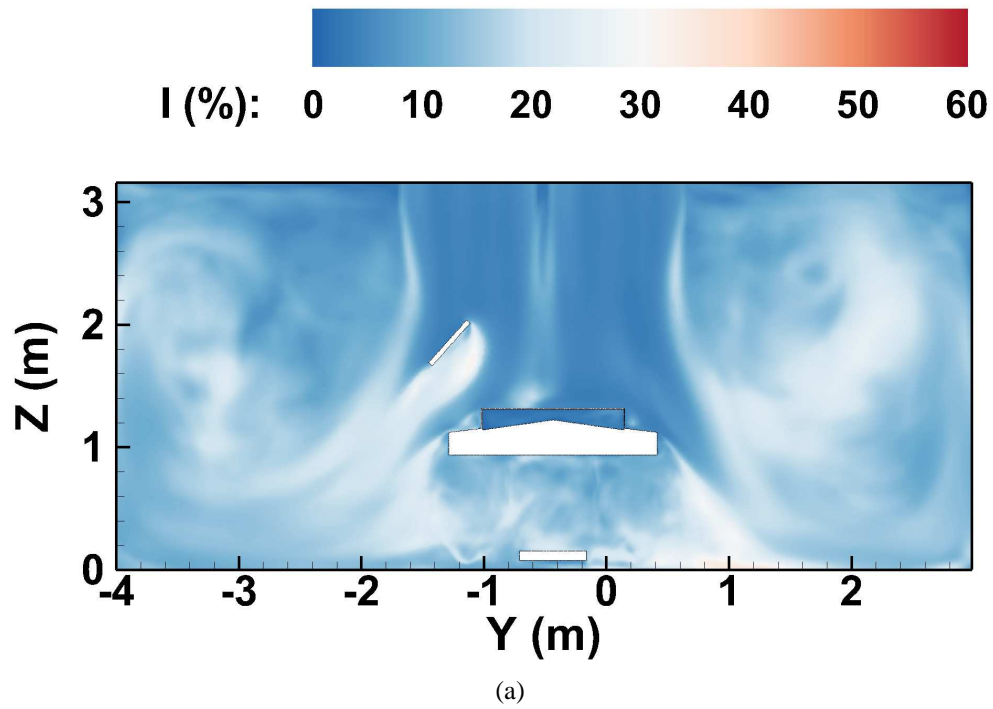


Figure 16: The turbulence intensity contours at $x = -0.88\text{m}$ (a) with blower-off and (b) with blower-on. The time average is taken over a physical time of 80s (no blower) and 37s (with blower) after establishing a stationary state.

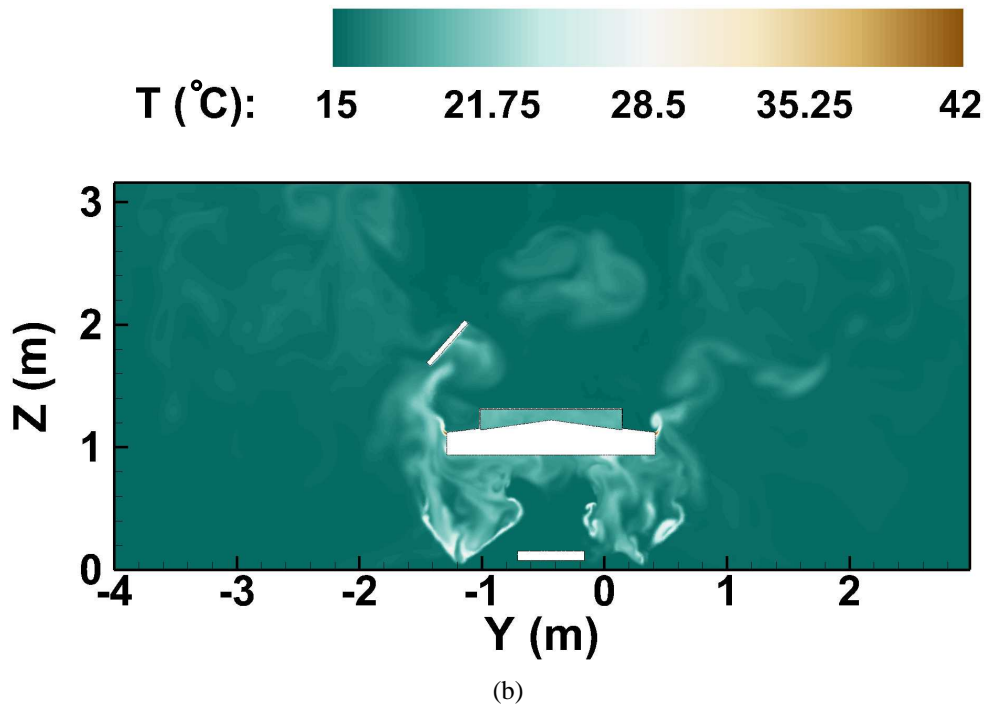
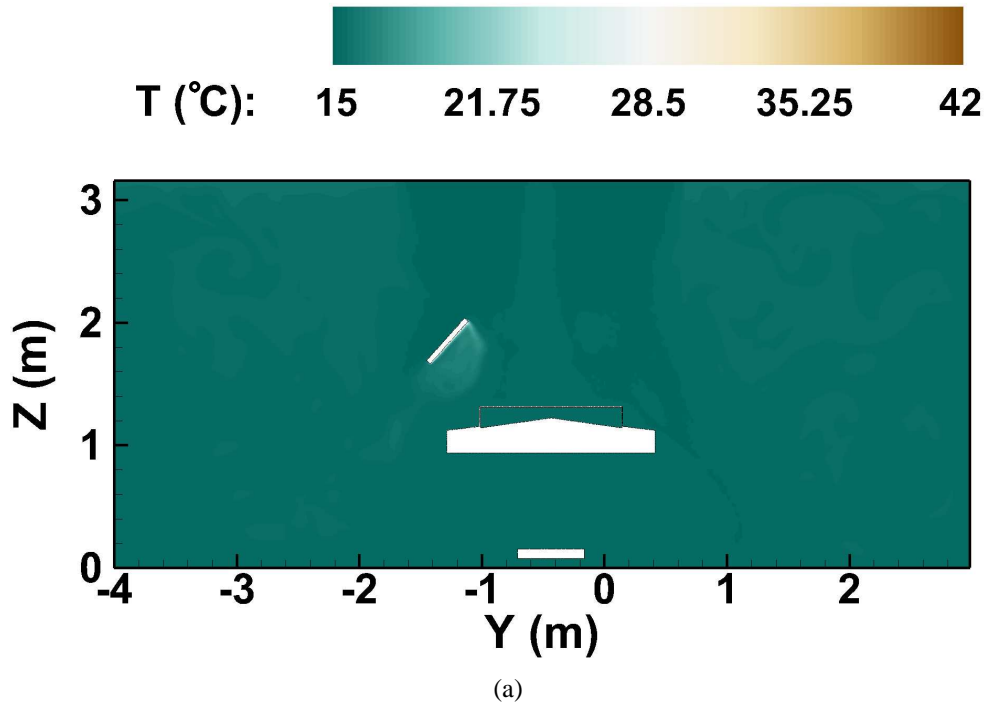


Figure 17: The instantaneous temperature contours at $x = -0.88\text{m}$ (a) with blower-off and (b) with blower-on. These snapshots are at about 35s after a stationary flow field was obtained and calculation for flow statistics was initiated.

instantaneous temperature, respectively, for the cases of blower-off and blower-on at $y = -0.162\text{m}$. Similar trends as described before are observed. The hot blower air and the rising thermal plumes disrupt the downward ventilation air flow. The high temperatures and turbulence intensity under the inverted U-shaped drape are clearly visible. The flow is also highly asymmetric with the blower turned on owing to the orientation and location of the drape. It is also seen from figure 20b that the rising thermal plumes may reach the ceiling in some regions. With the blower off, however, the plumes from warm surfaces of surgical lights, surgeons heads, and patient's knee are weak and are not significant enough to disrupt the downward ventilation air flow.

4.2 Dispersion of squames

This section provides details of the initial locations of the squames, their trajectories, and statistics of sampling the particles in regions of interest with high potential of reaching the surgical site.

4.2.1 Initial locations of squames

In order to provide a worst-case (or least probable) scenario for the squames to be carried to the surgical site by the air convection, all 3 million squames were initially placed on the floor and randomly distributed in a small region surrounding the operating table within a height of about 1 cm above the floor of the OR. If these squames are lifted by the turbulent air and moved to the surgical site, other effects such as motion of medical equipment and staff, additional squames shed from the heads and faces of medical staff, surgical garments, etc. will have an even higher probability to reach the surgical site.

Table 3: Coordinates of color-coded regions for initial positions of squames as shown in figure 21.

Color-coded initial position	$(x, y, z)_{\min}$ [m]	$(x, y, z)_{\max}$ [m]
Red	(-1.40, -0.025, 0.0)	(0.70, 0.40, 0.01)
Green	(-1.80, -1.35, 0.0)	(-1.4, 0.4, 0.01)
Yellow	(-1.40, -1.35, 0.0)	(0.70, -0.855, 0.01)

Three million particles with a diameter of 10 micron are placed within a 1 cm thick layer above the floor of the OR. The region where the particles are located is around the OT, surrounding the feet of four surgeons present in the CAD model. To better visualize the trajectories the squames

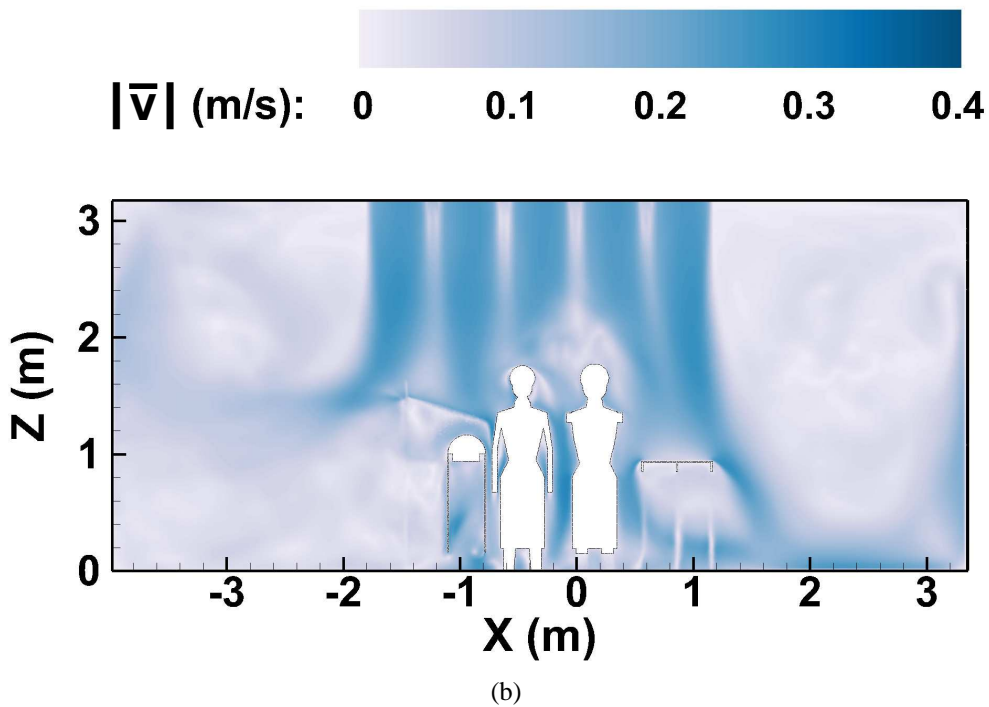
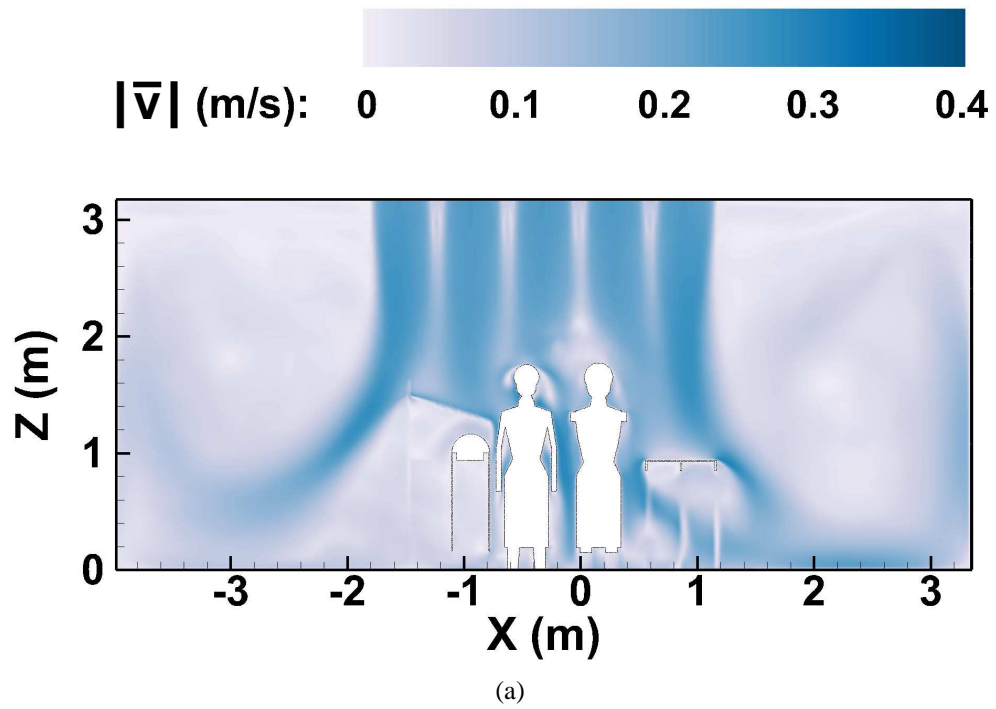


Figure 18: Contours of the mean velocity magnitude at $y = -0.162\text{m}$ (a) with blower-off and (b) with blower-on. The time average is taken over a physical time of 80s (no blower) and 37s (with blower) after establishing a stationary state.

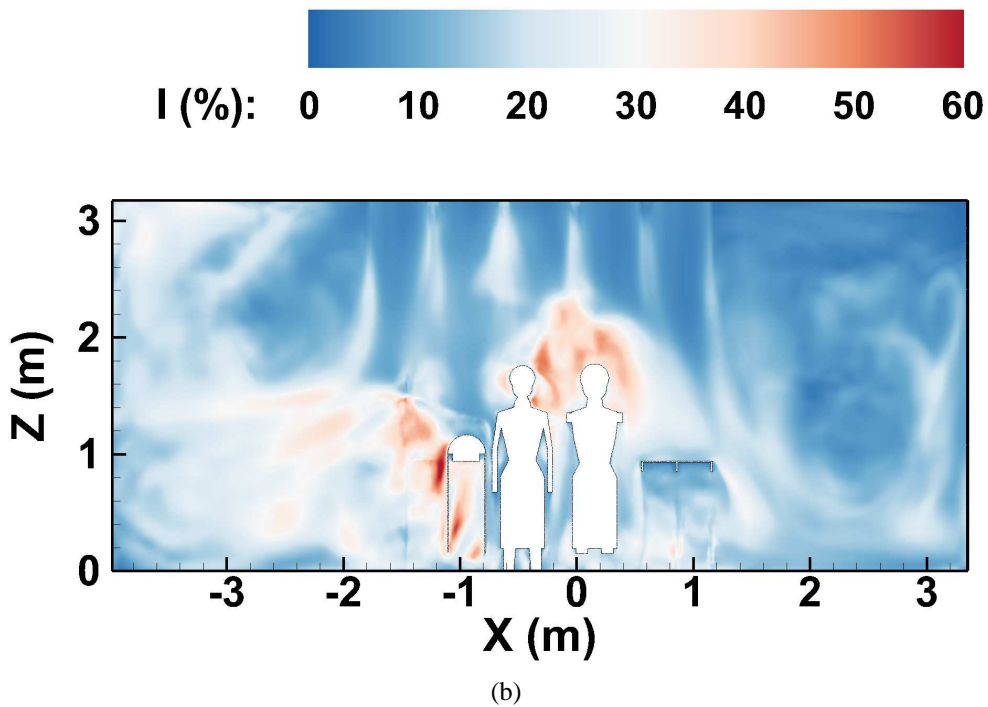
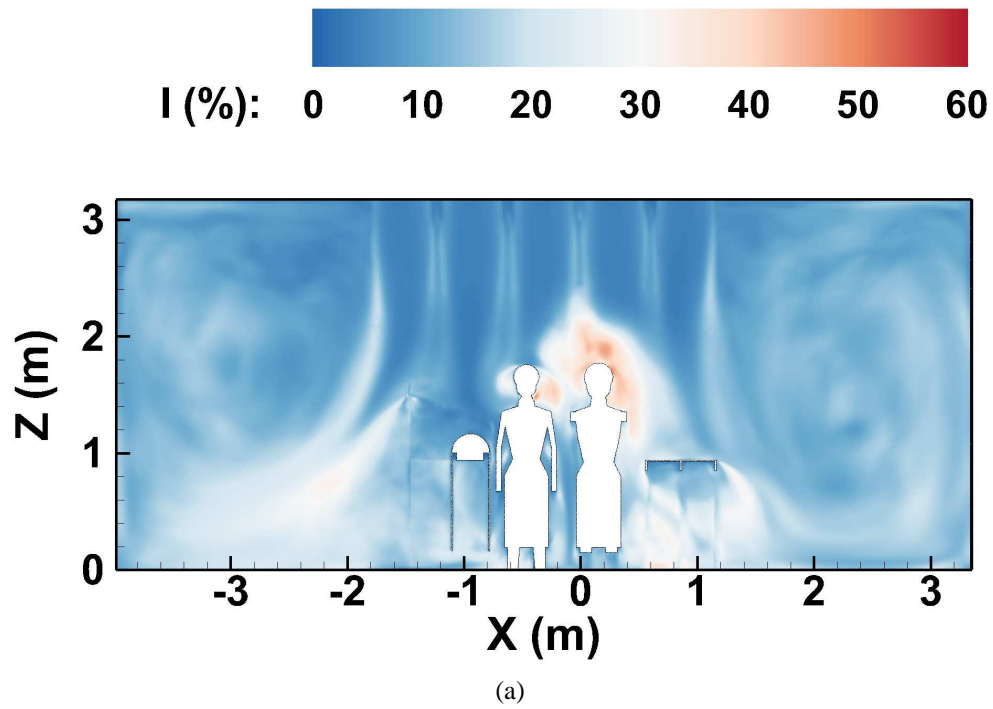


Figure 19: The turbulence intensity contours at $y = -0.162\text{m}$ (a) with blower-off and (b) with blower-on. The time average is taken over a physical time of 80s (no blower) and 37s (with blower) after establishing a stationary state.

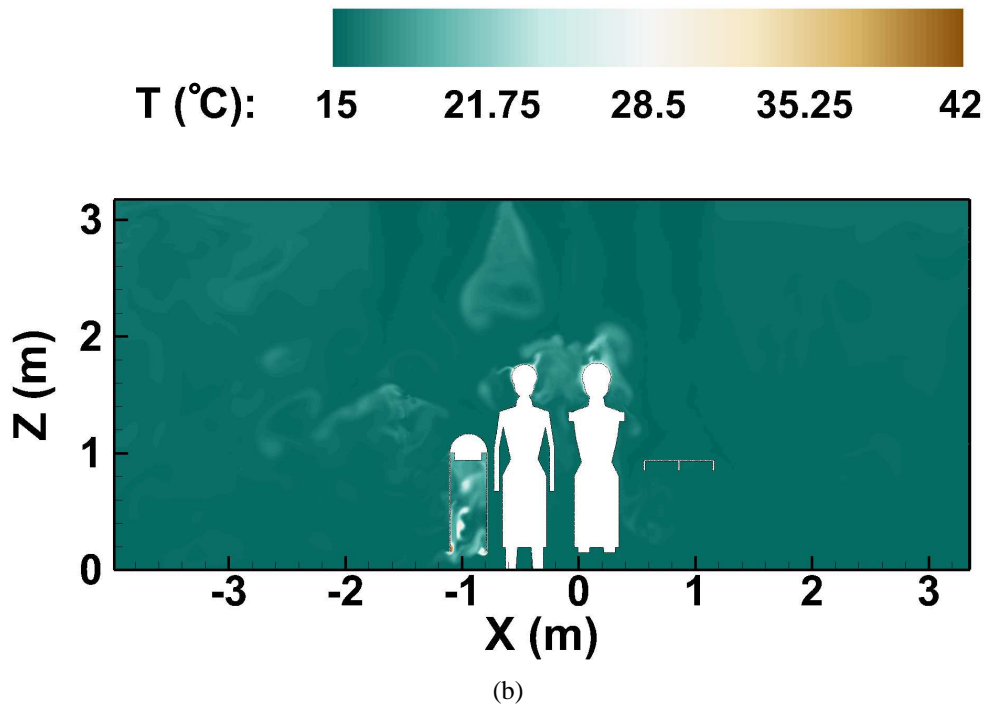
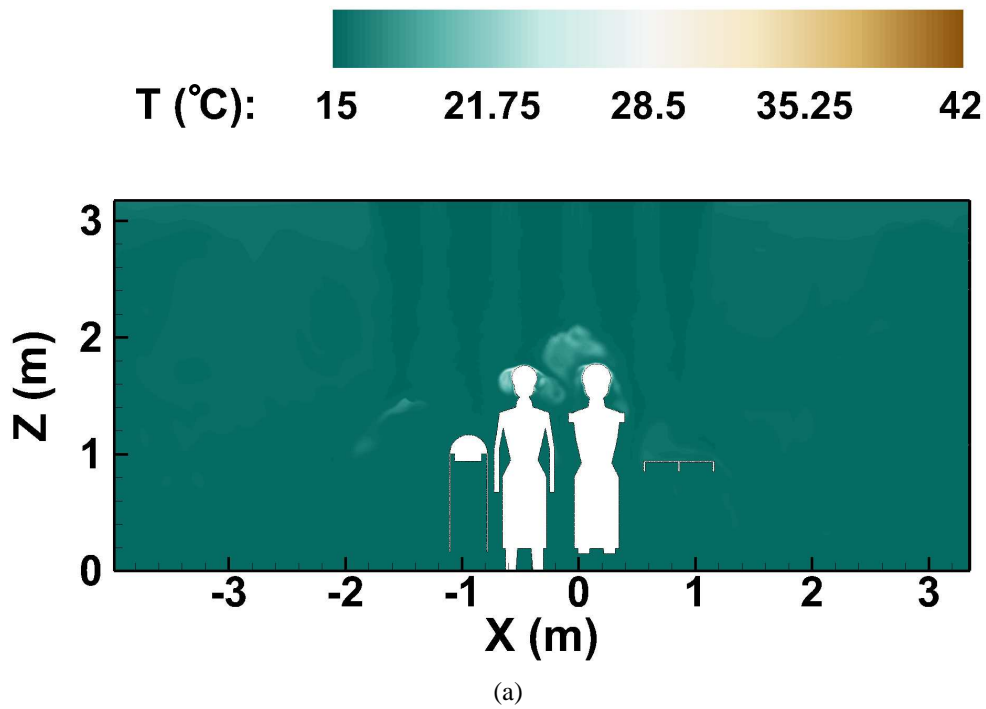


Figure 20: The instantaneous temperature contours at $y = -0.162\text{m}$ (a) with blower-off and (b) with blower-on. These snapshots are at about 35s after a stationary flow field was obtained and calculation for flow statistics was initiated.

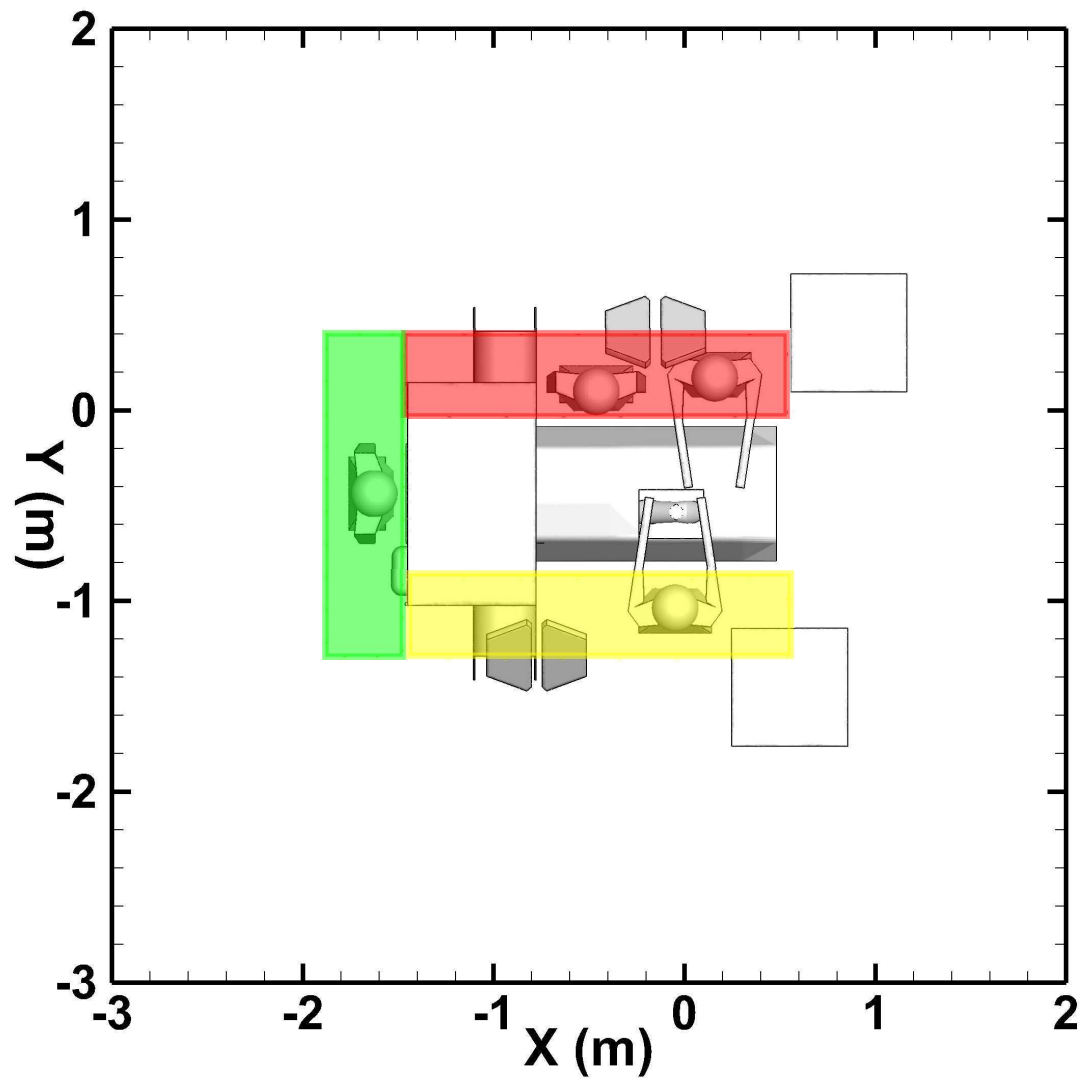


Figure 21: Three color-coded regions where the 3 million squames were initially distributed within a 1 cm height from the floor.

from different initial locations, the U-shaped region is divided into three rectangular sections color-coded as (i) red, (ii) green and (iii) yellow as shown in figure 21. One million squames are placed in each of the three sections at the same time, providing equal probability for the statistical analysis of motion of squames. The position of an individual squame particle in a section is chosen randomly using a uniform distribution. The squames of each section are tagged with distinct IDs. The actual coordinates of the three sections are given in Table 3.

4.2.2 Trajectories and snapshots of squames

In order to visualize the effect of the hot blower air on the trajectory of squames, instantaneous scatter plots of squames are displayed at 10s and 20s after their initiation with blower-off and blower-on in figures 22a,b and 23a,b, respectively. The squames are also color-coded based on their region of origin as highlighted in figure 21. Drastic differences between the blower-off and blower-on cases are observed. It is clear from figures 23a that the majority of the squames are dispersed by the ventilation air flow towards the outlet grilles when the blower is off. None of the squames actually rise to the level of the side tables or the OT. In contrast, in the case of blower-on, a large number of squames are lifted upwards by the rising thermal plumes. Some of the squames (mostly red-colored and some yellow-colored) are lifted above the surgeons heads and are blown towards the OT by the incoming ventilation air. Large number of squames are seen to be above the OT, several are surrounding the surgeons hands, above the side tables, and some are very close to the patient's knee and the surgical site. This is better visualized by the zoom-in view shown in figures 24a,b.

Figures 25, 26, and 27 show a different view angle for the squames at the same time instances as in the above discussion. It is again seen that with the blower-on several particles are lifted upwards by the thermal plumes and rise above the operating table and then are blown downwards by the incoming ventilation air.

Finally, figure 28 shows an instantaneous snapshot of squames very close to the patient's knee. It seen that several of the red-coded particles are near the bottom of the knee, whereas some yellow-coded particles are in the very close vicinity of the surgical site. Several particles are still suspended above the OT and are being transported downwards by the ventilation air and may potentially reach close to the surgical site.

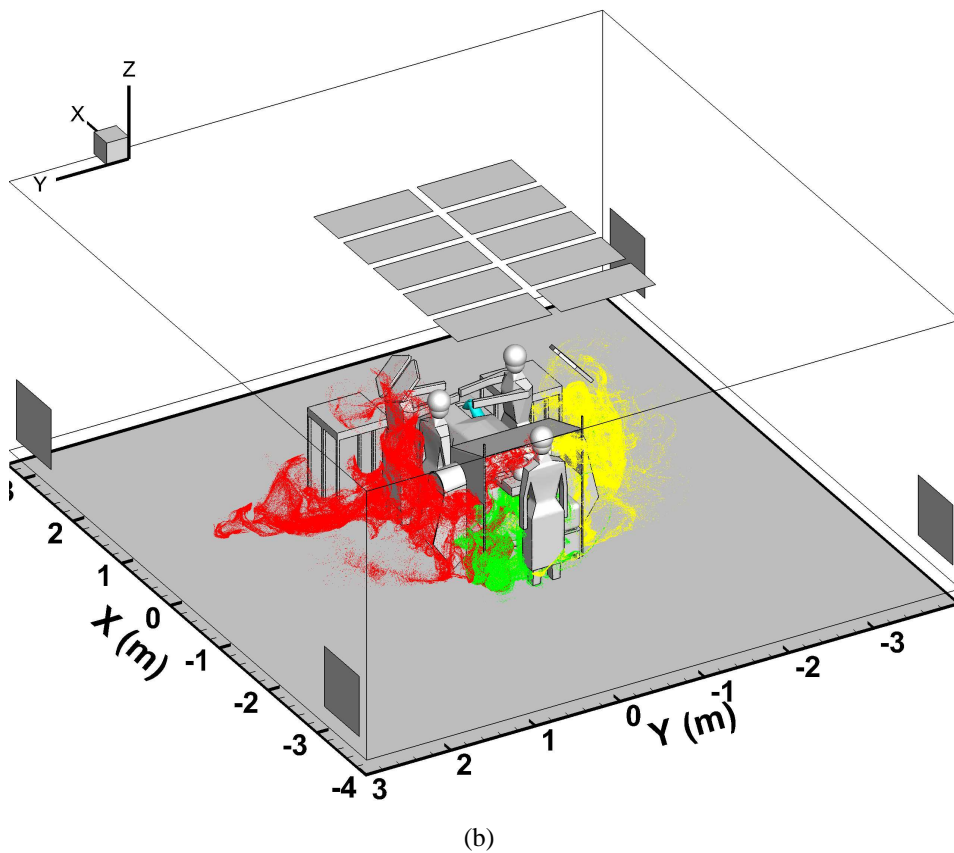
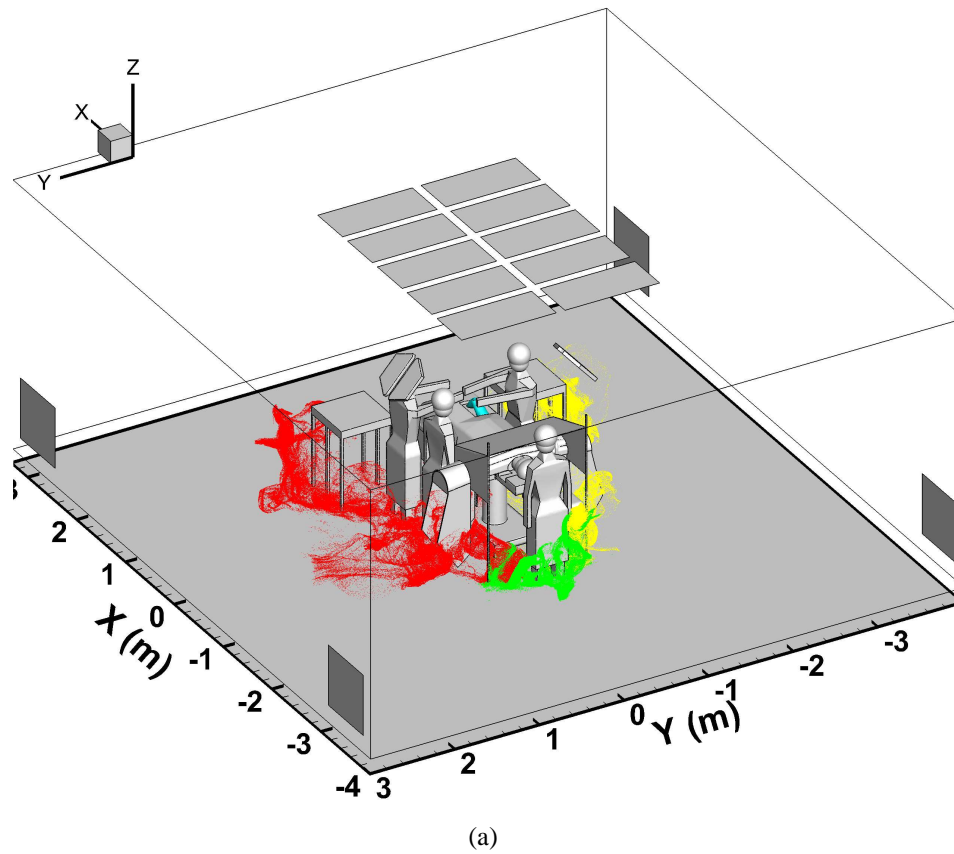


Figure 22: Instantaneous scatter plot of squames color-coded by their region of origin at 10s after initiation: (a) blower-off, (b) blower-on.

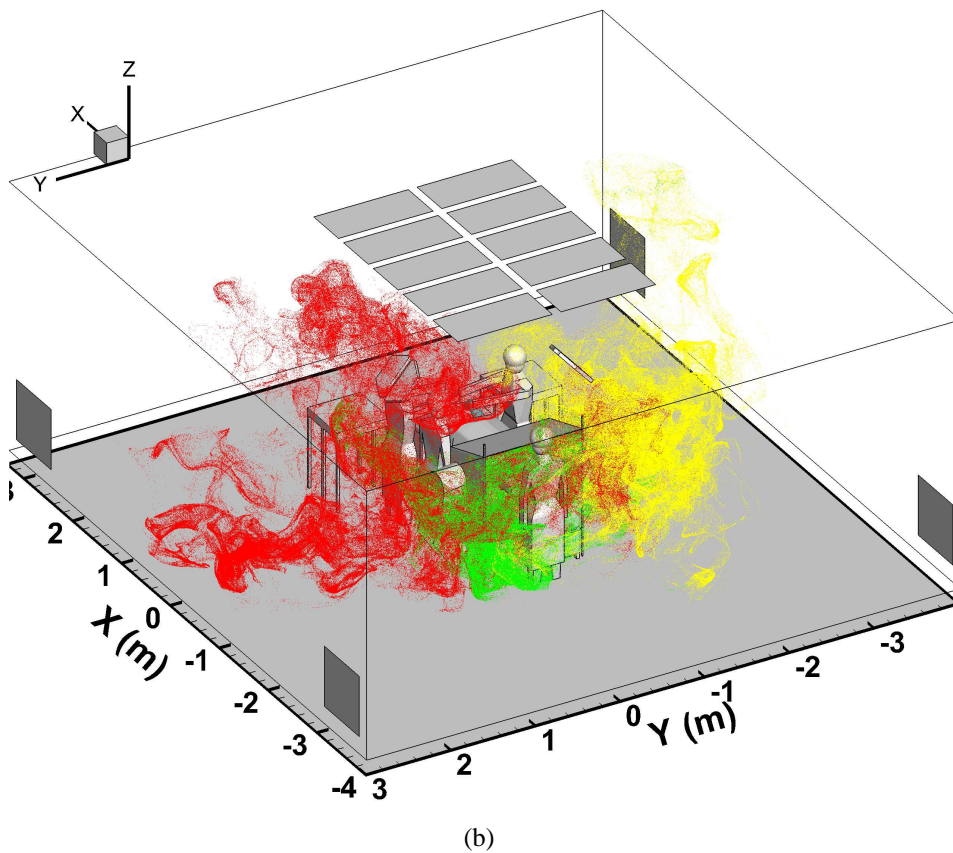
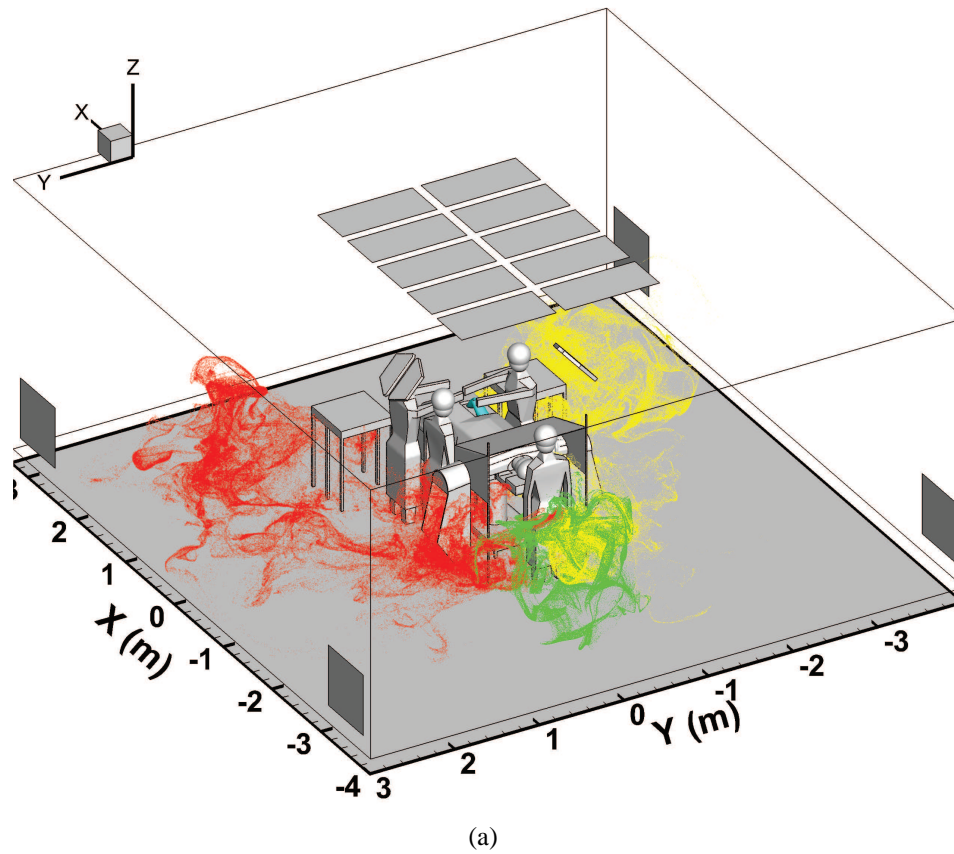
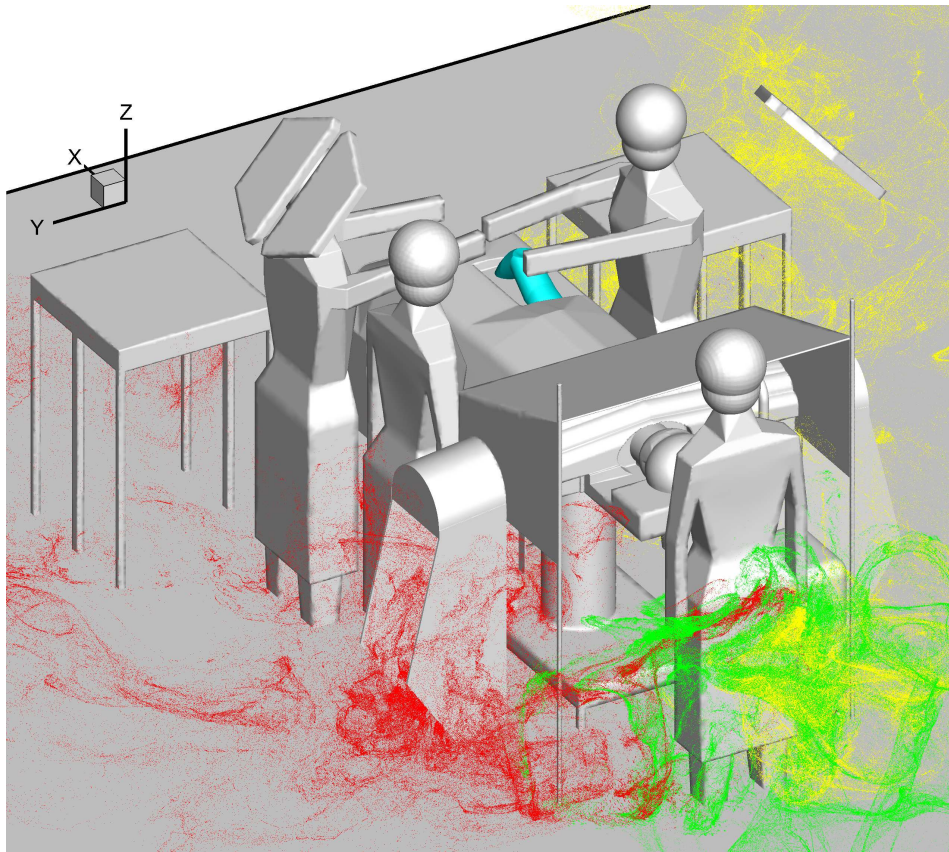
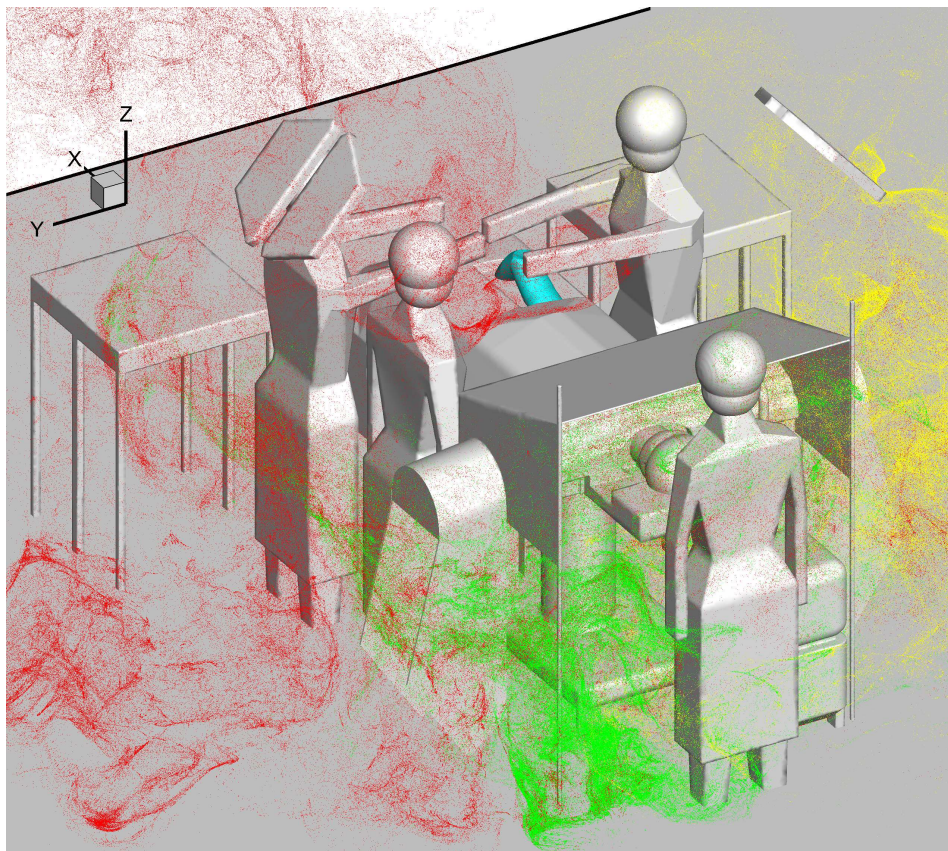


Figure 23: Instantaneous scatter plot of squames color-coded by their region of origin at 20s after initiation: (a) blower-off, (b) blower-on.



(a)



(b)

Figure 24: Zoom-in of the instantaneous scatter plot of squames color-coded by their region of origin at 20s after initiation: (a) blower-off, (b) blower-on.

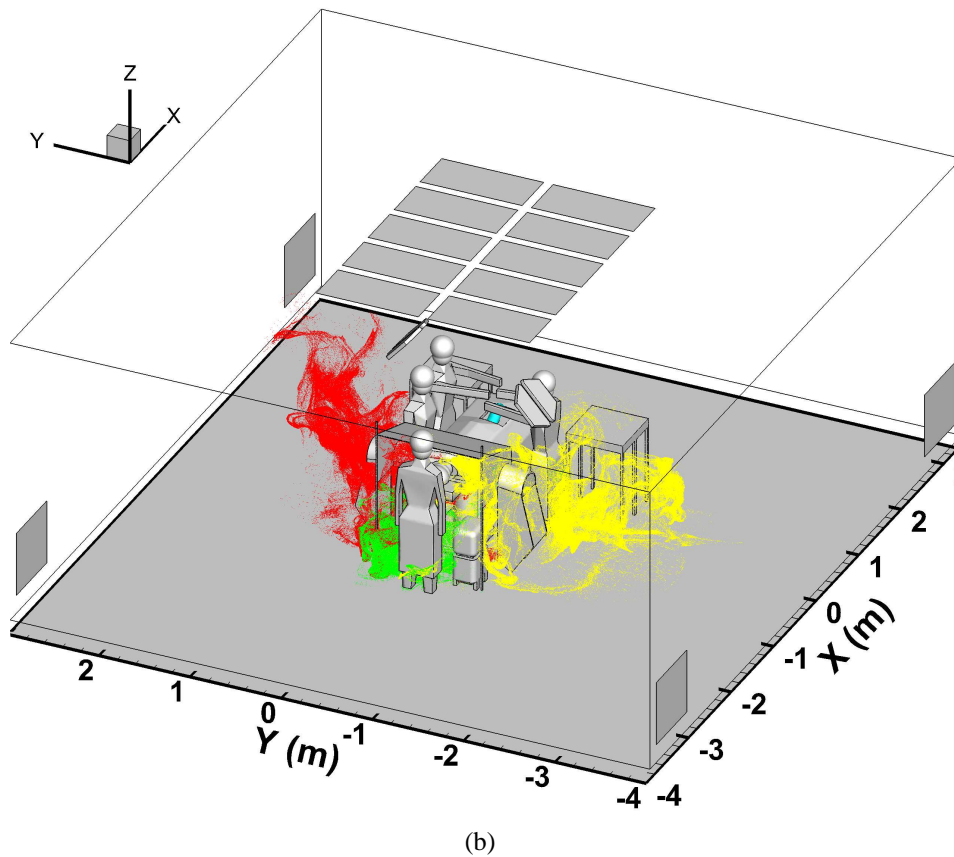
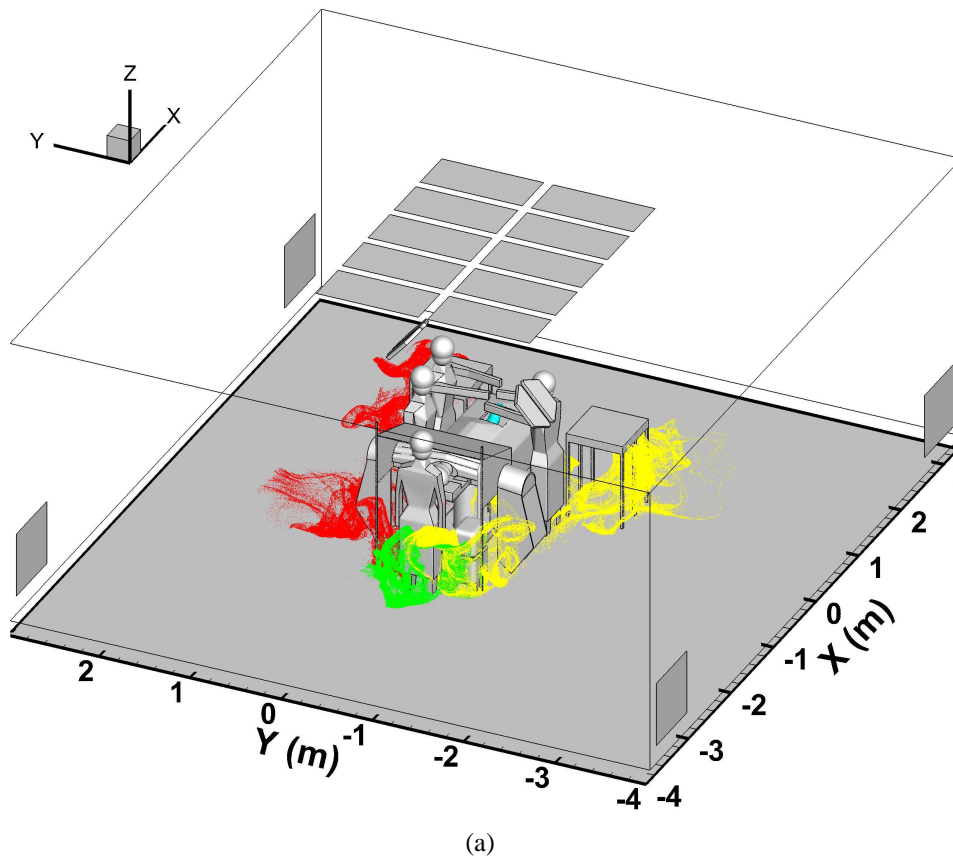


Figure 25: Instantaneous scatter plot of squames color-coded by their region of origin at 10s after initiation: (a) blower-off, (b) blower-on.

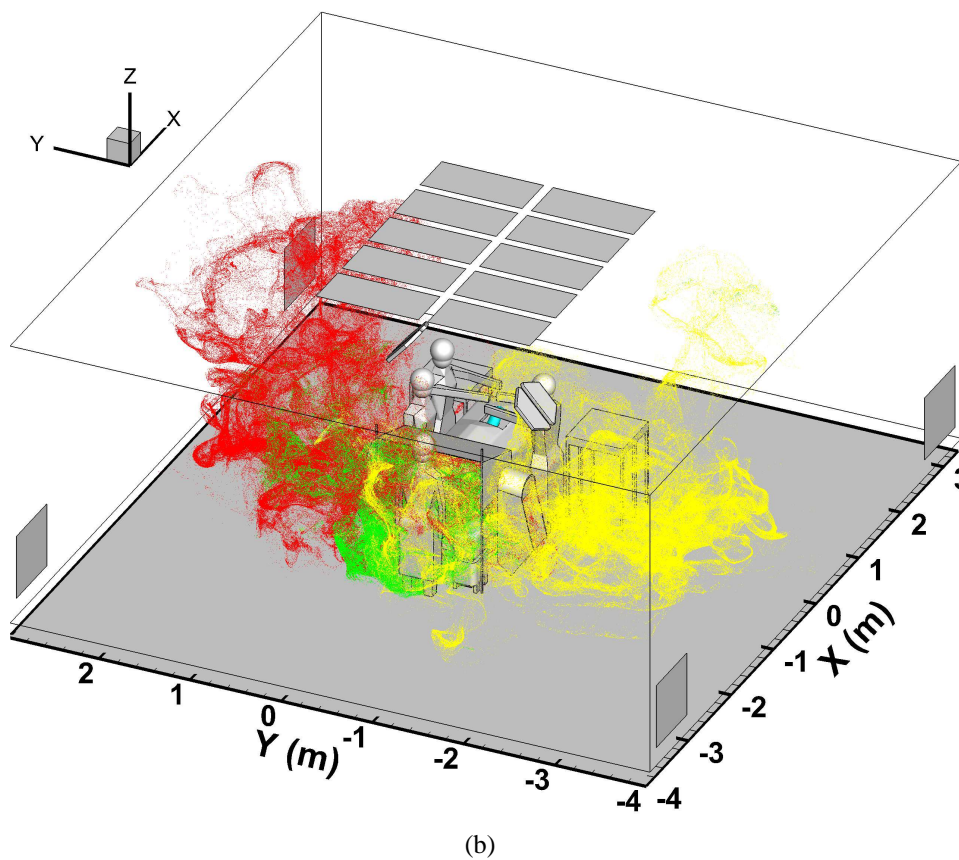
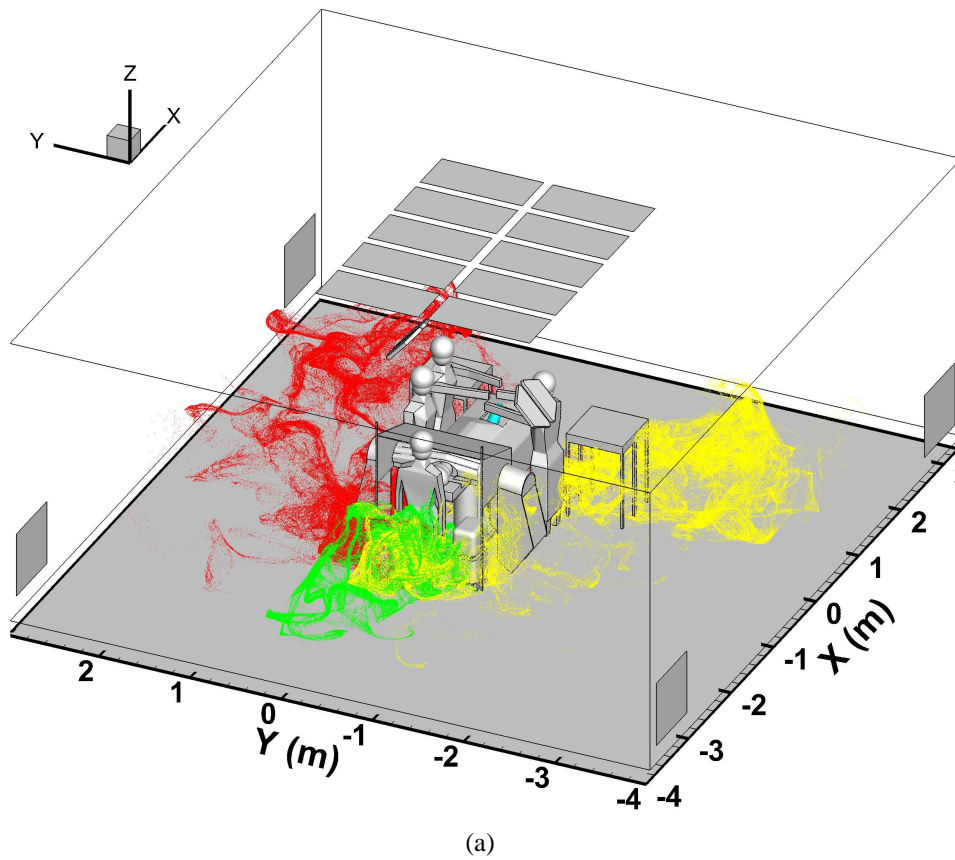
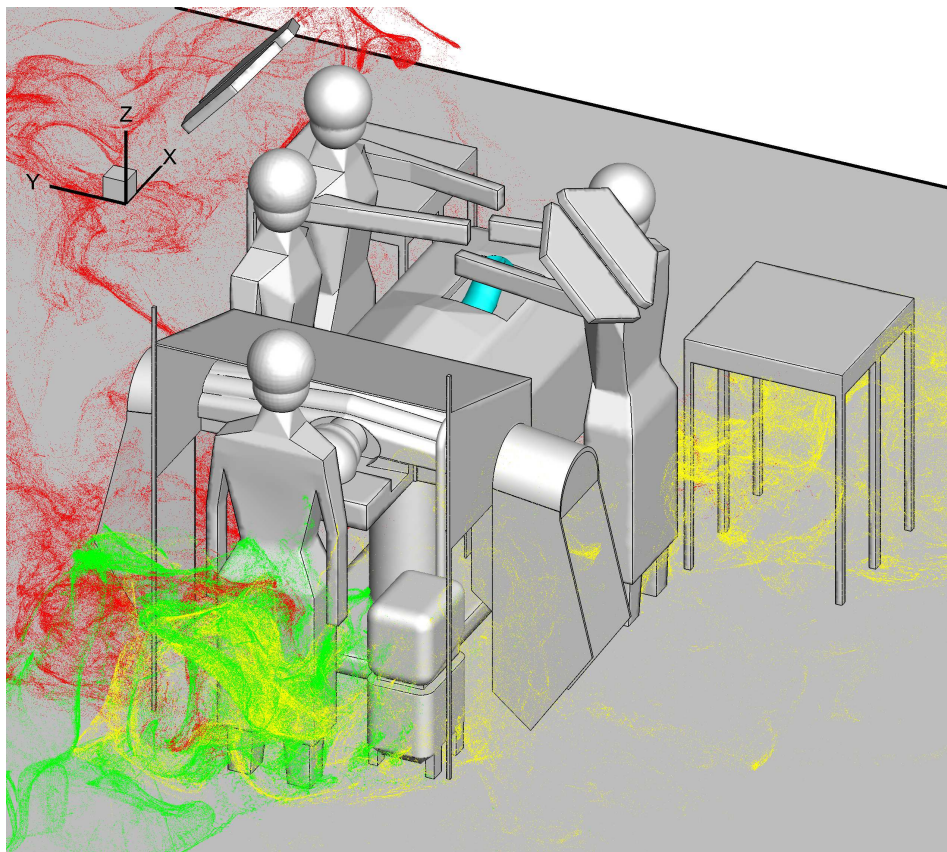
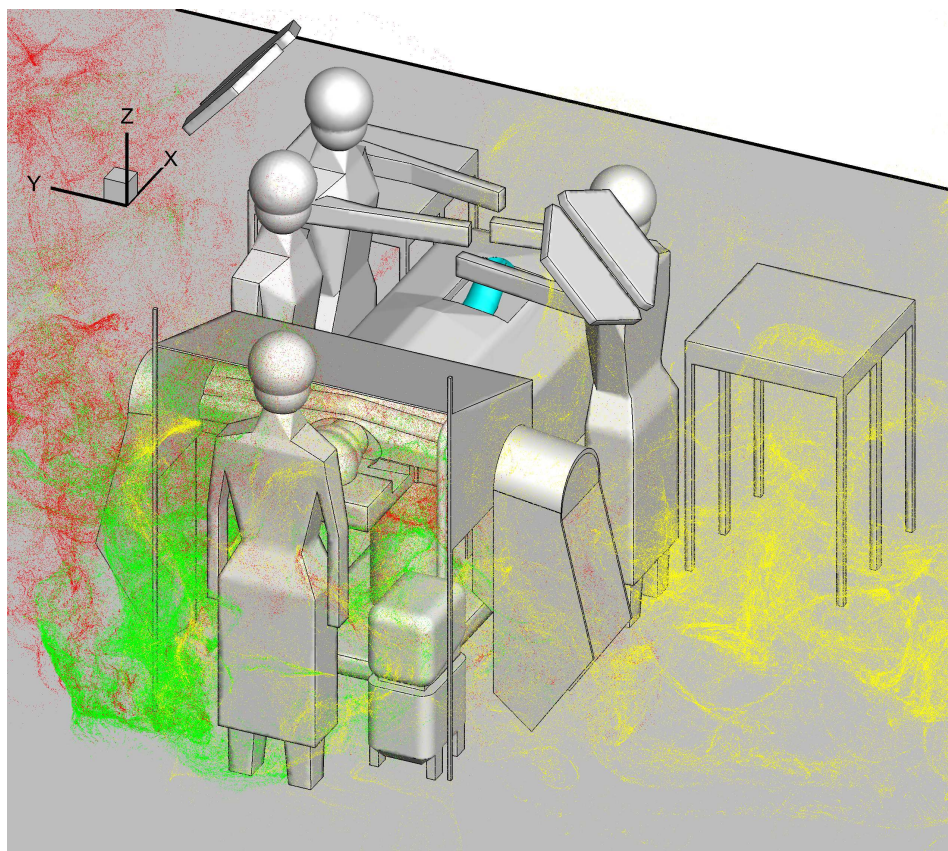


Figure 26: Instantaneous scatter plot of squames color-coded by their region of origin at 20s after initiation: (a) blower-off, (b) blower-on.



(a)



(b)

Figure 27: Zoom-in of the instantaneous scatter plot of squames color-coded by their region of origin at 20s after initiation: (a) blower-off, (b) blower-on.

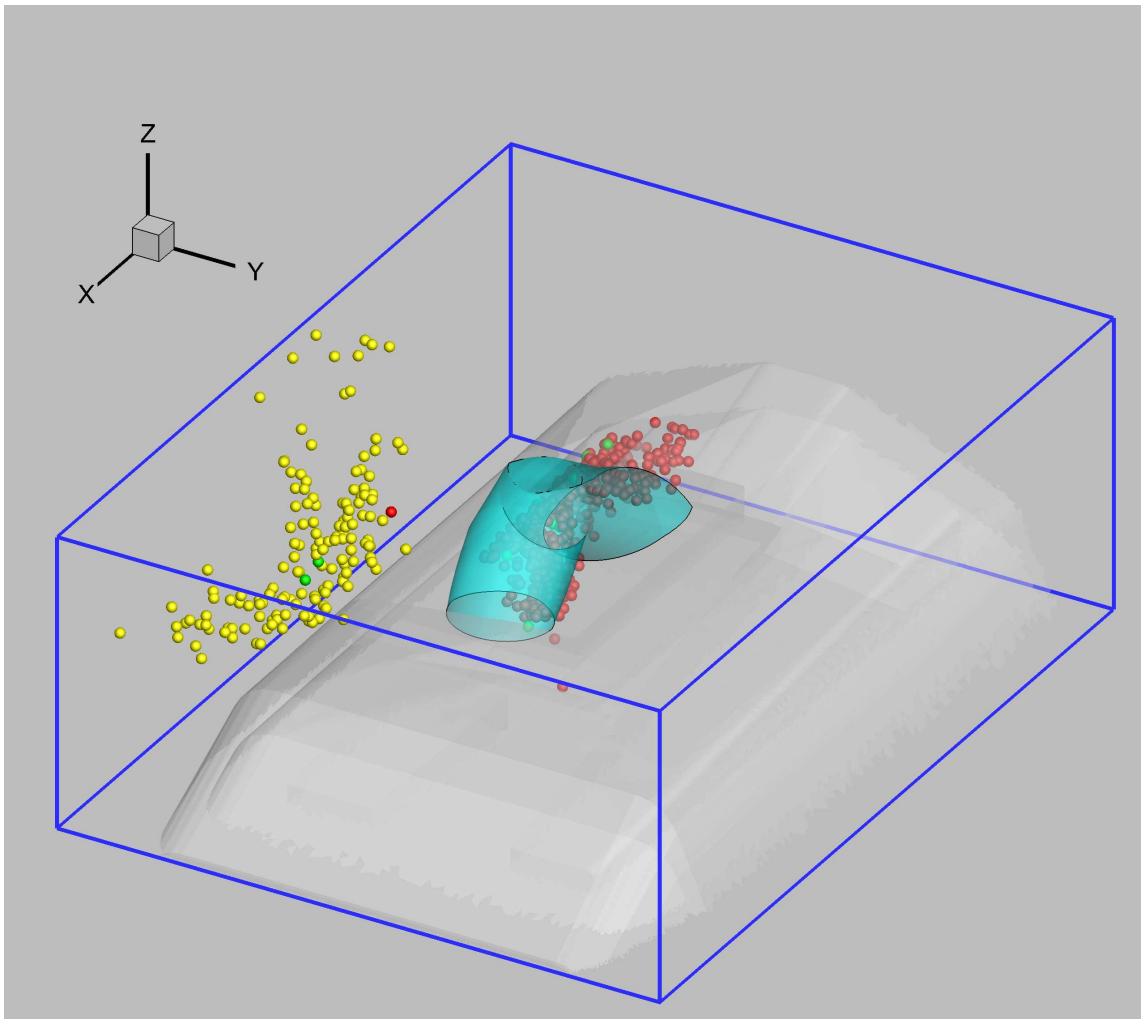


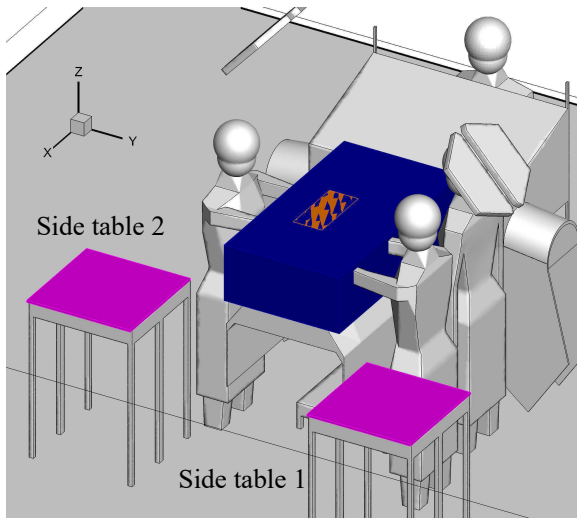
Figure 28: Zoom-in showing the instantaneous snapshot of squames near the surgical site at $t = 27$ s.

4.2.3 Number density of squames in the regions of interest

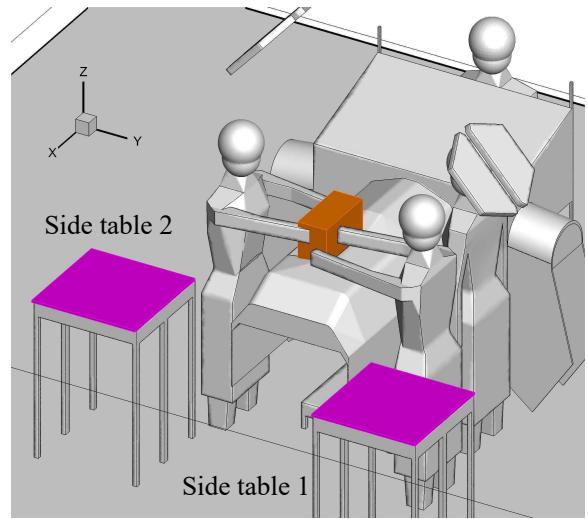
To assess the probability of squames reaching the surgical site, four imaginary boxes were located as follows: two boxes covering the two side tables, a box around the OT, and a box around the patient's knee area. The surgeons and medical assistants are bound to use surgical instruments placed on the side tables. The possibility of squames reaching the surgical site is then dependent on the number density of squames within these four imaginary boxes (see figure 29). The number of squame particles inside the four boxes are recorded in time. A blue box (figure 29 (a) and (c)) is covering the whole OT. The top of this box is about 30 cm high, including the patient's whole body and the surgeons hands. An orange box (figure 29 (b) and (d)) is placed above the OT, just covering the patient's knee and part of the surgeon's hands; and the top of the box is only 2 cm above the surgeon's hands. One purple box (figure 29 (a) - (d)) is placed on each of the two side tables. The height of these boxes is about 1 cm, so that any surgical instrument placed on the side tables would be within the box.

Two computations of the trajectories of squames were performed after a statistically stationary flow field has been reached for the cases of blower-off and blower-on. Based on the average inlet air velocity and the height of the room, it takes 15 – 20s for a fluid particle to travel from the ceiling grille to the floor. First, the blower is turned off and only the ventilation air from the inlet grilles and thermal plumes created by the warm surfaces including surgical lights, surgeons' heads, patient's head, and patient's knee are responsible for the dispersion of squames. It was found that all the squames initiated in all three sections (red, green and yellow) are basically transported by the air flow reaching the floor and quickly dispersed to the for outlet grilles. After a calculation of about 25s of physical time, some squame particles do rise to the underside of the side tables, but none of the squames was found to enter the four imaginary boxes representing the regions of interest. It was concluded that without the hot air discharged from the blower, the ventilation air circulation alone cannot disperse the squames to the surgical site. The thermal plumes from various warm surfaces only slightly affect the air coming from the inlet grilles and do not affect the motion of the squames.

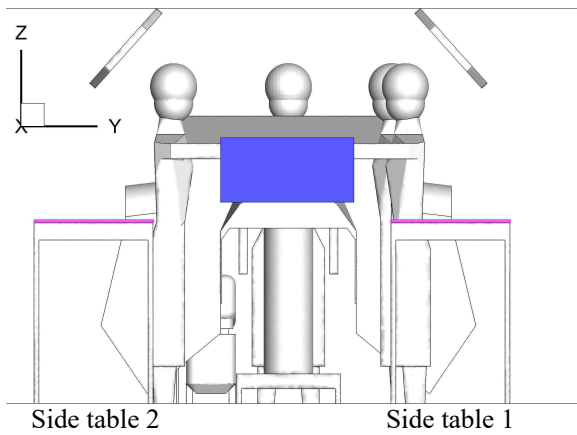
With the blower turned on, computations were carried out for about 30s of physical time to obtain a flow field with well established thermal plumes created by the hot air discharged from the blower. After reaching a stationary state, the squames were initiated in the same color-coded sections and the



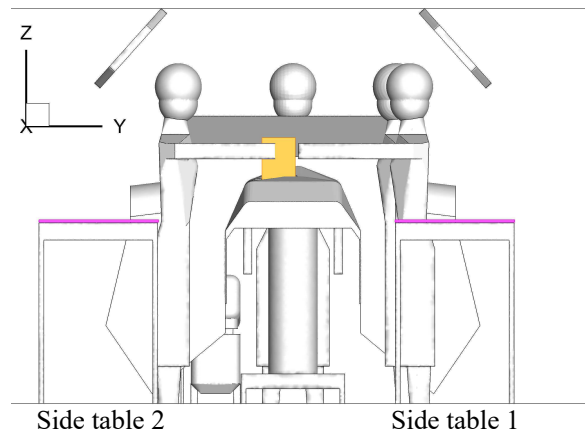
(a)



(b)



(c)

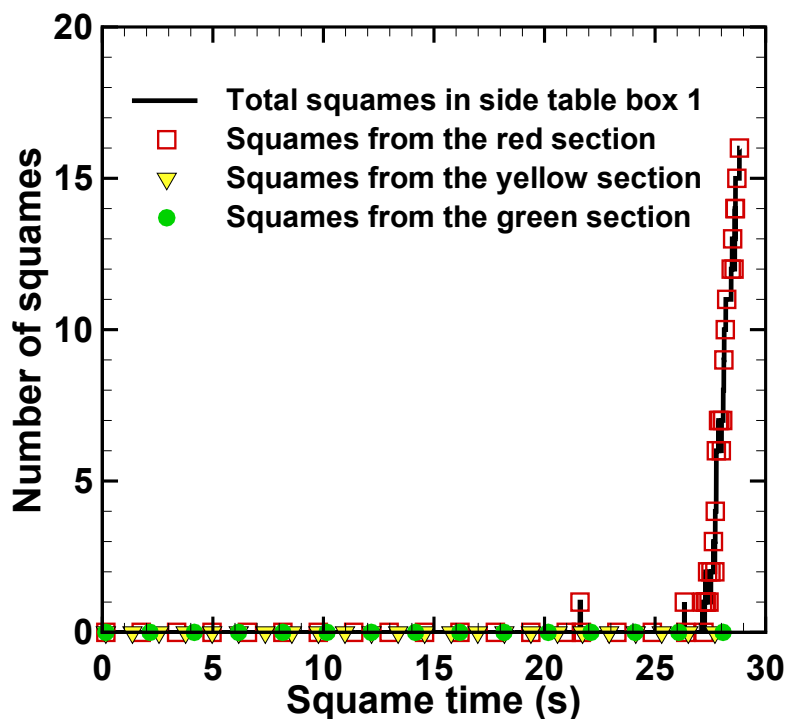


(d)

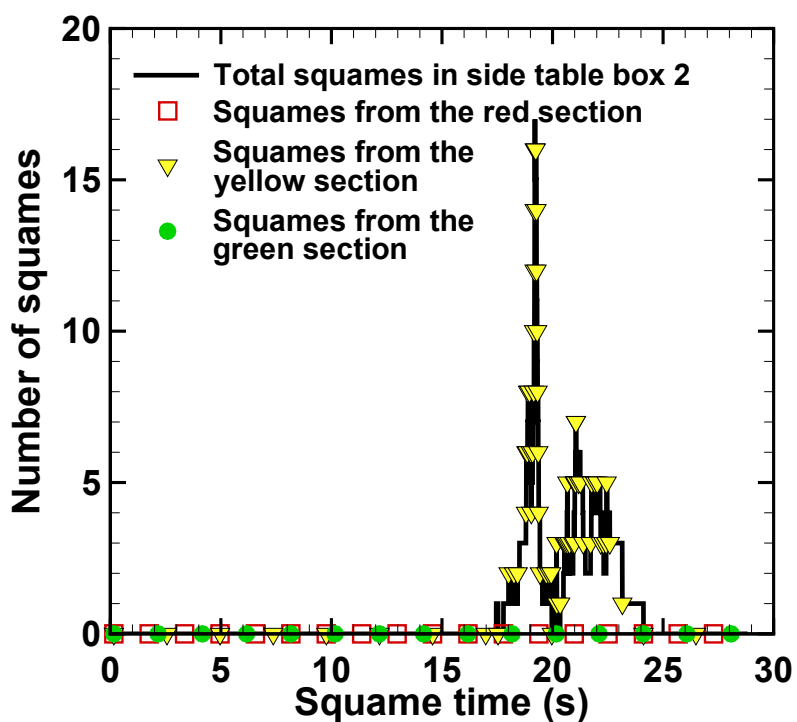
Figure 29: Four color-coded regions of interest, for recording the temporal history of the number of squames reaching them, shown in different views (a–d). The regions of interest include the zones above the two side tables, above the OT, and above the patient's knee.

computation continued for another 30s. With the blower on, hot air is discharged through the sides covering the patient's arms into the ambient air and strong thermal plumes rise under the operating table. Some of the edges of the drape are very close to the floor (see figure 4b) and the hot air plume drags squames with it making them rise upwards faster than in the case when the blower was off. A majority of the squame particles are transported away from the table towards the outlet grilles. However, a statistically significant number of particles are lifted above the operating table with some even reaching the height of the surgeons. The particles rise due to buoyancy and then get flushed down onto the operating table by the incoming ventilation air from the inlet grilles. The particles then do enter the imaginary boxes of interest, specifically above the operating table and the patient's knee.

Figures 30 and 31 show the number of squame particles as a function of time entering the four imaginary boxes of interest (above the side tables, above the operating table, and patient's knee). It can be seen from Figure 31b that no particles are found inside these boxes for the first 17s, which is about the time needed for the ventilation air to travel from the ceiling to the floor. After this time, the number of squame particles in the box above the OT increases almost in a linear fashion. Within 30s of physical time, the number of squame particles within the OT box are about 2500 and increasing. Figure 31a shows that at about 23s, some of the particles above the OT start to enter the box above the knee, which is a very narrow zone surrounding the patient's knee. The number of these particles increases linearly to about 600. Note that some of these particles do get trapped at the knee, some are carried away by the air flow and hence the number appears to be decreasing after about 25s. From the instantaneous snapshot of the squames shown in figures 24b and 27b, it can be seen that several particles are still above the OT and moving downward due to the air from the inlet grilles. It is thus expected that more particles will enter the box above the patient's knee, potentially raising the probability of infection. It is also interesting to note that the squame particles entering the box above the OT and above the knee are mainly the red-colored particles initiated from the side of the table with two surgeons. Owing to the asymmetry in the CAD model geometry, the flow pattern around each side of the table is different and the recirculation region created by the incoming air from the inlet grilles is also asymmetric. The rise and eventual trapping of the squames within the knee box is thus also related to which side of the table it originated from. The boxes above the side tables also entrain about 15 squame particles as can be seen from figures 30a,b. This suggests that

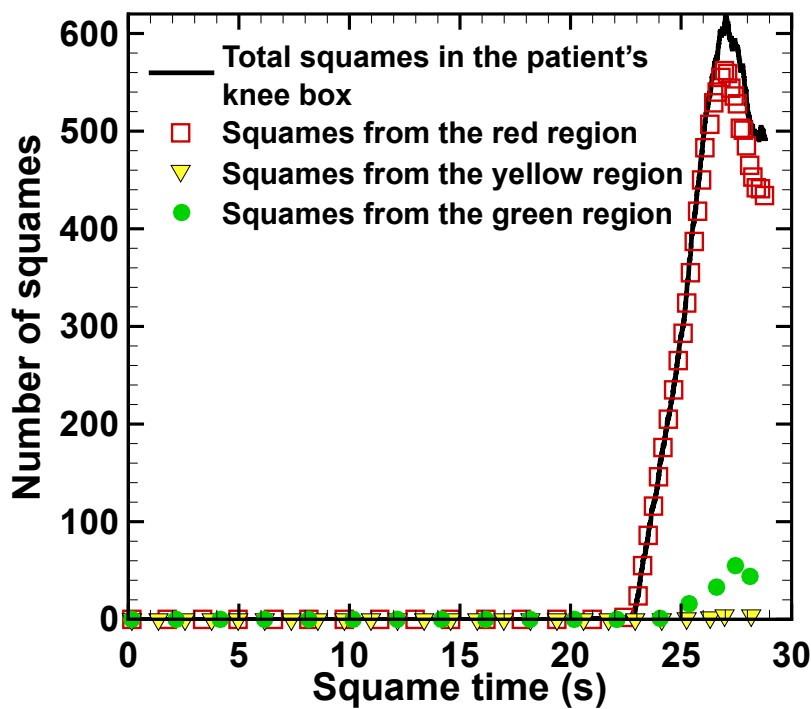


(a)

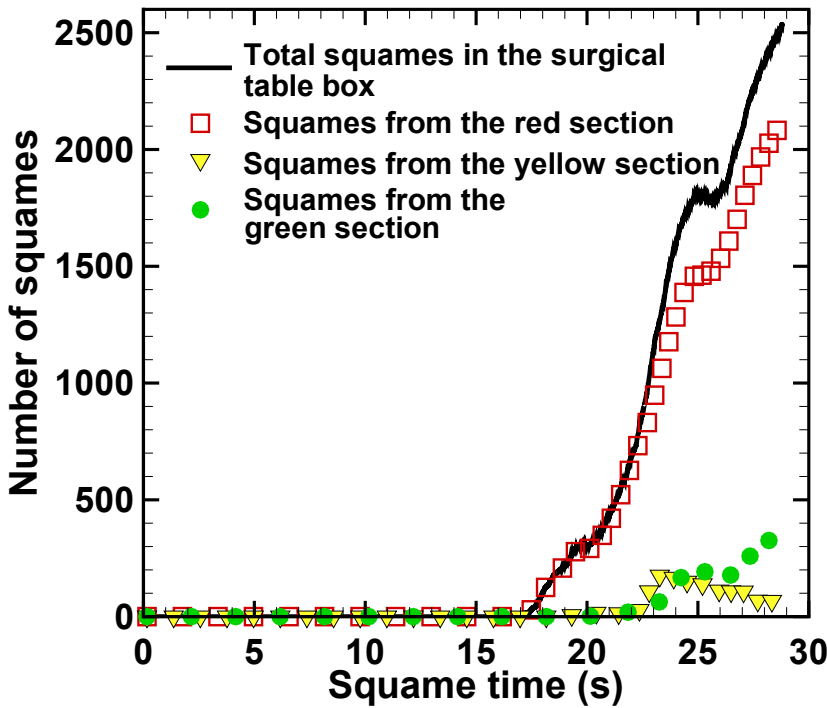


(b)

Figure 30: Temporal history of the total number of squames (shown by black color) entering four different regions of interest: (a) side table box 1, and (b) side table box 2. Also shown in color is the number of color-coded squame particles entering from the red, green and yellow regions of the figure 21.



(a)



(b)

Figure 31: Temporal history of the total number of squames (shown by black color) entering four different regions of interest: (a) the patient's knee area, and (b) the OT box. Also shown in color is the number of color-coded squame particles entering from the red, green and yellow regions of the figure 21.

the surgical instruments on the side tables also have a small probability of carrying squames to the surgical site.

5 Summary and Concluding Remarks

A high-fidelity, large-eddy simulation (LES) was performed to study the interaction of the operating room (OR) ultra-clean ventilation air flow and the flow created by a forced air warming system (3MTM Bair HuggerTM blower) and its impact on the dispersion of squames particles. A full three-dimensional design of an OR with operating table (OT), surgical lamps, medical staff, side tables, a blower, and a patient undergoing knee surgery was constructed. Unstructured grid elements involving hexahedra, tetrahedra, pyramids and wedges were used to capture the complex geometry of the OR. An arbitrary shaped, unstructured grid flow solver for LES based on governing equations for variable density in the limit of zero-Mach number was used. Ultraclean ventilation air enters the OR through 10 ceiling grilles with air changes per hour (ACH) of 24.45 and flow Reynolds number, based on the air inlet grille size and mean air inlet velocity, of 9226. The air inlet flow was developed from a periodic duct flow with the required target mass flow rate for each grille. No-slip conditions were applied for all solid surfaces and convective outflow condition was used at the four outlet grilles. Temperature values were specified at the surfaces of inlet grilles, the surgical lamps, heads of the medical staff, patient's head, and patient's knee and all other boundary surfaces were assumed adiabatic. Computations were performed on 1600 processors in parallel and flow statistics involving the time-averaged mean velocity field, turbulence intensity, and temperature distribution were computed.

Two computations were performed with the blower-off and blower-on to calculate a three-dimensional, time-dependent flow within the OR. Rising thermal plumes from the warm surfaces of surgeons heads, the patient's knee, patient's head, and the surgical lamp were calculated. With the blower on, air was drawn from the floor of the OR, heated, and blown into a blanket that covers the torso region of the patient. The blanket was covered with a plastic drape. The blower hot air generated forced convective currents and strong thermal plumes that interacted with the ultra-clean ventilation air. For both cases, trajectories of 3 million squames, placed initially on the floor in a small region surrounding the OT and surgeons, were calculated and contrasted to quantify the effect

of the hot air blower. The squames particles were assumed to be spherical in shape with 10 micron diameter and density of liquid water. The particle trajectories were tracked in a Lagrangian frame by computing the drag, lift, and buoyancy forces. The temporal variations of the number of squames particles within four imaginary boxes placed strategically above the two side tables, over the OT, and one surrounding the patient's knee were calculated and contrasted between the blower-off and blower-on cases. The following main conclusions can be drawn from these predictive computations:

1. For the case of blower-off, the ventilation air from the ceiling inlet grilles moves downwards, then is deflected by the surgical lights and the table, impinges on the floor farther away from the OT, and finally exits through the outlet grilles. Large recirculation regions are created on both sides of the table. The flow is not symmetric owing to asymmetries in the configuration of the OR contents. The maximum turbulence intensity level is about 30% in the high shear regions between the inlet air streams and the initial stagnant air in the OR, as well as near the warm surgical lights due to the buoyant plume. It is observed that the buoyant plumes from the patient's knee and other warm surfaces are relatively weak, and do not significantly alter the mean ventilation air flow.
2. For the case of blower-on, the mean flow underneath and around the OT is significantly modified and large levels of turbulence intensity are observed under the OT. The turbulence intensity levels are as high as 60% in regions affected by the rising thermal plumes from the blower. The instantaneous temperature contours confirm that the increased turbulence level is mainly because of the thermal plumes from the hot blower air causing higher temperature regions under the OT in comparison with the blower-off case. The flow is also highly asymmetric owing to the orientation and location of the drape. The rising thermal plumes are even observed to reach the ceiling in some regions and the downward ventilation flow from the inlet grilles was modified above the OT which also affected the recirculation region.
3. Drastic differences in the trajectories of the squames are observed between the blower-off and blower-on cases. With the blower-off, the majority of the squames are dispersed by the ventilation air flow towards the outlet grilles. None of the squames actually rise to the level of the side tables or the OT. In contrast, with the blower-on, a large number of squames are lifted upwards by the rising thermal plumes. Some of the squames are lifted above the surgeons

heads and are blown towards the OT by the downward moving ventilation air. Large number of squames are seen to be above the OT, several are surrounding the surgeons hands, above the side tables, and some are very close to the patient's knee and the surgical site. Majority of the squames that come close to the surgical site were found to have originated from the sides parallel to the length of the OT.

4. With the blower off, none of the squames particles were found to enter the four imaginary boxes placed above the side tables, OT, and a region surrounding the patient's knee. Some particles are lifted from the floor over time, but none rise close to the level of the imaginary boxes as the downward flow due to the ventilation air keeps the particles closer to the floor. With the blower turned on, hot air discharged from the edges of the drape and the resultant thermal plumes drag the squames, making them rise upwards. Some of the squames rise above the surgeons heads in the recirculation region on the sides of the OT. These particles are then flushed down onto the OT by the ventilation air from the inlet grilles. Statistically significant particles do enter the imaginary boxes of interest above the operating table and the patient's knee. Few particles are also observed above the side tables.

Starting with the worst-case scenario of having squames on the floor, it was shown that the hot air from the blower and the resultant thermal plumes are capable of lifting the particles and transporting them to the side tables, above the operating table, and the surgical site. It should be emphasized that if we also include the repetitive motion of the surgeons, the motion of medical assistants to fetch the surgical instruments placed on the side tables, and the resulting suspended squames shed by all staff in the OR, then the probability of dispersing the squames to the surgical site will be increased even further.

Although computationally intensive, large-eddy simulation of convective ventilation air flow and hot air from the blower in an OR is necessary to provide reliable predictions of the turbulent flow and dispersion of squames.

Appendix A

The aerodynamic behavior of squames suspended in a fluid is in general dependent upon the size and shape of the squames, their density, relative velocity with respect to the fluid motion, and density of the fluid. In the present study, the squames are suspended in air at room temperature (density ρ_g). The human skin cells or squames typically are disc-shaped with a diameter ranging from 4–20 μm and a thickness of 3–5 μm with density close to that of liquid water ($\rho_p = 1000 \text{ kg/m}^3$) (Noble *et al.*, 1963; Noble, 1975; Snyder, 2009).

Settling of a squame particle depends on its weight, the drag and buoyancy force on the particle, and its orientation relative to the flow direction. Owing to the changes in orientation and also resultant rotation and torque on disc particles, computing large number of trajectories in a Lagrangian frame is complicated. It is thus easier to assume these particles of spherical shape with an equivalent diameter such that their aerodynamic characteristics are matched. An equivalent diameter of the spherical particle should be calculated by matching the settling velocities for the two shapes.

Since $\rho_p/\rho_g = 1000$, the buoyancy force is much smaller compared to the weight of the particle. Then the settling velocity can be obtained from the balance of drag and gravitational forces,

$$F_d = F_g. \quad (24)$$

The drag and gravitational forces on a disc-shaped particle are given as,

$$F_d = C_{d,\text{disc}} \frac{1}{2} \rho_g U_{\text{disc}}^2 A_p, \quad (25)$$

$$F_g = (A_p h_{\text{disc}}) \rho_p g; \quad A_p = \frac{\pi}{4} D_{p,\text{disc}}^2 \quad (26)$$

where U_{disc} is the settling velocity of the disc, $C_{d,\text{disc}}$ is the drag coefficient, A_p is the frontal area of the circular disc, g is the gravitational acceleration, $D_{p,\text{disc}}$ is the diameter, and h_{disc} is the thickness of the disc. Equating the drag force to the weight of the disc to obtain the settling velocity as,

$$U_{\text{disc}} = \sqrt{2g \left(\frac{\rho_p}{\rho_g} \right) \left(\frac{h_{\text{disc}}}{C_{d,\text{disc}}} \right)}. \quad (27)$$

Following similar procedure, the settling velocity of a sphere of diameter $D_{p,\text{sphere}}$ can be ob-

tained as,

$$U_{\text{sphere}} = \sqrt{\frac{4}{3}g \left(\frac{\rho_p}{\rho_g} \right) \left(\frac{D_{p,\text{sphere}}}{C_{d,\text{sphere}}} \right)}, \quad (28)$$

853 where $C_{d,\text{sphere}}$ is the drag coefficient on a spherical particle.

854 In order to match the aerodynamic performance of the two shapes, the two settling velocities
855 should be the same. Equating U_{disc} and U_{sphere} we get,

$$D_{p,\text{sphere}} = \frac{3}{2}h_{\text{disc}} \left(\frac{C_{d,\text{sphere}}}{C_{d,\text{disc}}} \right). \quad (29)$$

For Stokes flow ($Re \leq 1$), the drag coefficients are given as (Munson *et al.*, 1990),

$$C_{d,\text{sphere}} = \frac{24}{Re} \quad (30)$$

$$C_{d,\text{disc}} = \frac{20.4}{Re}, \quad \text{flow normal to circular disc} \quad (31)$$

$$= \frac{13.6}{Re}, \quad \text{flow parallel to circular disc.} \quad (32)$$

856 Using a disc thickness of $h_{\text{disc}} = 5\mu\text{m}$, and using the drag coefficients for the disc and the sphere,
857 equation (29) gives an equivalent spherical diameter in the range of $D_{p,\text{sphere}} = 8.78$ and $13.2\mu\text{m}$.
858 Thus, an assumption of 10 micron spherical particle is reasonable to obtain similar dispersion be-
859 havior on an average as that of the disc-shaped squames particles.

References

- ALBRECHT, MARK, GAUTHIER, ROBERT L, BELANI, KUMAR, LITCHY, MARK & LEAPER, DAVID 2011 Forced-air warming blowers: An evaluation of filtration adequacy and airborne contamination emissions in the operating room. *American journal of infection control* **39** (4), 321–328.
- APTE, SV, GOROKHOVSKI, M. & MOIN, P. 2003a LES of atomizing spray with stochastic modeling of secondary breakup. *International Journal of Multiphase Flow* **29** (9), 1503–1522.
- APTE, SV, MAHESH, K. & LUNDGREN, T. 2008a Accounting for finite-size effects in simulations of disperse particle-laden flows. *International Journal of Multiphase Flow* **34** (3), 260–271.
- APTE, SV, MAHESH, K. & MOIN, P. 2008b Large-eddy simulation of evaporating spray in a coaxial combustor. *Proceedings of the Combustion Institute* **32**, accepted for publication.
- APTE, SV, MAHESH, K., MOIN, P. & OEFELEIN, JC 2003b Large-eddy simulation of swirling particle-laden flows in a coaxial-jet combustor. *International Journal of Multiphase Flow* **29** (8), 1311–1331.
- APTE, SOURABH V, MAHESH, KRISHNAN, GOROKHOVSKI, MICHAEL & MOIN, PARVIZ 2009 Stochastic modeling of atomizing spray in a complex swirl injector using large eddy simulation. *Proceedings of the Combustion Institute* **32** (2), 2257–2266.
- AUSTIN, PAUL N 2015 Guest editorial. *AANA journal* **83** (4), 237.
- CHEN, X-Q & PEREIRA, JCF 1998 Computation of particle dispersion in turbulent liquid flows using an efficient lagrangian trajectory model. *International journal for numerical methods in fluids* **26** (3), 345–364.
- CHOW, TIN-TAI & WANG, JINLIANG 2012 Dynamic simulation on impact of surgeon bending movement on bacteria-carrying particles distribution in operating theatre. *Building and Environment* **57**, 68–80.
- CLARK, RAYMOND P. & DE CALCINA-GOFF, MERVYN L. 2009 Some aspects of the airborne transmission of infection. *Journal of The Royal Society Interface* **6** (Suppl 6), S767–S782.

- 886 CROWE, CT, TROUTT, TR & CHUNG, JN 1996 Numerical models for two-phase turbulent flows.
887 *Annual Review of Fluid Mechanics* **28** (1), 11–43.
- 888 DRUZHININ, OA & ELGHOBASHI, S. 1998 Direct numerical simulations of bubble-laden turbulent
889 flows using the two-fluid formulation. *Physics of Fluids* **10**, 685.
- 890 EATON, JK & FESSLER, JR 1994 Preferential concentration of particles by turbulence. *Interna-*
891 *tional Journal of Multiphase Flow* **20**, 169–209.
- 892 EATON, J.K. & SEGURA, J.C. 2006 On momentum coupling methods for calculation of turbulence
893 attenuation in dilute particle-laden gas flows. *Fluid Mechanics and its Applications* **81**, 39.
- 894 ELGHOBASHI, S. 1994 On predicting particle-laden turbulent flows. *Flow, Turbulence and Com-*
895 *bustion* **52** (4), 309–329.
- 896 ELGHOBASHI, S. 2006 An updated classification map of particle-laden turbulent flows. *Fluid Me-*
897 *chanics and Its Applications* **81**, 3–10.
- 898 FERRANTE, A. & ELGHOBASHI, S. 2004 On the physical mechanisms of drag reduction in a spa-
899 tially developing turbulent boundary layer laden with microbubbles. *Journal of Fluid Mechanics*
900 **503**, 345–355.
- 901 FERRANTE, A. & ELGHOBASHI, S. 2007 On the accuracy of the two-fluid formulation in direct
902 numerical simulation of bubble-laden turbulent boundary layers. *Physics of Fluids* **19**, 045105.
- 903 GERMANO, MASSIMO, PIOMELLI, UGO, MOIN, PARVIZ & CABOT, WILLIAM H 1991 A dynamic
904 subgrid-scale eddy viscosity model. *Physics of Fluids A: Fluid Dynamics (1989-1993)* **3** (7),
905 1760–1765.
- 906 HAM, F., APTE, S., IACCARINO, G., WU, X., HERRMANN, M., CONSTANTINESCU, G., MA-
907 HESH, K. & MOIN, P. 2003 Unstructured LES of reacting multiphase flows in realistic gas turbine
908 combustors. Annual Research Briefs 2003. *Center for Turbulence Research, NASA Ames/Stanford*
909 *Univ* pp. 139–160.
- 910 HAM, FRANK & IACCARINO, GIANLUCA 2004 Energy conservation in collocated discretization
911 schemes on unstructured meshes. *Annual Research Briefs* **2004**, 3–14.

- 912 KELLAM, MELISSA D, DIECKMANN, LORAIN S & AUSTIN, PAUL N 2013 Forced-air warming
913 devices and the risk of surgical site infections. *AORN journal* **98** (4), 353–369.
- 914 KRAVCHENKO, AG & MOIN, PARVIZ 1997 On the effect of numerical errors in large eddy simu-
915 lations of turbulent flows. *Journal of Computational Physics* **131** (2), 310–322.
- 916 KULICK, JD, FESSLER, JR & EATON, JK 2006 Particle response and turbulence modification in
917 fully developed channel flow. *Journal of Fluid Mechanics Digital Archive* **277**, 109–134.
- 918 LEAPER, DAVID, ALBRECHT, MARK & GAUTHIER, ROBERT 2009 Forced-air warming: a source
919 of airborne contamination in the operating room? *Orthopedic reviews* **1** (2), 28.
- 920 LEES, JULIENNE & BRIGHTON, WD 1972 Simulated human skin scales. *Journal of Hygiene*
921 **70** (03), 557–565.
- 922 LEGG, AJ, CANNON, T & HAMER, AJ 2012 Do forced air patient-warming devices disrupt unidi-
923 rectional downward airflow? *J Bone Joint Surg Br* **94** (2), 254–256.
- 924 MAHESH, K., CONSTANTINESCU, G., APTE, S., IACCARINO, G., HAM, F. & MOIN, P. 2006
925 Large-eddy simulation of reacting turbulent flows in complex geometries. *Journal of Applied*
926 *Mechanics* **73**, 374.
- 927 MAHESH, K., CONSTANTINESCU, G. & MOIN, P. 2004 A numerical method for large-eddy sim-
928 ulation in complex geometries. *Journal of Computational Physics* **197** (1), 215–240.
- 929 MAXEY, MARTIN R & RILEY, JAMES J 1983 Equation of motion for a small rigid sphere in a
930 nonuniform flow. *Physics of Fluids (1958-1988)* **26** (4), 883–889.
- 931 MCGOVERN, PD, ALBRECHT, M, BELANI, KG, NACHTSHEIM, C, PARTINGTON, PF, CAR-
932 LUKE, I & REED, MR 2011 Forced-air warming and ultra-clean ventilation do not mix. *J Bone*
933 *Joint Surg Br* **93** (11), 1537–1544.
- 934 MCNEILL, JAMES, HERTZBERG, JEAN & ZHAI, ZHIQIANG JOHN 2013 Experimental investiga-
935 tion of operating room air distribution in a full-scale laboratory chamber using particle image
936 velocimetry and flow visualization .

- 937 MCNEILL, JAMES S *et al.* 2012 Field measurements of thermal conditions during surgical proce-
 938 dures for the development of cfd boundary conditions. *ASHRAE Transactions* **118**, 596.
- 939 MEMARZADEH, FARHAD 2003 Reducing risks of surgery. *ASHRAE journal* **45** (2), 28.
- 940 MEMARZADEH, FARHAD & MANNING, ANDREW P 2002 Comparison of operating room ventila-
 941 tion systems in the protection of the surgical site/discussion. *ASHRAE transactions* **108**, 3.
- 942 MITTAL, RAJAT & MOIN, PARVIZ 1997 Suitability of upwind-biased finite difference schemes for
 943 large-eddy simulation of turbulent flows. *AIAA journal* **35** (8), 1415–1417.
- 944 MOIN, P. & APTE, SV 2006 Large-eddy simulation of realistic gas turbine combustors. *AIAA Jour-
 945 nal* **44** (4), 698–708.
- 946 MOIN, P. & MAHESH, K. 1998 Direct numerical simulation: A tool in turbulence research. *Annual
 947 Reviews in Fluid Mechanics* **30** (1), 539–578.
- 948 MOIN, P., SQUIRES, K., CABOT, W. & LEE, S. 1991 A dynamic subgrid model for compressible
 949 turbulence and scalar transport. *Physics of Fluids A*, **3**, 2746–2757.
- 950 MORETTI, B, LAROCCA, AMV, NAPOLI, C, MARTINELLI, D, PAOLILLO, L, CASSANO, M,
 951 NOTARNICOLA, A, MORETTI, L & PESCE, V 2009 Active warming systems to maintain pe-
 952 rioperative normothermia in hip replacement surgery: a therapeutic aid or a vector of infection?
 953 *Journal of Hospital Infection* **73** (1), 58–63.
- 954 MUNSON, BRUCE ROY, YOUNG, DONALD F & OKIISHI, THEODORE H 1990 Fundamentals of
 955 fluid mechanics. *New York* **3** (4).
- 956 NG, V, LAI, A & HO, V 2006 Comparison of forced-air warming and electric heating pad for
 957 maintenance of body temperature during total knee replacement. *Anaesthesia* **61** (11), 1100–1104.
- 958 NOBLE, WC 1975 Dispersal of skin microorganisms. *British Journal of Dermatology* **93** (4), 477–
 959 485.
- 960 NOBLE, WC, LIDWELL, OM, KINGSTON, D *et al.* 1963 The size distribution of airborne particles
 961 carrying micro-organisms. *J Hyg (Lond)* **61** (385), e391.

- 962 PEREIRA, MARCELO LUIZ & TRIBESS, ARLINDO 2005 A review of air distribution patterns in
963 surgery rooms under infection control focus. *Revista de Engenharia Térmica* **4** (2).
- 964 PIERCE, C.D. & MOIN, P. 1998a Turbulent flow over three-dimensional dunes: 2. Fluid and bed
965 stresses. *Physics of Fluids* **10**, 3041–3044.
- 966 PIERCE, CHARLES DAVID 2001 Progress-variable approach for large-eddy simulation of turbulent
967 combustion. PhD thesis, Citeseer.
- 968 PIERCE, CHARLES D & MOIN, PARVIZ 1998b Large eddy simulation of a confined coaxial jet with
969 swirl and heat release. *AIAA paper* **2892**.
- 970 PIOMELLI, U 2014 Large eddy simulations in 2030 and beyond. *Philosophical Transactions of*
971 *the Royal Society of London A: Mathematical, Physical and Engineering Sciences* **372** (2022),
972 20130320.
- 973 POPE, SB 2000 *Turbulent Flows*. Cambridge University Press.
- 974 POZORSKI, JACEK & APTE, SOURABH V 2009 Filtered particle tracking in isotropic turbulence
975 and stochastic modeling of subgrid-scale dispersion. *International Journal of Multiphase Flow*
976 **35** (2), 118–128.
- 977 READE, W.C. & COLLINS, L.R. 2000 Effect of preferential concentration on turbulent collision
978 rates. *Physics of Fluids* **12**, 2530.
- 979 ROUSON, D.W.I. & EATON, J.K. 2001 On the preferential concentration of solid particles in tur-
980 bulent channel flow. *Journal of Fluid Mechanics* **428**, 149–169.
- 981 SAARINEN, PEKKA E, KALLIOMÄKI, PETRI, TANG, JULIAN W & KOSKELA, HANNU 2015
982 Large eddy simulation of air escape through a hospital isolation room single hinged doorwayval-
983 idation by using tracer gases and simulated smoke videos. *PloS one* **10** (7), e0130667.
- 984 SAFFMAN, PGT 1965 The lift on a small sphere in a slow shear flow. *Journal of fluid mechanics*
985 **22** (02), 385–400.

- 986 SESSLER, DANIEL I, OLMSTED, RUSSELL N & KUELPMANN, RUEDIGER 2011 Forced-air warm-
 987 ing does not worsen air quality in laminar flow operating rooms. *Anesthesia & Analgesia* **113** (6),
 988 1416–1421.
- 989 SNYDER, OP 2009 A ‘Safe Hands’ hand wash program for retail food operations: a technical
 990 review. *Yeast* **55** (18.5), 14–8.
- 991 SOMMERFELD, M, ANDO, A & WENNERBERG, D 1992 Swirling, particle-laden flows through a
 992 pipe expansion. *Journal of fluids engineering* **114** (4), 648–656.
- 993 SRIDHAR, G. & KATZ, J. 1999 Effect of entrained bubbles on the structure of vortex rings. *J. Fluid*
 994 *Mech.* **397** (-1), 171–202.
- 995 STRAUB, A. 2016 *Bentley Microstation Design V8i, M/E Engineering, P.C.*. 150 North Chestnut
 996 Street, Rochester, NY 14604, www.meengineering.com.
- 997 TENNEKES, HENDRIK & LUMLEY, JOHN LEASK 1972 *A first course in turbulence*. MIT press.
- 998 WARTTIG, SHERYL, ALDERSON, PHIL, CAMPBELL, GILLIAN & SMITH, ANDREW F 2014 Inter-
 999 ventions for treating inadvertent postoperative hypothermia. *The Cochrane Library* .
- 1000 WOOD, AM, MOSS, C, KEENAN, A, REED, MR & LEAPER, DAVID J 2014 Infection control
 1001 hazards associated with the use of forced-air warming in operating theatres. *Journal of Hospital*
 1002 *Infection* **88** (3), 132–140.